ANALYSIS OF FLOATING SUPPORT STRUCTURES FOR MARINE AND WIND ENERGY

A thesis submitted to the University of Manchester towards the degree of Doctor of Philosophy (PhD)
In the Faculty of Engineering and Physical Sciences

2014

Emmanuel Fernandez Rodriguez

School of Mechanical, Aerospace and Civil Engineering

List of Contents

Words count 45,764

List of Symbol

$\mathrm{a}_{\mathrm{axial}}$	Axial induction factor
a	Added mass of a disc
a_{T}	Tangential induction factor
a_{c}	High axial induction threshold
A	Swept area
A_{D}	Area of the disc
A_{w}	Area of the downstream
A_{wave}	Wave amplitude
A_0	Area of the upstream tube
$a_{\mathrm{i,j}}$	Added mass of the support structure in the six coupled modes
$a_{\mathrm{k,i,j}}$	Ratio of added mass between the platform and supported rotors in the six coupled modes
b	Damping of disc
$b_{\mathrm{i,j}}$	Damping of support structure in the six coupled modes
$b_{\mathrm{k,i,j}}$	Damping between support structure and rotor
$b_{\mathrm{max,i,j}}$	Maximum disc damping in the six coupled modes
b_{ord}	Ordinate
B	Number of blades
c	Chord
$c_{\mathrm{i,j}}$	Restoring coefficient of the support in the six coupled modes
C_{a}	Added mass coefficient
$C'_{\mathrm{a,i,j}}$	Added mass coefficient of the rotor expressed with volume of a disc for the six coupled modes
C_{b}	Damping coefficient of rotor in surge
C_{d}	Foil drag coefficient
C_{D}	Oscillatory drag coefficient
$C_{\mathrm{D,c}}$	Drag coefficient in uniform flow
$C_{\mathrm{D,1}}$	Drag coefficient in combined current and oscillatory flow due to contribution of the current velocity only

$C_{\mathrm{D,2}}$	Drag coefficient in combined current and oscillatory flow due to contribution of the oscillatory velocity
$C_{\mathrm{D,wave}}$	Drag coefficient in combined current and waves due to contribution of wave velocity
C_{i}	Temporal correlation factor
C_{l}	Foil lift coefficient
C_{M}	Inertia coefficient
C_{P}	Power coefficient
$C_{\mathrm{P,max}}$	Betz limit
C_{T}	Thrust coefficient
C_{x}	Horizontal force of blade section
C_{y}	In-plane force of blade section
D	Diameter
D_{l}	Length Characteristic
E	Energy spectrum of the incident flow
$\mathrm{f}_{\mathrm{initial}}$	Initial conditions
f_{H}	Local hub loss multiplying factor
f_{k}	Local tip loss multiplying factor
f	Frequency
f_{n}	Natural frequency
f_{r}	Frequency of mean rotational speed
f_{wave}	Peak frequency of wave
F	Force
$\bar{F}$	Mean force of the combined oscillatory and turbulent flow
F'	Force fluctuations around the mean
F_{drag}	Drag force on the blade segment
F_{dynamic}	Dynamic force
$F_{\mathrm{D,1}}$	Drag force in oscillatory flow due to current flow separation
$F_{\mathrm{D,2}}$	Drag force in oscillatory flow due to streamwise velocity separation
F_{H}	Hub loss factor
F_{j}	Individual force from time-varying measurements
F_{k}	Tip loss factor

F_{l}	Lift force
F_{loss}	Tip and hub losses factor
F_{m}	Measured force
$F_{\mathrm{mech,t}}$	Force to overcome the mechanical friction and tower
$F_{\mathrm{neglected,1}}$	Neglected term in the Morison equation due to flow separation of the current
$F_{\mathrm{neglected,2}}$	Neglected term in the Morison equation due to flow separation of the streamwise velocity
F_{N}	Normal Rotor force
F_{osc}	Rotor force due to imposed steady oscillations or waves
$F_{\mathrm{osc,max}}$	Maximum force due to oscillatory flow only
F_{T}	Total force on the fluid
F_{Th}	Threshold force
F_{tower}	Tower load
F_{turb}	Excitation force of the rotor in turbulent current
F_{x}	Horizontal load
F_0	Time-averaged force in mean flow with turbulence present
$F_{\frac{1}{\mathrm{n}}}$	Force with a probability of occurrence of $\frac{1}{\mathrm{n}}$
$F'_{\frac{1}{\mathrm{n}}}$	Force with a probability of occurrence of $\frac{1}{\mathrm{n}}$ due to the turbulent fluctuations
g	Gravity constant (9.81 m/s^2)
h	Water depth of the wave-current flume
H	Wave height
H_0	Mean wave height
H_{s}	Significant wave height
k	Wave number
$k_{\mathrm{i,j}}$	Stiffness of mooring lines
k_{s}	Shape factor
$\mathrm{k}-\epsilon, \mathrm{k}-\omega$	Turbulence models
$\mathrm{K_{spera}}$	Spera thrust factor
KC	Keulegan Carpenter number
$\mathrm{K_i}$	Force factor in the six modes

K_{I}	Admittance factor
$\mathrm{l_x}$	Semi-axis length in x direction
$\mathrm{l_y}$	Semi-axis length in y direction
$\mathrm{l_z}$	Semi-axis length in z direction
L	Length of the tower
L_{ii}	Average length scale where $i = x, y, z$
L_{w}	Wave length
m	Mass
$m_{\mathrm{rotor,i,j}}$	Mass of the rotor in the six coupled modes
m_{slope}	Slope
M	Time length of the long run measurement
M_{a}	Mass of a spheroid
$M_{\mathrm{k,i,j}}$	Mass ratio in the six coupled modes
$m_{\mathrm{i,j}}$	Mass of the support structure in the six coupled modes
$M2$	Harmonics due to moon
n_{exc}	Arbitrary number of measured forces
n	Number of rotors
N	Number of forces samples
p	Pressure
p_0	Pressure at the upstream tube
p_4	Pressure at the wake
p_+	Pressure before the disc
p_-	Pressure after the disc
P	Probability
P_{p}	Power
Q	Torque
r	Radii
rms	Root mean square
r_{R}	Local radii over rotor radius
R	Radius
$\mathrm{R^2}_{\mathrm{res}}$	Least square residuals
R_{hub}	Hub radius

Re	Reynolds number
$S2$	Harmonics due to sun
t	Time
t_{th}	Thickness
T	Thrust
T_{amb}	Period of the ambient flow based on energy spectrum of speed fluctuations
TI	Turbulence Intensity
T_{p}	Mean period of probability range
T_{R}	Return period
T_{wave}	The wave period
TSR	Tip-Speed Ratio
TSR_{r}	Local Tip-Speed Ratio
u	Velocity of the ambient flow
u'	Time fluctuations of the upstream velocity around the mean
u_{b}	Bypass velocity
u_{c}	Velocity in a mean flow with turbulence present
u_{D}	Disc velocity
u_{Dc}	Disc velocity in bounded flow
u_{wave}	Wave velocity
$u_{\mathrm{wave,m}}$	Measured wave velocity
$u_{\mathrm{wave,p}}$	Wave velocity using linear wave theory
u_{x}	Velocity in x-axis
u_{w}	Wake velocity
u_{wc}	Wake velocity in bounded flow
u_{y}	Velocity in y-axis
u_{z}	Velocity in z-axis
u_{0}	Mean upstream velocity
$u_{0\mathrm{c}}$	Equivalent water velocity to bounded flow
U	Velocity at an arbitrary location of the stream tube
U_{a}	Velocity of the incident flow using the Morison Equation
U_{0}	Depth-averaged velocity

V	Volume
x	Displacement in surge
$x_{\mathrm{i,j}}$	Motion of the support in the six coupled modes
$\|\dot{x}\|_{\mathrm{max}}$	Highest measured amplitude of the forced rotor's streamwise tests
$x_{\mathrm{rotor,i,j}}$	Motion of the rotor in the six coupled modes
X	Matrix of set of differential equations
$X_{\mathrm{e,i}}$	External forcing in the six degrees of freedom
X_{i}	Wave force in the six modes
$X_{\mathrm{h,i,j}}$	Hydrodynamics of support structure in the six coupled modes
$\chi^2\|f\|$	Admittance factor
y	Vertical displacement
W	Width
W_{rel}	Relative wind velocity
z	Distance along the flume depth
$\mathcal{F}_{\mathrm{normal}}$	Normal distribution
$\mathcal{F}_{\mathrm{Pareto}}$	Pareto distribution
$\mathcal{F}_{\mathrm{Type\ 1}}$	Type 1 distribution
$\mathcal{F}_{\mathrm{weibull}}$	Weibull distribution
α	Angle of attack
β	Stokes or Frequency number
δ	Phase
η	Surface elevation
ε	Blockage factor
ξ	Attenuation damping rate
γ	Blade-pitch angle
λ_{s}	Shape parameter
μ_0	Mean of distribution
μ	Dynamic viscosity of medium
ν	Kinematic viscosity
ω	Angular speed
φ	Relative wind angle
ρ	Density of fluid

σ	Standard deviation
$\sigma_{\mathrm{r,a}}$	Alternative blade chord solidity
σ_{r}	Blade chord solidity
τ	Porosity ratio
τ_{t}	Correlation time
θ_{r}	Pitch response at the hub height

List of Figures

List of Tables

Abstract

The University of Manchester
Emmanuel Fernandez Rodriguez
Doctor of Philosophy
Analysis of Floating Support Structures for Marine and Wind Energy
December 2014

Bed connected support structures such as monopiles are expected to be impractical for water depths greater than 30 m and so there is increasing interest in alternative structure concepts to enable cost-effective deployment of wind and tidal stream turbines. Floating, moored platforms supporting multiple rotors are being considered for this purpose. This thesis investigates the dynamic response of such floating structures, taking into account the coupling between loading due to both turbulent flow and waves and the dynamic response of the system.

The performance and loading of a single rotor in steady and quasi-steady flows are quantified with a Blade Element Momentum Theory (BEMT) code. This model is validated for steady flow against published data for two 0.8 m diameter rotors (Bahaj, Batten, et al., 2007; Galloway et al., 2011) and a 0.27 m diameter rotor (Whelan and Stallard, 2011). Time-averaged coefficients of thrust and power measured by experiment in steady turbulent flow were in agreement with BEMT predictions over a range of angular speeds. The standard deviation of force on the rotor is comparable to that on a porous grid for comparable turbulence characteristics.

Drag and added mass coefficients are determined for a porous disc forced to oscillate normal to the rotor plane in quiescent flow and in the streamwise axis in turbulent flow. Added mass is negligible for the Keulegan Carpenter number range considered (KC < 1). The drag coefficient in turbulent flow was found to decay exponentially with KC number, to 2±10% for KC values greater than 0.5. These coefficients were found to be in good agreement with those for a rotor in the same turbulent flow with disc drag coefficient within 12.5% for KC < 0.65.

An extreme-value analysis is applied to the measured time-varying thrust due to turbulent flow and turbulent flow with waves to obtain forces with 1%, 0.1% and 0.01% probability of exceedance during operating conditions. The 1% exceedance force in turbulent flow with turbulence intensity of 12% is around 40% greater than the mean thrust. The peak force in turbulent flow with opposing waves was predicted to within 6% by superposition of the extreme force due to turbulence only with a drag force based on the relative wave-induced velocity at hub-height estimated by linear wave theory and with drag coefficient of 2.0.

Response of a floating structure in surge and pitch is studied due to both wave-forcing on the platform defined by the linear diffraction code WAMIT and due to loading of the operating turbine defined by a thrust coefficient and drag coefficient. Platform response can either increase or decrease the loading on the rotor and this was dependant on the hydrodynamic characteristics of the support platform. A reduction of the force on the rotor is attained when the phase difference between the wave force on the support and the surface elevation is close to $\pm\pi$ and when the damping of the support is increased. For a typical support and for a wave condition with phase difference close to π, the 1% rotor forces were reduced by 8% when compared to the force obtained with a rotor supported on a stiff tower.

Declaration

No portion of the work referred to in the thesis has been submitted in support of an application for another degree or qualification of this or any other University or other institute of learning.

Copyright

Acknowledgements

I thank my family for the encouragement, support and trust given to me all these years. God for making everything possible, express gratitude to the government of Mexico, University of Manchester, Dr. Teresa Alonso, supervisors Dr. Tim Stallard and Prof. Peter Stansby, lecturers, technicians, students, staff members, friends and everyone else for the help and guidance I needed to complete this research.

CHAPTER 1: INTRODUCTION

In this chapter, an overview is given of tidal stream energy extraction and the fundamental basis of approaches for modelling such systems. These key concepts include descriptions of site characteristics and turbine support structures.

1.1 Tidal Stream Background

Over the last decades, there has been increasing interest in the development of turbines to generate electricity from tidal streams (Hardisty, 2009; Fraenkel, 2010; Cheng-Han et al., 2012). The relatively high energy flux density and predictability of tidal flows make tidal stream systems a promising solution to reduce dependence on carbon-emitting electricity generation sources such as oil and coal. At present, a small number of commercial-scale tidal turbines are undergoing field trials to evaluate performance and reliability. The majority of such systems are horizontal-axis turbines that are designed along similar principles to wind turbines (Nelson, 2009) with the distinction that they are immersed in water. Operation in a subsea environment imposes constraints on the selection of blade material (Grogan et al., 2013) and on the range of operation that is practical to avoid cavitation (Bahaj, Molland, et al., 2007), bio-fouling (Walker et al., 2014) and corrosion. It is widely recognised that the cost of energy from such devices must be reduced to enable deployment of commercial farms. This requires accurate prediction of energy yield and the reduction of capital costs and operating costs.

1.2 Tidal Energy Resource

Various studies have predicted the annual energy yield from specific tidal stream deployment sites. The Energy Technology Support Unit (ETSU) in 1993 and the Black & Veatch (B&V) consulting company in 2005 identified and quantified the annual energy yield of a number of possible tidal stream sites around the UK and Europe (Black & Veatch Ltd., 2005). Although the speed range differed between the two reports, more than 70% of the resources considered were located in water depths greater than 40 m (Table 1.1). For these water depths only unproven systems exist to support turbines.

Furthermore, at most of the sites considered suitable for tidal stream systems, the flow is sheared and waves co-exist (Norris and Droniou, 2007). There remains uncertainty concerning the magnitude of the rotor loads obtained due to the combination of turbulent flow and waves. Peak and unsteady loading on the rotor are important factors to consider for the design of cost-effective support structures.

Table 1.1 Tidal energy resources (Black & Veatch Ltd., 2005; Blunden and Bahaj, 2007).

REF	Speed Range	UK sites	Annual Energy (GWh)	Water depths
ETSU (93)	≈ 2m/s	33	57.639	70%>48m
B&V (2005)	>1.5 m/s	42	21.812	78%>40m

In the UK, electricity generated from tidal stream resources around the coastline could provide around 16% of the 318 TWh/yr present demand (Burrows et al., 2009). The Pentland Firth has drawn particular attention from the industrial and research sectors, since this location accounts for 36% of the UK tidal stream resource (Black & Veatch Ltd., 2011). Various projects are being conducted by trade, public and governmental institutions in parts of Europe (Carballo et al., 2009; Xia et al., 2010) and America (Blanchfield et al., 2008; Karsten et al., 2008) for the assessment of tidal stream energy, as well as the development of cost-effective devices an the study of environmental impact (Neill et al., 2009; Furness et al., 2012).

1.3 Support Structures for Offshore Turbines

Wind turbines are an established technology that has been widely deployed offshore in waters of less than 30 metres depth in the last decade. Tidal prototypes are still under development and some rely on similar structural approaches to wind turbines. Exploitation of deeper sites is the objective of recent and planned wind-farm projects, but this requires the use of low-cost support structures. Several floating and moored platforms comprising single or multiple turbines are now in development as an alternative approach. Dynamic loads and rotor motions experienced by these structures directly affect reliability of the system and hence total costs but are not yet fully understood. To evaluate the dynamic response, it is necessary to quantify the dynamic loading on the supported turbine and to couple these loads with a model of support-structure response.

1.4 Design of Floating Platforms

Developers of floating support structures must address several design issues. Principally, the structure must provide a stable platform despite excitation due to turbine operation, wave-induced loading and constraint by the mooring system employed. Additionally, the turbine's pitch angle and nacelle acceleration must be kept within the operating design specified by the manufacturer (Berthelsen and Fylling, 2011). Engineering tools are required to predict within acceptable accuracy the loading on the rotor and the structure, including fatigue, turbulence and other external loads. The loading, damping and added mass of both the supported tidal stream rotor and supporting structure must be combined into a coupled model of system response. Non-linear forcing can arise from the structure geometry, rotor design and operation, mooring arrangement and wave drift.

1.5 Objectives

Wind turbines have been successfully deployed at offshore sites with water depths less than 30 metres by using gravity-based systems and rigid-bed-connected support structures. However, current technology has not provided a practical structural arrangement at the deeper sites and a significant number of long-term projects (such as floating moored devices) are currently undergoing trials. A key uncertainty exists for the time variation and peak loading of such dynamic systems. Extreme, or peak, loads represent an important design criterion for any support structure and the magnitude of such loads is a driver of the capital cost.

Unsteady horizontal loads occur on tidal stream turbines, for both fixed or floating support structures, due to sheared flows co-existing with turbulence and waves. Such loads have not been fully investigated and for floating support structures will be dependent on the influence of the incident flow on turbine loads coupled with the response of the rotor. This is also dependent on the response of the supporting structure.

The aim of this PhD is to analyse the influence of the dynamic response of a support structure on the loading of a horizontal-axis tidal stream turbine. It is addressed by investigating the dynamic loading on individual turbines resulting from the combined influence of mean flow, turbulence, opposing regular waves and oscillation of the turbine's support structure. Each load combination is investigated both experimentally and numerically using engineering tools such as Blade Element Momentum Theory (BEMT) to obtain the excitation force on the rotor. The particular focus is the influence of dynamic response on the magnitude of extreme loads applied to the turbine.

1.6 Structure of Thesis

The thesis is divided into seven chapters. In this chapter, an introduction is given of the current status and potential for energy yield of tidal stream systems. The aims and objectives of this research are presented, along with constraints and technical issues of developing floating support structures.

In the second chapter, a literature review is presented on the environmental conditions at tidal stream sites and techniques typically employed to analyse turbine loading in steady flow. The Blade Element Momentum Theory, widely used for characterisation of rotor performance, is introduced and inclusion of thrust corrections due to hub and tip losses and high axial induction factors are discussed. A review of extreme-value methods is also presented for the load characterisation of a tidal support in steady and unsteady flows.

The third chapter reports an experimental study of rotor performance in a turbulent channel flow to compare with prediction methods of Chapter 2. An extreme value analysis is applied to the time-varying thrust of a rotor supported on an effectively rigid structure to understand the effect of peak load to turbulence intensity. The extreme loads obtained characterise the loading on a support structure for return periods of approximately two days at full scale.

To inform analysis of the loading on the rotor on a flexible support, Chapter 4 reports an experimental study to determine coefficients of a Morison type drag and inertia equation for representing the time-varying force on a turbine undergoing oscillation in the streamwise direction within a steady flow. An experimental approach is taken to obtain time-varying force on the rotor for a range of oscillation amplitudes and frequencies. Added mass, damping and drag coefficients are determined for a porous disc of comparable mean thrust to a rotor and for a rotor. The peak rotor loads predicted by the fitted coefficients are compared with those obtained from the measured time-history of force providing reasonable agreement.

In Chapter 5, an experimental study is conducted on a single rotor in turbulent channel flow with co-generation of opposing waves. The procedure is to characterise and analyse the different wave conditions and to determine the extreme support forces. The rotor extreme response in the wave oscillatory flows is compared to the rotor forced oscillation tests in turbulent channel flows (Chapter 4).

In the sixth chapter, alternative support structure configurations ranging from conventional (rigid) structures through floating moored platforms to support horizontal-axis turbines are reviewed and design and development constraints identified. Response of a tidal rotor is modelled for surge only and surge with pitch to investigate variation of extreme load due to characteristics of the floating support. Rotor forcing is defined by the formulation and coefficients developed in Chapter 4. Combinations of forcing, natural period and damping of the support structure are identified that allow reduction of rotor motion and peak load.

The seventh chapter summarises the findings and conclusions of the studies of rotor performance in turbulent flow only and due to oscillatory flow with turbulence. It also addresses proposed support structure designs. Future work is outlined to improve understanding of support and rotor interaction in oblique oscillatory flows due to waves and rotor streamwise oscillation, dynamic coupling with mooring lines and hydrodynamic forcing of rotors with more degrees of freedom movement.

CHAPTER 2: HORIZONTAL-AXIS TURBINE MODELLING

In this chapter, an introduction is given to the operating-flow conditions of tidal stream turbines, along with numerical and experimental methods typically employed for analysis of power output and loading of horizontal-axis turbines. Wind-energy concepts of Blade Element Momentum Theory (BEMT), tip losses and high axial induction correction methods are briefly presented for the development of a numerical code to predict performance of a tidal rotor in steady flows. Statistical methods based on prediction of extreme wave height and forces on offshore structures are reviewed for the future assessment of peak loads influencing design life of a tidal support structure.

2.1 Tidal Streams

Tidal streams are flows of water driven by gravitational forcing. Tides are responsible for creating the tidal streams, and time variation of surface elevation is typically modelled as the sum contribution of multiple tidal constituents. Each harmonic component is provided relative to a particular location and is identified with its amplitude of motion along with its phase and the angular velocity specified in degrees per mean solar hours. The tidal constituents are mainly defined by the position of the earth relative to the sun ($S2$) and of the moon ($M2$). Other factors such as the shape of the site, the inclination, and the rotation of the earth also affect the surface elevation.

At many of the locations considered suitable for tidal stream systems, a pair of high and low tides occurs during each day. These are termed semidiurnal tides, and are primarily caused by the gravitational forcing of the moon on the oceans. The difference between low and high tides modifies the water elevation and creates a tidal current. The kinetic and potential energy of these environmental flows can be utilised to produce electricity by driving mechanical devices such as horizontal-axis turbines (Hardisty, 2009; Fraenkel, 2010; Cheng-Han et al., 2012).

Depending on the harmonics predicted for a precise place for each day, a high and a low tide may appear. These are referred to as diurnal tides, or they may instead consist of a mixture of diurnal and semidiurnal tides. The tidal currents at particular locations are usually presented in nautical charts with the magnitudes of spring and neap velocities specified at different time intervals (NOAA; Bowditch, 2002). Spring tides refer to the stage in the tidal cycle when the moon and sun are both aligned with the earth and their gravity pull on the ocean is superposed. This alignment produces a higher and lower bulge that occurs on full and new moons. By contrast, the neap tides appear when the moon and sun are positioned at right angles and their gravity force is partly cancelled out. Neap tides happen in the quarter phases of the moon with high and low tides being practically of equal height. Spring velocities have higher magnitudes than the neaps and the transitional spring-neap period lasts around seven days.

Tidal current speeds are higher magnitude in shallow waters and narrow locations such as in bays, inlets, estuaries, firths and harbours. For instance, Thomson et al. (2012) state that tidal flows have been recorded to reach velocities of up to 3.6 m/s for the Admiralty Inlet, in the Puget Sound region.

The tidal current is a velocity vector that varies with the condition of the tides and the bathymetry of the site. These mean currents induce turbulence in vertical and horizontal direction of the flow. The ratio of the standard deviation of these fluctuations to the average speed is referred to as the turbulence intensity, TI. The turbulence intensity recorded for tidal stream sites ranges from 10% to 20% (Sutherland et al., 2012; Thomson et al., 2012). Increased values of turbulence intensity have been found to decrease the overall rotor performance slightly, but to increase by a larger amount both the fluctuations of the rotor thrust (Mycek et al., 2014) and the root bending moments in the blade sections (McCann, 2007). Furthermore, at most of the sites considered suitable for tidal stream systems, waves and current co-exist (Norris and Droniou, 2007). Such load variation directly influences fatigue design, which means that turbulent characteristics are expected to play a crucial role in defining system life expectancy and cost of equipment.

2.2 Flow Conditions at Tidal Stream Sites

Sites typically considered suitable for electricity generation include locations with mean current due to spring tides of 3-4 m/s (ABPmer, The Met Office & Proudman Oceanographic Laboratory, 2004) and water depths of 40 m (ETSU, 1993). A tidal stream is a slowly-varying oscillatory flow, which means that the flow experienced by a horizontal-axis tidal stream turbine is typically considered as a quasi-steady process (McAdam et al., 2010; Milne et al., 2011). However the flow is complex with turbulence intensity in the range 10-20% (Sutherland et al., 2012; Thomson et al., 2012), surface waves of periods around 5-9 s (Harrald et al., 2010) and depth-varying velocity profiles such as following $1/7^{th}$ power law (Kawase et al., 2011; Batten et al., 2008). The oscillatory incident flow due to waves occurring with current may be reproduced in laboratory conditions if aligned. However, as a result of the specific flow constriction of sites, the incident waves may propagate to a particular direction relative to the mean current (Lewis et al., 2014). The ambient velocity varies over the water depth. Both log-law and power-law profiles have been considered, although field measurements (Polagye and Thomson, 2013; Gunn and Stock-Williams, 2013) indicate that more complex sheared and parabolic profiles may develop.

Although several studies have been published concerning tidal resource assessments and the practical extent of deployment, these studies have mainly focused on smoothly-varying flow speeds. At present, there is limited published information regarding the environmental conditions at potential deployment sites and the effects on tidal device performance (Blackmore et al., 2013). However, data is increasingly becoming available, including from two tidal stream sites in Puget Sound, WA (Gooch et al., 2009; Polagye and Thomson, 2013; Thomson et al., 2012), from test sites in the Orkney Isles, UK (Sutherland et al., 2012) and other potential deployment sites.

In Scotland, the energy resource and potential deployment of wave and tidal energy devices was highlighted in the report of Harrald et al. (2010). The size of the wave, tidal resource and the infrastructure were estimated using a Geographical Information System (GIS). Two potential sites were proposed around the area of Mull of Kintyre and Southwest of Islay. The features at the Mull of Kintyre comprised annual mean speeds of 1.5-3 m/s with waves of heights between 1.4 and 1.6 m and periods of 6.2 and 6.4 s. In contrast, the Southwest of Islay provided annual mean spring velocities of 1.1-3.6 m/s, neaps between 0.6-1.9 m/s and wave heights of 1.3-2.6 m with a period of 6.8 s. The water depths at the sites were 10-30 m and 50-100 m respectively.

Perhaps one of the most documented locations is the Falls of Warness located at the European Marine Energy Centre (EMEC, UK) in the Orkney Isles where the flow experienced is described as a current co-existing with waves. The tidal stream test-site is located 2 km off Billia Croo Bay. The water depth is between 45 and 50 m and the currents resulting from spring and neap tides are 1.44 m/s and 3.34 m/s, respectively. The average significant wave height is 1.9 m with a zero up-crossing period of 5.9 s.

Hs (m)	Tz (s)						
	1.5	2.5	3.5	4.5	5.5	6.5	7.5
0.25	7.14	0.69	0.10				
0.75		26.78	27.16	0.58	0.03		
1.25			9.39	2.10	0.28	0.05	
1.75			0.79	8.09	5.83	0.06	0.02
2.25			0.02	2.05	2.97	1.05	0.19
2.75				0.31	2.31	1.20	0.26
3.25					0.22	0.25	0.07

Figure 2.1 Wave scatter diagram for a tidal stream site in the Orkney Isles (McCann et al., 2008).

A detailed wave scatter diagram for the same location is also provided by McCann et al. (2008), Figure 2.1. Most of the occurring waves have amplitudes of 0.75 m and periods of 2.5 to 3.5 seconds. In view of these short periods, it is likely that waves are propagated in the same direction as the current. Waves of up to 13 m height have been suggested to appear in extreme conditions about every ten years (Norris and Droniou, 2007).

2.3 Modelling Methods for Individual Turbines

The aim of turbine manufacturers is to design a commercially viable method of generating electricity from tidal streams. This requires many considerations including accurate prediction of power output and loading of a particular rotor. Furthermore, the device must withstand the mechanical loading and be able to survive in the harsh environmental conditions of deployment sites.

In the design of a reliable system, it is necessary to anticipate the operating loads and, importantly, the loads most likely to occur in a given return period. The return period selected may differ with component but is likely to be of the order of 10-20 years, typical of offshore wind turbines structures. Operating loads are related to the performance curve of the turbine, usually termed the power curve.

The power curve relates the steady power and thrust behaviour of the turbine to its rotational speed and is determined by several characteristics of the turbine, such as geometry of the blade and rotor size. Various computer codes are available to predict the power curve of a rotor. The comparisons between simulations and experiments conducted on a particular prototype serve to modify and improve the design, as well as to lower costs, select materials and certify design. Some of the numerical codes utilised by the wind industry are: GH Bladed, TurbSim, Aerodyn, NuMAd (Manwell et al., 2002), among others.

These prediction tools are based on different approaches, each having some advantages and limitations over others. Computational programs implementing Computational Fluid Dynamics (CFD) have the advantage of providing good approximations of the turbine's hydrodynamics, but demand more computational resources. There are other simple methods to predict performance curves such as the Vortex Theory, the Actuator Disc method, Cascade Theory (as employed in Turbo machinery), Blade Element Theory (BET), and Blade Element Momentum Theory (BEM), among others.

2.4 Studies of Rotors in Uniform and Sheared Flows

Various methods have been employed to analyse rotor performance in uniform flows. Numerical codes implementing BEM theory have been shown to be suitable for predicting the power curve of wind turbines (Sedaghat and Mirhosseini, 2012; Velázquez et al., 2014). BEM theory describes the turbine's performance in steady conditions, but corrections such as blade-tip losses and modifications such as sheared and time-varying inflow velocities are included to predict loading resulting from unsteady flow in a quasi-steady approach. One of the limitations and difficulties of BEM arises when trying to predict the turbine wake and its transient unsteady loading conditions. Sometimes these results can give an unrealistic power, but, in general, it is a reliable and simple tool (Moriarty and Hansen, 2005).

Several engineering tools that incorporate BEM theory have been extended to predict steady performance of tidal stream turbines, providing good agreements with scale device experiments (Bahaj, Batten, et al., 2007; McCann, 2007; Lee et al., 2011; Togneri and Masters, 2011). Some published studies have considered the BEM method to assess the turbulent and sheared flow fields imparted on tidal stream turbines. Flow fluctuations across the rotor modify the blade loading and thus cause transient and unsteady loads. At present, most of the rotor loading that has been analysed is due to specific turbulence models. For instance, Togneri et al. (2011) analysed the rotor power using both synthesised and measured time histories of mean flow with turbulence of a 5-minute sample length each. The BEM predictions of power using the measured and predicted flow kinematics were 10-15% higher than that obtained in a uniform flow. The turbulent flow fluctuations imparted on the rotor also affect the fatigue loading and blade root moments. The influence of these unsteady loads on the design life of tidal turbine blades is an important design consideration (McCann, 2007).

Various numerical approaches have coupled the resistance forces due to the rotor with the governing continuum equation of the operating fluid with turbulence modelled by the Reynolds averaged-Navier Stokes (RANS) equations, or by Large-Eddy Simulation (LES). The RANS numerical methods provide the physical phenomenon in a time-averaged sense and are relevant for obtaining the rotor's performance (Afgan et al., 2013) and large-scale effects such as the numerical investigation of the tidal stream modification (Batten et al., 2013). LES techniques are preferred to RANS due to the higher flow resolution, particularly for understanding the flow interaction through the blades, such as in uniform flow with turbulence present. However, they require more computational resources (McNaughton et al., 2012). These sets of differential formulas are based on alternative closure models with models such as $\mathrm{k}-\epsilon$ and $\mathrm{k}-\omega$ models widely employed for wind industry applications. A range of methods can be used for the representation of tidal turbines or turbulent onset flow in CFD simulations. These approaches vary in complexity and computational cost. Forcing of a tidal rotor has been represented with the Actuator disc (Batten et al., 2013), Actuator line (Churchfield et al., 2013), embedded blade element actuator disc methods (Harrison, Batten, and Bahaj, 2010; Edmunds et al., 2014) and Blade Resolved methods (Afgan et al., 2013), amongst others.

Techniques based on the Actuator Disc Method replace the counteracting torque generated by the blades on the incident flow with the concept of a stationary disc, which exerts resistant forces or momentum sinks in the axial flow (Harrison, Batten, Myers, and Bahaj, 2010). For this method, the swirl in the disc's wake is not modelled and flow recovery might be different to a rotor at a different downstream position (Tedds et al., 2014). A few experimental formulas for flow recovery have been obtained from the rotor to far downstream positions, but have been limited to interactions of a single turbine (Crasto et al., 2012).

The actuator disc has been employed to analyse the wake in turbulent flows with different length scales, along with the flow characterisation and proximity effects of rotor deployment (Myers et al., 2008; Bahaj et al., 2012; Fallon et al., 2014; Tedds et al., 2014) .The motive for the disc employment includes the simplicity in modelling of a disc instead of rotating blades, as well as the reduced computational work and the lab-scale agreement with flow characteristics behind single rotors. They also have served as a proper estimate of the extraction rate of tidal resources and impact on the natural flow field (Bryden and Couch, 2006; Myers and Bahaj, 2006; Harrison, Batten, and Bahaj, 2010; Batten et al., 2013).

CFD models using actuator lines employ rotating lines acting as momentum sinks to the onset flow. For blade-resolved methods, the full rotating blade is meshed, but this requires high cell density close to the blades and therefore is a computationally expensive method. Blade-resolved methods using RANS and LES have been found suitable for rotor performance in uniform and sheared flows including with large values of turbulence length-scale representative of conditions at test sites (Afgan et al., 2013).

An advantage of CFD models is the fluid flow resolution and the prediction of unsteady wake characteristics lacking in the BEM theory alone. However, the major drawback is the required computational resources. For instance, to obtain results for a single operating condition on a typical desktop Personal Computer (PC), approximately 6 hours are required using a CFD model compared to around 0.02 s for a BEM model (Chapman et al., 2013). Therefore, BEM models remain popular for the design of both wind and tidal stream devices.

2.5 Blade Element Momentum Theory

The horizontal loading and power of a horizontal-axis turbine are both dependent on the blade geometry and the rotational speed of the rotor. The Blade Element Momentum (BEM) method is often used to relate lift and drag curves for each section of the blade to the net thrust coefficient (C_{T}) and power coefficient (C_{P}) of a turbine rotor. The design software GH Bladed is based on the BEM theory and is widely used today for both wind and tidal stream turbine design. BEM is a combination of the Linear Momentum Theory (LMT) and Blade Element Theory (BET).

Momentum theory is a control-volume method that describes the horizontal force due to the pressure drop produced by a disc or arbitrary object across an incident, steady flow. The Blade Element Theory states two perpendicular forces are generated at the blade sections based on the geometry of the blade and the characteristics of the imparted flow. The relationship of thrust and power from the two theories allows an iterative procedure to calculate the performance characteristics of all sections along a blade. The variation of net thrust and power with rotational speed are then calculated by integrating the local components of blade loading along the blade length for each flow speed.

2.6 Linear Momentum Theory

Momentum Theory is often used to estimate the horizontal force on a disc or area, across which a pressure drop occurs. The basis of the Linear Momentum Theory is that the force due to the rate of change of momentum of a fluid between upstream and downstream of an object is equivalent to the force due to the pressure imposed on the same object. In the context of wind-turbine models, the approach is often applied to an actuator disc, which is commonly represented as a disc located within a stream tube (Figure 2.2). If a pressure drop is imposed across the disc, flow velocity must reduce from upstream, through the disc to downstream. Since mass flux is conserved, the sectional area of the stream tube that passes the disc increases from upstream, through the disc to downstream. The fluid pressure recovers asymptotically to the undisturbed condition at the far downstream, referred to as the region of the far wake. At this location, the flow's kinetic energy is reduced and its static pressure is in equilibrium with the upstream condition. Ignoring heat dissipation and losses occurring across the wake, the energy relationships of incompressible fluids are applied to different parts of the stream tube. Subsequently, various equations are developed to relate velocity and pressure at upstream, disc and wake positions to force imposed on the flow by the body.

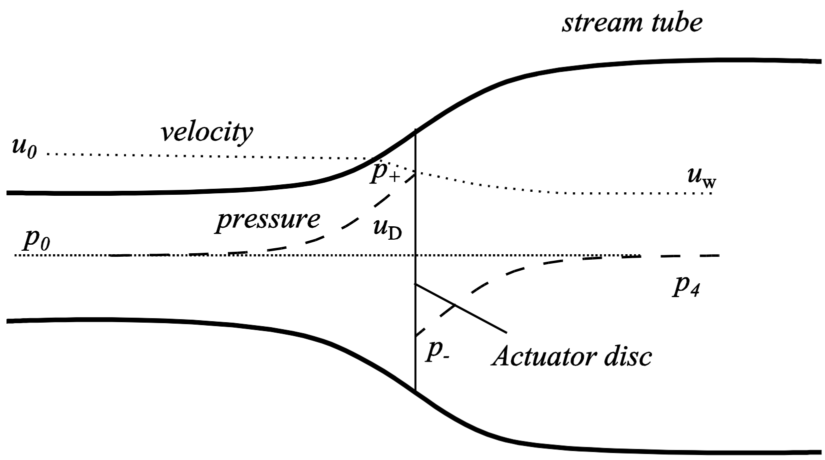

Figure 2.2 Actuator disc modified from Burton et al. (2001). Mass flow rate (ρAU) has to be equal for all locations, hence the cross-sectional area of the stream tube at the wake increases to compensate for reduced velocity.

The key points from Burton et al. (2001) and Manwell et al. (2002) regarding this method are as follows:

- The velocity decreases from the free stream to the wake. The axial induction factor is defined from the relationship between the free stream velocity and the disc velocity, as:

$$\mathrm{a}_{\mathrm{axial}} = (u_0 - u_{\mathrm{D}})/u_0 \qquad \text{Eq. 2.1}$$

- The disc and wake velocity are given in terms of the free stream velocity and axial induction factor, $\mathrm{a}_{\mathrm{axial}}$:

$$u_{\mathrm{D}} = u_0(1 - \mathrm{a}_{\mathrm{axial}}) \qquad \text{Eq. 2.2}$$

$$u_{\mathrm{w}} = u_0(1 - 2\mathrm{a}_{\mathrm{axial}}) \qquad \text{Eq. 2.3}$$

If the axial induction factor is greater than half (≥0.5), Eq. 2.3 becomes negative ($u_{\mathrm{w}} \leq 0$) and unreal. The Momentum Theory breaks down and beyond this limiting point, other empirical techniques need to be employed. Section 2.9 addresses some of the correct formulae utilised for high axial induction factors.

- The pressure difference across the actuator disc produces a dynamic force:

$$F_{\text{dynamic}} = \frac{1}{2}\rho u_0{}^2 A \qquad \text{Eq. 2.4}$$

- The thrust coefficient is defined as the ratio of the thrust (T), or force acting on the actuator, to the dynamic force. It is expressed as:

$$C_{\text{T}} = \frac{T}{F_{\text{dynamic}}} = 4\text{a}_{\text{axial}}(1 - \text{a}_{\text{axial}}) \qquad \text{Eq. 2.5}$$

- The power extracted equals to the horizontal force multiplied by the velocity at the disc. The power coefficient, C_{P}, is the ratio of power extracted by the rotor (P_{p}) to that available in the wind. The power coefficient is defined as:

$$C_{\text{P}} = \frac{2P_{\text{p}}}{\rho A u_0{}^3} \qquad \text{Eq. 2.6}$$

- In terms of the axial induction factor, the power coefficient is:

$$C_{\text{P}} = 4\text{a}_{\text{axial}}(1 - \text{a}_{\text{axial}})^2 \qquad \text{Eq. 2.7}$$

- For unbounded flows, there exists a theoretical maximum power coefficient that a turbine is capable of obtaining, irrespective of its size, blade shapes or other parameters; this is known as the Betz limit. Today all wind turbines operate below this quantity. In the case of tidal turbines, the power coefficient is able to exceed this limit due to blockage (Nishino and Willden, 2012). The values for the Betz limits are:

$$\text{a}_{\text{axial}} = 1/3 \qquad \text{Eq. 2.8}$$

$$C_{\text{P-max}} = 0.593 \qquad \text{Eq. 2.9}$$

- Wind turbines extract energy by simultaneously slowing down and exerting a mechanical torque on the undisturbed flow. The counteracting torque is transmitted to a shaft, which is then coupled to an electrical generator. The flow leaving the rotor proceeds to the far downstream with increased angular momentum. Extending momentum analysis with the wake rotation, a tangential induction factor,a_{T}, is multiplied on the tangential velocity component ($\text{a}_{\text{T}}\omega r$).
- The thrust and torque calculation involve the axial and tangential induction factors. These are:

$$dT = 4\text{a}_{\text{axial}}\rho u_0{}^2(1 - \text{a}_{\text{axial}})\pi r dr \qquad \text{Eq. 2.10}$$

$$dQ = 4a_T \rho u_0 (1 - a_{axial}) \pi r^3 \omega dr \qquad \text{Eq. 2.11}$$

2.7 Blade Element Theory

Blade Element Theory was first proposed by William Froude in the 1870s and has been applied to the analysis of propellers and helicopters. This method demonstrates an examination of the rotor characteristics, the nature of the flow and loading on the blade. The approach consists of separating the blade into a number of small segments where two perpendicular forces, named lift and drag, are generated by flow at an angle of attack (α). The definitions of the lift and drag provide the spanwise components of the normal force and blade's torque.

The local forces of lift and drag are related to a drag coefficient (C_d) and lift coefficient (C_l). Values of these coefficients vary according to the angle of attack. Their magnitude is dependent on the pressures generated across the aerofoil, the surface roughness, the operating Reynolds number and the geometry of the blade. Experimental measurements in wind tunnels or numerical panel methods such as XFOIL are usually employed to quantify the aerofoil characteristics (C_d, C_l) for a range of Reynolds numbers, $Re = \frac{u_0 D_l}{\nu}$, where D_l is a length characteristics such as chord and ν is the kinematic viscosity.

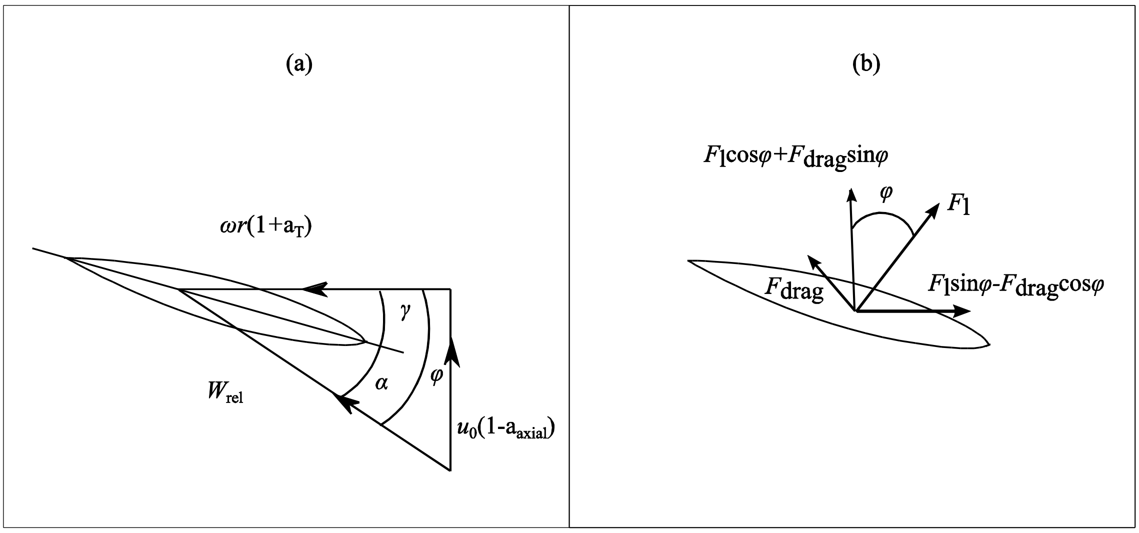

Figure 2.3 Forces and velocities obtained in a section of the blade. a) Diagram of the velocities and the angles obtained, based on Burton et al. (2001). b) Lift and drag forces indicated with the corresponding angle of attack.

The main points of BET as stated in Manwell et al. (2002) are:

- The turbines use aerofoil devices in the shape of blades, to produce lift and drag from the flow incident motion and relative position. From mathematical analysis, we can write the angle of relative wind to the cross-section of a blade (see Figure 2.3) as:

$$\tan\varphi = \frac{u_0(1 - \mathrm{a}_{\mathrm{axial}})}{\omega r(1 + \mathrm{a}_{\mathrm{T}})} = \frac{1 + \mathrm{a}_{\mathrm{axial}}}{TSR(1 + \mathrm{a}_{\mathrm{T}})} \qquad \text{Eq. 2.12}$$

- The angle of attack is the angle between the chord line and the velocity relative to the free stream flow, W_{rel}. In terms of the blade-pitch angle, γ, the angle of attack is defined as:

$$\alpha = \varphi - \gamma \qquad \text{Eq. 2.13}$$

- The Tip-Speed Ratio is the ratio of the rotor's tangential velocity to the free-stream flow:

$$TSR = \omega R/u_0 \qquad \text{Eq. 2.14}$$

- Similarly, the local speed ratio is relative to the blade section as:

$$TSR_{\mathrm{r}} = \omega r/u_0 \qquad \text{Eq. 2.15}$$

- For convenience, the out of plane (or axial) and in-plane components are:

$$C_{\mathrm{x}} = C_{\mathrm{l}}\cos\varphi + C_{\mathrm{d}}\sin\varphi \qquad \text{Eq. 2.16}$$

$$C_{\mathrm{y}} = C_{\mathrm{l}}\sin\varphi - C_{\mathrm{d}}\cos\varphi \qquad \text{Eq. 2.17}$$

- The chord solidity is expressed as a function of the number of blades, B, as:

$$\sigma_{\mathrm{r}} = Bc/(2\pi r) \qquad \text{Eq. 2.18}$$

- The normal force and torque are:

$$dF_{\mathrm{N}} = \frac{1}{2}B\rho {W_{\mathrm{rel}}}^2(C_{\mathrm{l}}\cos\varphi + C_{\mathrm{d}}\sin\varphi)cdr \qquad \text{Eq. 2.19}$$

$$dQ = \frac{1}{2}B\rho {W_{\mathrm{rel}}}^2(C_{\mathrm{l}}\sin\varphi - C_{\mathrm{d}}\cos\varphi)crdr \qquad \text{Eq. 2.20}$$

2.8 Blade Element Momentum Theory

Blade Element Momentum Theory incorporates the thrust definition in Momentum Theory with the net normal force from the Blade Element Theory. This approach follows from relating the rate of change of momentum of flow across an annular section to the force applied to the blade elements within the same annulus. To obtain the net force and power on a blade, the blade is typically split into several elements with aerofoil cross-sections. The combining of definitions from both theories produces new relationships for the differential thrust (Eq. 2.10 and Eq. 2.19) and torque (Eq. 2.11 and Eq. 2.20) as:

$$dT = \frac{\rho \sigma_{\mathrm{r}} \pi u_0{}^2 (1 - \mathrm{a}_{\mathrm{axial}})^2 r C_{\mathrm{x}} dr}{(\sin \varphi)^2} \qquad \text{Eq. 2.21}$$

$$dQ = \frac{\rho \sigma_{\mathrm{r}} \pi u_0{}^2 (1 - \mathrm{a}_{\mathrm{axial}})^2 r^2 C_{\mathrm{y}} dr}{(\sin \varphi)^2} \qquad \text{Eq. 2.22}$$

The different thrust and power coefficients are made non-dimensional with the available power $(F_{\mathrm{dynamic}} u_0)$ and thrust of the incident flow:

$$dC_{\mathrm{T}} = \frac{dT}{\frac{\rho \pi R^2 u_0{}^2}{2}} \qquad \text{Eq. 2.23}$$

$$dC_{\mathrm{P}} = \frac{dP_{\mathrm{p}}}{\frac{\rho \pi R^2 u_0{}^3}{2}} \qquad \text{Eq. 2.24}$$

Likewise, the thrust coefficient at each annulus section is obtained using the volume-control method of Linear Momentum Theory and is given by Hansen (2012) as:

$$C_{\mathrm{T}} = \frac{dT}{\frac{1}{2} \rho u_0{}^2 2 \pi r dr} \qquad \text{Eq. 2.25}$$

Therefore, equating the Momentum thrust coefficient (Eq. 2.5) with BEM (Eq. 2.21 with Eq. 2.25), the (local) thrust-combined coefficient is:

$$C_{\mathrm{T}} = 4\mathrm{a}_{\mathrm{axial}} (1 - \mathrm{a}_{\mathrm{axial}}) = \frac{(1 - \mathrm{a}_{\mathrm{axial}})^2 \sigma_{\mathrm{r}} C_{\mathrm{x}}}{(\sin \varphi)^2} \qquad \text{Eq. 2.26}$$

Eq. 2.16 and Eq. 2.17 are based on lift and drag coefficients obtained for a 2-dimensional foil section and therefore flow along the blade is neglected. For the majority of the blade this is typically an acceptable assumption. However, at the hub and tip of the blade the flow may become 3-dimensional. Hub and tip loss correction factors are therefore often applied to the thrust definition of Eq. 2.26. Tip losses developed by Prandlt are employed in the present BEM model.

The Prandlt tip loss formula is commonly used to represent wind rotors and is given by Hansen (2012) as:

$$F_{\mathrm{k}} = \left(\frac{2}{\pi}\right)\cos^{-1}\left[\mathrm{e}^{-\mathrm{f_k}}\right] \qquad \text{Eq. 2.27}$$

where

$$\mathrm{f_k} = \frac{B(R-r)}{2r\sin\varphi} \qquad \text{Eq. 2.28}$$

Another variation of the tip losses for marine blades is given by Batten et al. (2007):

$$F_{\mathrm{k}} = \left(\frac{2}{\pi}\right)\cos^{-1}\left[\cosh 7\left(\frac{r}{R}\mathrm{f_k}\right)/\cosh)\mathrm{rf_k})\right] \qquad \text{Eq. 2.29}$$

where

$$\mathrm{f_k} = \left(\frac{BR}{2r\tan\varphi} - 0.5\right) \qquad \text{Eq. 2.30}$$

Hub losses may also be added to the tip losses and include total losses (Moriarty and Hansen, 2005; Chapman et al., 2013). It becomes:

$$F_{\mathrm{loss}} = F_{\mathrm{k}}F_{\mathrm{H}} \qquad \text{Eq. 2.31}$$

where the hub losses are defined relative to the hub radius, R_{hub} as:

$$F_{\mathrm{H}} = \left(\frac{2}{\pi}\right)\cos^{-1}\left[\mathrm{e}^{-\mathrm{f_H}}\right] \qquad \text{Eq. 2.32}$$

and

$$\mathrm{f_H} = \frac{B(r-R_{\mathrm{hub}})}{2r\sin\varphi} \qquad \text{Eq. 2.33}$$

These two formulas for tip losses are evaluated in the simulations of the next chapters. Applying losses to the thrust of Eq. 2.26, the local axial and tangential induction factors become (Manwell et al., 2002; Hansen, 2012):

$$\mathrm{a_{axial}} = \frac{1}{\frac{4F_{\mathrm{k}}(\sin\varphi)^2}{\sigma_{\mathrm{r}}C_{\mathrm{x}}} + 1} \qquad \text{Eq. 2.34}$$

$$\mathrm{a_T} = \frac{1}{\frac{4F_{\mathrm{k}}(\sin\varphi\cos\varphi)}{\sigma_{\mathrm{r}}C_{\mathrm{y}}} - 1} \qquad \text{Eq. 2.35}$$

The local power coefficient from Eq. 2.22 and Eq. 2.24 becomes:

$$dC_{\mathrm{p}} = \frac{dQ\omega}{\frac{1}{2}\rho\pi R^2 {u_0}^3} = \frac{2\sigma_{\mathrm{r}}(1-\mathrm{a_{axial}})^2 C_{\mathrm{y}} r^2 \omega dr}{(\sin\varphi)^2 u_0 R^2} \qquad \text{Eq. 2.36}$$

Recalling Tip-Speed Ratio from Eq. 2.14 and substituting with the power (Eq. 2.36) and previous thrust relationship (Eq. 2.21 and Eq. 2.23). The power and thrust coefficients become:

$$dC_{\mathrm{p}} = \frac{2TSR\sigma_{\mathrm{r}}(1 - \mathrm{a}_{\mathrm{axial}})^2 C_{\mathrm{y}} r^2 dr}{(\sin\varphi)^2 R^3} \qquad \text{Eq. 2.37}$$

$$dC_{\mathrm{T}} = \frac{2\sigma_{\mathrm{r}}(1 - \mathrm{a}_{\mathrm{axial}})^2 C_{\mathrm{x}} r dr}{(\sin\varphi)^2 R^2} \qquad \text{Eq. 2.38}$$

In Batten et al. (2008), these expressions of thrust and power coefficients are equally obtained for a BEM numerical solver with the solidity ratio and local radii defined as $\sigma_{\mathrm{r,a}} = \frac{Bc}{2\pi R}$ and $r_{\mathrm{R}} = r/R$. The net characteristics such as axial, tangential flow induction factors, forces, and power coefficients are finally calculated by summing all the local components along the blade.

2.9 High axial Induction Factor

For axial induction factors greater than half, the wake velocity predicted by the Momentum Theory becomes negative and, therefore, non-physical. In this state, shear-flow instabilities begin to occur at the boundaries of the wake, hence forming several circulating currents, named as eddies, along this region. As a result of the eddies, additional flow energy is then transferred from outside of the stream tube into the wake, thus causing a higher pressure drop across the rotor than that predicted with a disc approach. This is referred to as the turbulent-wake state and empirical relationships are commonly used over the range $0.5 < \mathrm{a}_{\mathrm{axial}} < 1$ to describe the increase of thrust as the solidity of the rotor is increased. Several formulations and descriptions of thrust exist for the high axial induction factor range. Some of the conventional routines implemented into BEM models are summarised in Table 2.1. The total losses, F_{loss}, may replace the tip losses, F_{k} shown in Table 2.1.

Table 2.1 Corrected formulas of the thrust coefficient.

Method	Thrust Formula	Range
Spera (Hansen, 2012)	$C_{\mathrm{T}} = 4(\mathrm{a_c}^2 + (1 - 2\mathrm{a_c})\mathrm{a_{axial}})F_{\mathrm{k}}$	$\mathrm{a_{axial}} > \mathrm{a_c}$ $\mathrm{a_c} = 0.2 - 0.3$
Tidal Bladed (Bossanyi, 2007)	$C_{\mathrm{T}} = (0.6 + 0.61\mathrm{a_{axial}} + 0.79\mathrm{a_{axial}}^2)F_{\mathrm{k}}$	$\mathrm{a_{axial}} > 0.3539$
Buhl (Buhl, 2005)	$C_{\mathrm{T}} = \frac{8}{9} + \left(4F_{\mathrm{k}} - \frac{40}{9}\right)\mathrm{a_{axial}} + \left(\frac{50}{9} - 4F_{\mathrm{k}}\right)\mathrm{a_{axial}}^2$	$\mathrm{a_{axial}} > 0.4$

The previous experimental studies were formulated to correct the net thrust on a disc in incident steady flow. In practice, the flow behaviour along the annular sections of the rotor is acceptable and thus the equations of Table 2.1 are often applied to model the forcing on the blade elements. The new (high) axial induction factor is therefore calculated by replacing momentum thrust (Eq. 2.26) with empirical formulas for thrust. These are shown in Table 2.2.

The rotor performance depends heavily on the blade design (radial variation of the axial induction factor) and some variation could occur by employment of a particular high thrust formula (Buckland et al., 2010). The Tidal Bladed and Buhl formula implemented in BEM codes have been found suitable to predict power and improve thrust prediction of tidal rotors (Buckland et al., 2010; Masters et al., 2011; Chapman et al., 2013). However, it has been found that for several prototype rotor designs operating in relatively unconstrained conditions, the majority of the local axial induction factors along the blade (apart from at the tip and at high Tip-Speed ratios) tend to reside in the valid range of the Momentum Theory (Batten et al., 2008). As a result, fairly consistent power and thrust outputs are obtained regardless of the formula for the high axial induction factor employed.

Table 2.2 High axial induction factors using the Spera, Tidal and Buhl method.

Thrust	High axial induction factor
Spera	$= 1/2\left(2 + \mathrm{K_{spera}}(1 - 2\mathrm{a_c}) - \sqrt{\left(\mathrm{K_{spera}}(1 - 2\mathrm{a_c}) + 2\right)^2 + 4\left(\mathrm{K_{spera}}\mathrm{a_c}^2 - 1\right)}\right)$ where $\mathrm{K_{spera}} = \frac{4F_\mathrm{k}(\sin\varphi)^2}{\sigma_\mathrm{r} C_\mathrm{x}}$ $\quad \mathrm{a_c} = 0.2$
Tidal Bladed	$= \frac{-(1(61F_\mathrm{k}\sin\varphi^2 - 100\sin\varphi\,(8C_\mathrm{x}\sigma_\mathrm{r}F_\mathrm{k} - 1.5239{F_\mathrm{k}}^2\sin\varphi^2)^{0.5} + 200C_\mathrm{x}\sigma_\mathrm{r}}{158F_\mathrm{k}\sin\varphi^2 - 200C_\mathrm{x}\sigma_\mathrm{r}}$
Buhl	$= \frac{18\sigma_\mathrm{r}C_\mathrm{x} - 40(\sin\varphi)^2 - 9(\sin\varphi)\left(16{F_\mathrm{k}}^2(\sin\varphi)^2 - 64F_\mathrm{k}\frac{(\sin\varphi)^2}{3}\right)^{0.5}}{18\sigma_\mathrm{r}C_\mathrm{x} - 100(\sin\varphi)^2 + 72F_\mathrm{k}(\sin\varphi)^2} + \frac{8\sigma_\mathrm{r}C_\mathrm{x} + 36F_\mathrm{k}(\sin\varphi)^2}{18\sigma_\mathrm{r}C_\mathrm{x} - 100(\sin\varphi)^2 + 72F_\mathrm{k}(\sin\varphi)^2}$

2.10 Blockage Correction

Corrections may be required to performance prediction of tidal stream turbines due to the blockage ratio (ε) defined as the ratio of sectional area of the rotor to that of the channel. Contrary to flows incident to wind turbines, the shallow waters considered for tidal turbine deployment have boundary effects from the seabed, water surface and finite channel width, or adjacent turbine spacing, that alter loading and performance relative to a turbine in unbounded flow. Following Linear Momentum Theory, a correction to the thrust and power coefficient may be derived.

Presently, a few correction methods exist for the blockage ratio obtained within an array of rotor lines across the channel width accounting for an actuator disc within a channel of finite cross-sectional area. In the case of a single turbine, a tunnel correction approach has been shown as suitable (Bahaj, Molland, et al., 2007). For this approach, the volume control of the Linear Momentum Theory introduces a pressure drop in the bypass flow that surrounds the wake and the Bernoulli principle is applied to both the stream tube occupied by the disc and to the bypass flow. The formulation and derivation procedures are shown in Appendix A.

The aim of the method is to find the incident velocity (u_{0c}) for an unbounded flow, which generates a rotor power and thrust equivalent to that produced with an identical rotor that is operating in a bounded flow. The experimental measurements in the bounded flow are then normalised with the unbounded flow and compared to the BEM simulations.

To calculate the unbounded velocity, the incident velocity (u_0), the blockage ratio, the torque (Q), and thrust (T), are obtained straightforwardly from experimental measurements. The bypass velocity, u_b, is estimated by iterating for the incident disc, u_D, and wake velocity components, u_w, as:

$$u_\mathrm{D} = \frac{u_\mathrm{w}(u_\mathrm{b} + u_\mathrm{w})}{u_\mathrm{b} + 2u_\mathrm{w} - u_0} \qquad \text{Eq. A.16}$$

$$u_\mathrm{b} = \frac{u_0 - u_\mathrm{w} + \sqrt{\varepsilon u_0{}^2 - 2\varepsilon u_0 u_\mathrm{w} + (1 - \varepsilon + \varepsilon^2)u_\mathrm{w}{}^2}}{1 - \varepsilon} \qquad \text{Eq. A.20}$$

$$u_\mathrm{w} = \sqrt{\frac{-T}{0.5\rho A} + u_\mathrm{b}{}^2} \qquad \text{Eq. A.21}$$

Once the bypass, disc and wake velocity have been converged. The equivalent incident velocity to a bounded flow becomes:

$$u_{0\mathrm{c}} = u_\mathrm{D} + \frac{(u_\mathrm{b}{}^2 - u_\mathrm{w}{}^2)}{4u_\mathrm{D}} \qquad \text{Eq. A.25}$$

From Eq. A.25, the equivalent incident velocity is then used to correct the experimental TSR, thrust and power coefficients as:

$$C_\mathrm{T} = \frac{T}{0.5A\rho u_{0\mathrm{c}}{}^2} \qquad C_\mathrm{P} = \frac{Q\omega}{0.5A\rho u_{0\mathrm{c}}{}^3} \qquad TSR = \frac{\omega R}{u_{0\mathrm{c}}}$$

The other correction method is to rewrite the BEM model for bounded flows. Direct comparison with experiments (Whelan et al., 2009a) indicated that this method is suitable only for low rotational speeds, typically of TSRs less than 4.

2.11 Iterative Solution to Obtain Axial and Radial Induction Factors

An iterative procedure based on the BEMT of Sections 2.8 and 2.9 is implemented to obtain power curves for a given rotor geometry and corresponding aerofoil performance data for the operating Reynolds range. The blade is divided into numerous small segments and for each element, the performance characteristics such as power, thrust, torque and horizontal load against TSR are calculated for each section and the entire blade. The overall procedure is summarised as follows:

1. Define TSR of interest (Eq. 2.14).
2. Define blade geometry.
3. Define blade lift and drag characteristics.
4. Analyse a blade section.
5. At each section, assign local values of φ, C_{x}, C_{y}, F_{loss} (Eq. 2.12, Eq. 2.16, Eq. 2.17 and Eq. 2.31).
6. Find the local Tip-Speed Ratio and chord solidity (Eq. 2.15 and Eq. 2.18)
7. Calculate the axial and tangential induction factors, $\mathrm{a}_{\mathrm{axial}}$ and a_{T} respectively (Eq. 2.34 and Eq. 2.35).
8. If the axial induction factor is high, use one of the empirical formulas (Table 2.2).
9. Find φ (Eq. 2.12).
10. Work out the value of α (Eq. 2.13).
11. Get C_{d} and C_{l} from published graph and subsequently φ, C_{x}, C_{y}, F_{loss} (Eq. 2.12, Eq. 2.16, Eq. 2.17 and Eq. 2.31).
12. Repeat steps 4-11 until the local axial and tangential induction factors converge.
13. Obtain the local axial and tangential induction factors across the entire blade.
14. Estimate C_{P} and C_{T} across the entire radius (Eq. 2.37 and Eq. 2.38).
15. Repeat steps 1-15 for another TSR of interest.
16. Evaluate power and thrust coefficients against the range of TSRs.

An advantage of this method compared to CFD models is its efficiency and simplicity due to the small requirements of computational work (Chapman et al., 2013). The solution of power and thrust is obtained in few steps.

2.12 Unsteady Incident Flows

Unsteady load is considered herein as oscillation of the imposed flow to the rotor resulting from waves and linear horizontal motion due to the support structure. These operating conditions induce speed oscillations on the rotor blades, thus producing time-varying forces. Concerning the wave oscillatory loading on single rotors, BEM modified versions including kinematics due to presence of waves have been developed to predict mean rotor performance, blade loading and root moment (Galloway, 2013; Luznik et al., 2013). However, these studies have been limited to flows without turbulence and for a range of finite waves. For instance, Barltrop et al. (2007) studied the oscillatory loading imposed on a 3-bladed turbine that had been towed through generated waves. Both torque and thrust were evaluated by combining BEM with linear wave theory to integrate velocities and accelerations of the wave-current incident flow. Measured thrust and torque due to towing at uniform speed through waves agreed well with the numerical simulations (within 10%). It was found that the torque increased with the incoming waves and the mean thrusts remained with the same magnitude. However, some measures may be neglected in this type of towing-tank experiment: these are the wavelength and speed modification due to Doppler shift and consequent change of wave height as well as possible interaction between wave kinematics and turbulence (Galloway et al., 2010). Thus, the use of a wave-current flume is more representative of the natural flow field at a natural site.

Following the previous BEM method in waves, Faudot and Dahlhaug (2012) predicted mean loads with inclusion of blade added mass due to time variation of the axial induction factor. The simulations were contrasted with measurements of a 2-bladed turbine for several wave-current conditions and provided reasonable agreement. The added mass in this method was found to provide only 1% reduction of the thrust prediction. The influence of the wave conditions on the peak rotor forces was not addressed.

Likewise, some works have analysed the response of a rotor oscillating in the streamwise direction using the Morison equation. The Morison equation is a semi-empirical formula usually employed to predict forcing in bluff bodies due to oscillatory flows (Morison et al., 1950). The force is given as a sum of a Froude-Krylov force and a drag, an added mass, which are evaluated from the relative motion between the body and the incident flow:

$$F = \frac{1}{2}\rho A C_{\mathrm{D}}(U_{\mathrm{a}} - \dot{x})|U_{\mathrm{a}} - \dot{x}| + \rho V C_{\mathrm{a}}\left(\dot{U}_{\mathrm{a}} - \ddot{x}\right) + \rho V \dot{U}_{\mathrm{a}} \qquad \text{Eq. 2.39}$$

where C_{D} and C_{a} correspond to the drag and inertia coefficient, V, the volume of the body, x, the body motion, and U_{a} the flow kinematics normal to the body plane. In Eq. 2.39, the Froude-Krylov component, $\rho V \dot{U}_{\mathrm{a}}$, is the force resulting from the pressure change of the undisturbed flow field that is applied to the wetted surface area of the body. Due to this approximation, the Froude-Krylov force is only valid for slender structures in long waves, with typical dimensions of the body, e.g. diameter over the wavelength, $\frac{D}{L_{\mathrm{w}}}$, being less than 0.2 (Lehmann, 2007). For a relatively large structure, $\frac{D}{L_{\mathrm{w}}} > 0.2$, the Morison force is invalid and the force due to disturbance of the pressure field by the body, named as the diffraction force, is hence more appropriate.

Two types of oscillatory flow may be considered for which the forcing differs. Firstly, a rigid body encountering oscillatory flow, such as in waves. Secondly, motion of a rigid body relative to a non-oscillatory flow, such as a body oscillating in still water or in a mean incident flow. In the case of turbulence being present in a mean flow, the velocity fluctuations due to the turbulent intensity are intrinsically chaotic and thus it becomes challenging to predict its behaviour, as well as the force that is imposed on the body. Here, a Morison force is proposed to account the turbulence influence by using a Reynolds decomposition of the velocity and consequently the imposed force. The velocity is given as the sum of a mean, u_0, and a zero-average fluctuation velocity component, u'. It is:

$$u_{\mathrm{c}} = u_0 + u' \qquad \text{Eq. 2.40}$$

If the mean flow contains a low turbulence intensity, it implies that flow acceleration is small $\dot{u} \approx 0$ and fluctuations of velocity contain magnitudes, which are statistically lesser than the mean component, $u' \ll u_0$.

From this assumption, if a rigid body is in a mean flow with turbulence, the Morison equation (see Eq. 2.39) is obtained with parameters:

$$U_{\mathrm{a}} = u_{\mathrm{c}} \, , \dot{u}_{\mathrm{c}} = 0 \, , x = 0 \qquad \text{Eq. 2.41}$$

Since the differences of the Morison equations (Eq. 2.39) are due to the flow conditions (velocity and acceleration). Below are explained some of the oscillatory flow conditions with their corresponding approach-flow velocities and body motion.

For a rigid body in oscillatory flow due to incoming waves, the velocity of the incident flow and body motion is:

$$U_{\mathrm{a}} = u_{\mathrm{wave}} \, , \dot{x} = 0 \qquad \text{Eq. 2.42}$$

In the case of a rigid body, where the oscillatory flow is due to waves combined with a mean flow, u_0, the velocity is then a sum of each component. The force is obtained with:

$$U_{\mathrm{a}} = u_{\mathrm{wave}} + u_0 \,, \dot{x} = 0 \qquad \text{Eq. 2.43}$$

If the body is oscillating in a flow with zero mean speed, such as a cylinder undergoing streamwise oscillations within a quiescent flow, the velocity becomes:

$$U_{\mathrm{a}} = 0 \qquad \text{Eq. 2.44}$$

Since the Froude-Krilov force is given in function of the time-dependent pressure gradient of the ambient flow applied to the wetted surface area of the body. In the quiescent flow, the pressure gradient of the ambient flow is not time varying and remains as zero. Thus the Froude-Krylov force does not exist.

If the body is oscillating in a mean flow, the drag and inertia that results from the body oscillations is often assumed to remain equal to that obtained in the absence of a mean flow. The velocity of oscillation is:

$$U_{\mathrm{a}} = u_0 \qquad \text{Eq. 2.45}$$

For a body oscillating in a mean flow with turbulence present, the velocity is written:

$$U_{\mathrm{a}} = u_{\mathrm{c}} \qquad \text{Eq. 2.46}$$

This is assuming that the turbulent fluctuations, u', are irregular and set over a wide range of frequencies, such that the frequency of oscillatory part is unaffected by the turbulence intensity.

Following this approach, the velocity of a body oscillating within a flow due to waves combined with a mean flow and turbulence is:

$$U_{\mathrm{a}} = u_{\mathrm{c}} + u_{\mathrm{wave}} \qquad \text{Eq. 2.47}$$

In the thesis, the Morison force due to contribution of the turbulent fluctuations is not simulated. Usually, the turbulent effects are important to consider in a support-structure response, in order to obtain the correct system's output. Since the response of the support force in here, is mostly comprised within a narrow band of frequencies in the low spectrum region and the components of the load fluctuations due to turbulence are mostly located in the high-frequency range. The contribution of the turbulent load within the frequency range of the support response becomes negligible. However in the conditions where the bandwidth of the system force is considerable, such as those obtained with random sea waves (relative large bandwidth), the turbulence and waves effect must be considered. Hence a frequency-response model becomes more appropriate. For this method, a point-by point multiplication would be required between the spectra of input signals (wave-current) and the response of the structure to simulate the system output.

An extensive literature exists for coefficients and hydrodynamics of a circular cylinder in oscillating flows due to waves and forced axial oscillations within a mean flow. The measured force is described by the Morison Equation using $A = \frac{\pi D^2}{4}$ and $V = \frac{\pi D^2}{4} t_\mathrm{h}$, where t_h denotes the thickness of the cylinder. Nevertheless, the Morison equations described above do not always satisfy experimental data and several alternative forms exist.

Since a similarity exists between wake and thrust characteristics obtained for rotor and perforated discs of equivalent thrust operating in steady flows. As such, the findings of the Morison equation for a solid (non-perforated) cylinder in oscillatory flows may be applicable to perforated discs and rotors as well.

For a rigid cylinder oscillating in the streamwise direction in a mean flow, an alternative approach to Eq. 2.45 into Eq. 2.39 has been given by accounting for the added mass and by treating the drag due to the mean and streamwise flow component separately. This form incorporates a drag coefficient associated with the mean flow, $C_{\mathrm{D},1}$, and a different drag coefficient associated with the oscillatory flow, $C_{\mathrm{D},2}$, as follows:

$$F = \frac{1}{2}\rho A C_{\mathrm{D},1} u_0 |u_0| - \frac{1}{2}\rho A C_{\mathrm{D},2} \dot{x}|\dot{x}| - \rho V C_\mathrm{a} \ddot{x} \qquad \text{Eq. 2.48}$$

This method is based on the Verley and Moe's (1979) formula and has been shown to provide a better fit to measured time-histories of thrust on rotor and disc subjected to steady, streamwise oscillatory motions (Whelan et al., 2009b) than alternative formulations.

Another formulation of force, as proposed in here, is to account the added mass and expand the drag term (Eq. 2.39 and Eq. 2.45) into two components:

$$F = \frac{1}{2}\rho A C_{\mathrm{D},1} u_\mathrm{c} |u_\mathrm{c} - \dot{x}| - \frac{1}{2}\rho A C_{\mathrm{D},2} \dot{x}|u_\mathrm{c} - \dot{x}| - \rho V C_\mathrm{a} \ddot{x} \qquad \text{Eq. 2.49}$$

It has also been proposed that the force due to a rigid cylinder in a mean flow combined with waves (Eq. 2.43 into Eq. 2.39) may be replaced in an analogous way to Eq. 2.48, where the effects of force due to the mean and wave velocity are treated as separately (Chakrabarti, 1987). The same statement may be inferred from Eq. 2.49.

The force on the rotor may also be treated analogous to the hydrodynamic studies of representative damper and stabilizers such as squared or circular perforated thin plates.

These plates are forced to oscillate in the heave motion in a quiescent flow, whereby the measured force is then described with a linear damping, b, and added mass, a force:

$$F = -a\ddot{x} - b\dot{x} \qquad \text{Eq. 2.50}$$

In addition, some authors (Vu et al., 2004; Tao and Dray, 2008) relate the added mass of the perforated disc with the theoretical added mass for a non-perforated disc in the heave motion (oscillatory flow). This added mass resembles the water mass given by a spheroid with the origin at the mid-cross section of the disc, where the semi-axes are equal to $\mathrm{l_y} = \frac{D}{\pi}$ for the axis of motion and $\mathrm{l_x} = \mathrm{l_z} = \frac{D}{2}$ for the plane normal to the disc (Tao et al., 2007). It is (Sarpkaya and Isaacson, 1981):

$$M_\mathrm{a} = \frac{4}{3}\rho\pi \mathrm{l_x l_y l_z} = 1/3\rho D^3 \qquad \text{Eq. 2.51}$$

Therefore, the non-dimensional added mass (C_a) and damping (C_b) obtained using this normalisation of mass into Eq. 2.50 are simply expressed as:

$$C_\mathrm{a} = \frac{a}{M_\mathrm{a}} = \frac{a}{1/3\rho D^3} \qquad C_\mathrm{b} = \frac{b}{2M_\mathrm{a}\omega} = \frac{b}{2/3\omega\rho D^3} \qquad \text{Eq. 2.52}$$

Since the area and added mass of a porous disc in the Morison equation could replace that obtained for a rotor, the added mass on the porous disc and rotor is given here as a multiple of the mass of this spheroid.

This set of force equations will be explored in the following chapters to evaluate its suitability with the measured force on a porous disc and a rotor in oscillatory flows due to waves and forced streamwise motions.

2.13 Extreme-Value Analysis

The capital cost of a support structure (Lee, 2005; Blasques and Natarajan, 2013) and reliability of a wind turbine are a function of the service and maximum loads expected during the design life and of the load cycles expected during operation (Det Norske Veritas, 2007; IEC61400-3, 2009). The time-varying response required for a wind blade test design is often of the order of more than half billion successive repeated cycles (Freebury and Musial, 2000). The process incurred in conducting such analysis experimentally is laborious, time consuming and costly. Various numerical and statistical tools have been developed to represent the long-term physical behaviour of wind loading in typical operating flows using a limited set of data. The time history of rotor forces, obtained either from measurements or time-dependent simulations, are then extrapolated to exceed probabilistic loads and converted to equivalent loads for the life support assessment and fatigue blade damage (Moriarty et al., 2004).

Although fatigue and blade failure analysis methods developed for wind turbine applications have been applied to tidal stream turbines (McCann, 2007; Val et al., 2014), little work has been done on the ultimate loads caused by the combination of turbulent flow and waves that exist at tidal stream sites (Fernandez-Rodriguez et al., 2013). Appropriate experiments or modelling are required to obtain the excitation rotor force in wave flows and hence quantify the extreme forces applied to tidal turbine supporting structures.

Due to the nature of turbulence and waves, the loads on offshore support structures could be considered as random variations, characterised by a statistical process, combined with a quasi-steady process. The aim of such statistical models is to draw conclusive evidence from the natural phenomenon and represent properly the effects of the underlying process.

Extreme-value analysis methods are typically used to identify the peak occurrences within time-history of measurements and predict the values most likely to arise within a time interval that is longer than the duration of the original sample. A 25, 50 or 100 year return period is often defined as a design survivability requirement for an oil and gas offshore support (Sirnivas et al., 2014). In the case of an offshore wind turbine, design standards require consideration of return periods of 1 and 50 years (IEC61400-3, 2009).

Extreme-value analysis methods are not limited to particular phenomenon and have been applied to many physical and environmental research areas. Examples include the forecast of maximum sea levels and floods likely to occur in storms (Coles et al., 2001), the forces generated on oil and gas offshore structures by ocean waves (Brouwers and Verbeek, 1983; Naess, 1983), the predictions of maximum wind loads (Simiu et al., 2001) and the response of tension leg platforms supporting wind turbines (Jensen et al., 2011), amongst others.

In Sarpkaya and Isaacson (1981) five probability distributions, including the Type 1, are discussed for the prediction of extreme wave heights during a random sea described by narrow-band spectra. For each method, exceedance statistics are obtained for the maximum wave height of each independent event defined by a threshold force. A fitting technique is subsequently employed at the low probability curve to extrapolate from the trend of exceedance statistics to specific exceedance, or probability, values.

The ability to trend-fit and the effectiveness of an extreme method depends on the residual (R^2_{res}) obtained between the measured events in the tail of the probability distribution and the fitted trend-line. The threshold and sample length must be carefully selected to ensure that convergence is produced with the extreme values obtained using a very large sample.

Various and more complicated methods are also available for extrapolating independent data to a low probability range by rescaling the events and probability such that a linear trend is obtained. These specific methods are often used for extreme analysis studies, such as characterising the maximum loading on offshore wind turbines.

The extreme loading on a wind turbine is typically predicted to be proportional to the squared velocity of the flow component across the rotor that is expected during the operating life (Simiu et al., 2001). In order to identify the long-term wind conditions at a deployment site, several statistical methods have been developed and compared to measurements. These include the Generalized Pareto (Brabson and Palutikof, 2000), Weibull (Perrin et al., 2006), combined Normal-Weibull (Kollu et al., 2012), Rayleigh and lognormal distribution (Morgan et al., 2011), amongst others. The suitability of each method has been shown to vary according to the site. For tidal flows, the extreme prediction of the squared velocity has been considered using a Generalized distribution (Harding et al., 2011), Normal and Gumbel distributions (Val et al., 2014). Nevertheless, the implementation and accuracy of employing a particular statistical method for a tidal stream is less well known than for a wind resource and thus the tidal flow characterisation is still in progress (Togneri et al., 2011; Milne et al., 2013). In this work, three of these statistical distributions are considered further and a summary of the Generalized Pareto with the Type 1 distribution, the Normal and the Weibull method is given (see Embrechts et al., 1997; Schabenberger and Pierce, 2001; Papoulis and Pillai, 2002; Hsu, 1996).

The Generalized Pareto distribution (GP) is usually employed for modelling theoretical and observable tails of exceedance curves with complicated forms. The GP distribution is fitted by different curves depending on the distribution shape of the curve, k_s, the scale or standard deviation, σ, and location of the mean, μ_0. The GP cumulative function for a random force, F_j, is mathematically stated as:

$$\mathcal{F}_{\text{Pareto}}(k_{\text{s}},\sigma,F_{\text{j}},\mu_0) = \begin{cases} 1-\left(1+\dfrac{k_{\text{s}}(F_{\text{j}}-\mu_0)}{\sigma}\right)^{-\frac{1}{k_{\text{s}}}}, & k_{\text{s}}\neq 0, \sigma>0, \mu_0\in\mathbb{R}, k_{\text{s}}\in\mathbb{R} \\ 1-e^{-\frac{(F_{\text{j}}-\mu_0)}{\sigma}}, & k_{\text{s}}=0, \sigma>0, \mu_0\in\mathbb{R}, k_{\text{s}}\in\mathbb{R} \end{cases} \quad \text{Eq. 2.53}$$

where the domain of the function corresponds

$$\begin{aligned} &\mu_0 \leq F_{\text{j}} < \infty\,, && |\, k_{\text{s}} \geq 0 \\ &\mu_0 \leq F_{\text{j}} < \mu_0 - \tfrac{\sigma}{k_{\text{s}}}\,, && |\, k_{\text{s}} < 0 \end{aligned} \quad \text{Eq. 2.54}$$

Three GP cumulative shapes are commonly identified. The GP with positive shape values provide cumulative functions with tails that can be approximated using polynomial equations. A shape parameter of zero value depicts tails given by exponential functions (see Eq. 2.53) and negative magnitudes generate curves with finite tails. Finite tails correspond to cumulative functions that are defined in the probability interval [0-1] and contain curves described by using three-shape parameters $(k_{\text{s}},\sigma,\mu_0)$. Here, the measured distribution is approximated at the tail of the probability distribution using the Generalized Pareto distribution (Eq. 2.53 and Eq. 2.54) and subsequently, measurements and predictions are then scaled by the Type 1 extreme distribution.

A Type 1 extreme distribution, also referred as the Gumbell distribution, is often employed to model measurements with probability functions of the following form (Schabenberger and Pierce, 2001):

$$\mathcal{F}_{\text{Type 1}}(k_{\text{s}},F_{\text{j}},\mu_0) = \exp\left(-\exp\frac{-(F_{\text{j}}-\mu_0)}{k_{\text{s}}}\right) \quad \text{Eq. 2.55}$$

where the measured force is F_{j}, and the mean and shape of the distribution correspond to μ_0 and k_{s}. Eq. 2.55 can be rewritten by converting the exponential expression into natural logarithmic forms. This format provides a linear relationship of the cumulative probability distribution. It is:

$$-\ln(-\ln\{\mathcal{F}(k_{\text{s}},F_{\text{j}},\mu_0)\}) = \frac{1}{k_{\text{s}}}F_{\text{j}} - \frac{\mu_0}{k_{\text{s}}} \quad \text{Eq. 2.56}$$

where $\frac{1}{k_{\text{s}}}$ and $\frac{-\mu_0}{k_{\text{s}}}$ denote the slope and intercept of the linear equation. For this method, extreme values are obtained by extrapolating the measured data to specific exceedance values. Thus, if the measured and fitted tail of the distribution using the Pareto method are in good agreement, then both distributions scaled in the Type 1 format trend into a straight line.

Weibull distributions, besides providing good agreement with wind speed distribution, are also employed to approximate probability of occurrence of wave heights within seas of narrow-band spectra. The Weibull cumulative function is:

$$\mathcal{F}_{\mathrm{weibull}}\left(k_{\mathrm{s}}, F_{\mathrm{j}}, \lambda_{\mathrm{s}}\right) = \begin{cases} 1\ e^{-\left(\frac{F_{\mathrm{j}}}{\lambda_{\mathrm{s}}}\right)^{k_{\mathrm{s}}}} & F_{\mathrm{j}} \geq 0, k_{\mathrm{s}} > 0, \lambda_{\mathrm{s}} > 0 \\ 0 & F_{\mathrm{j}} < 0\ , k_{\mathrm{s}} > 0, \lambda_{\mathrm{s}} > 0 \end{cases} \qquad \text{Eq. 2.57}$$

where k_s is the shape and λ_s the scale parameter of the distribution. The Weibull exceedance can be linearly arranged by rewriting Eq. 2.57 as a log-log format. After a series of algebraic manipulations, the cumulative function converts to:

$$\ln\left(-\ln\left(1n\mathcal{F}_{\mathrm{weibull}}\left(F_{\mathrm{j}}\right)\right)\right) = k_{\mathrm{s}}\ln\left(F_{\mathrm{j}}\right) - k_{\mathrm{s}}\ln\lambda_{\mathrm{s}} \qquad \text{Eq. 2.58}$$

Eq. 2.58 is similar to the slope form formula of a straight fitted line to the experimental data ($y = m_{\mathrm{slope}}x + b_{\mathrm{ord}}$). Thus, if the measurements follow the theoretical distribution, the scaled cumulative curve becomes linear and the extremes are obtained by extrapolation.

The normal distribution describes symmetrical exceedance curves centred on the mean with negligible skewedness. Its shape is defined by the mean, μ_0, and standard deviation, σ, of the measured data. The cumulative Normal function is:

$$\mathcal{F}_{\mathrm{normal}}\left(\sigma, F_{\mathrm{j}}, \mu_0\right) = \frac{1}{\sigma\sqrt{2\pi}} - \int_0^{F_{\mathrm{j}}} \frac{1}{t} e^{\frac{-(\mathrm{t}-\mu_0)^2}{2\sigma^2}} dt \quad \sigma^2 > 0, \mu \in \mathbb{R} \qquad \text{Eq. 2.59}$$

A special case is the standard normal distribution, where μ_0 =0 and σ =1, and the x-axis of the cumulative function is scaled to units of standard deviations.

In summary, it is plausible to conclude that measurements originated from a theoretical distribution, when the measurements are scaled to the theoretical probability plot and this trend follows a straight line. The Generalized Pareto is perhaps the most convenient approach for representing the form of an exceedance distribution tail. However, the sensitivity of threshold magnitude with the length of the measurements needs to be checked and compared to other methods.

2.14 Conclusions

The literature review on environmental conditions at tidal stream sites provided representative ranges of turbulence intensities, wave flow periods and amplitudes. Different modelling techniques typically employed for both wind and tidal turbine design in uniform and sheared flows were also discussed. A numerical BEM code was outlined to predict the power curve of a generic rotor in steady flows. Modifications to account for high axial induction, tip losses and blockage have been identified. A blockage correction method for steady flow based on a tunnel model was identified.

Studies were reviewed concerning the causes of oscillatory flows and loading including due to rotor motion and wave-induced components to mean flow. These flow conditions transmit similar unsteady characteristics to the rotor performance in the form of high turbulence frequency components and wave oscillations, typically at a much lower frequency. Subsequently, applications of statistical methods based on extreme prediction were addressed for the design life of a support and wind turbine. This approach consisted in obtaining the peak forces exceeded by a threshold magnitude. Three theoretical distributions to extrapolate measurements to exceedance probability forces were defined to investigate variation of extreme values and suitability of extreme value analysis method.

CHAPTER 3: LOADING OF A TIDAL STREAM TURBINE IN TURBULENT CHANNEL FLOW

A BEM solver has been developed to investigate variation of thrust and power coefficient with rotational speed (Tip-Speed Ratio, TSR). The objective is to first quantify the rotor loads accounting for incident steady flows and then to assess in the next chapters the influence of oscillatory flow due to waves and structural motion. To evaluate the accuracy of the model, predictions of thrust and power are first compared to published performance of two tidal stream rotors of 0.4 m diameter each (Bahaj, Batten et al., 2007; Galloway et al., 2011).

The numerical model is then compared to the predicted thrust performance of a full-scale turbine (Whelan and Stallard, 2011) and to experimental measurements of a scaled rotor. The scaled rotor employed represents the thrust curve of a full-scale turbine that operates at a different Reynolds number. This process required the use of different blade geometry depending on the Reynolds number. Two rotors were designed to represent a full-scale turbine located in water depth of 33 m at approximately 1:30th scale and 1:70th scale based on channel depth. All rotors comprised three blades. The predictions of thrust and power for the full size rotor are as reported in Whelan and Stallard (2011) using the GH Tidal Bladed software. For the 1:70th scale rotor, the performance predictions were obtained using the in-house BEM code. These predictions were then compared to predictions of the full scale rotor and to experiments based on channel-flow velocity at 1:70th scale.

Thrust values with a specified exceedance probability are then determined for flows with onset turbulence intensity (TI) of 12% and 14%. The technique employed is based on methods typically applied to extreme wave statistics. In the thesis, the same approach will be applied to predictions of the loading on a full-scale rotor supported on a flexible or floating structure to assess whether dynamic response of the structure can be employed to reduce the magnitude of extreme loads.

3.1 BEM Model Predictions

In Bahaj, Batten, et al. (2007), the performance characteristics of a 3-bladed rotor were evaluated against the rotor's rotational speed variation at four blade-pitch angles: $\gamma = 0^{\circ}$, 5°, 10°, 12°. The geometry of the rotor was described, along with a methodology based on BEMT for the prediction of the power curve. The sections of the blade were selected with NACA 68XX profiles with drag and lift relationships obtained via the panel method XFOIL and stall extrapolation techniques developed by Viterna and Corrigan (1982). Simulations based on the BEMT were contrasted with performance measurements in steady flows.

The accuracy of the BEM solver, as shown in Chapter 2, was then evaluated using the published drag and lift relationships of the rotor blades (Batten et al., 2007). The power curves obtained for the blade-pitch angles $\gamma = 5^{\circ}$, 10°, 12°, were compared to the published performance and these were found to be in agreement within 11%.

For the TSR range 6 to 10 and blade-pitch angles γ<5°, the axial induction factor was not predicted within the range of validity of the Linear Momentum Theory and hence prediction of curves varied with use of high axial induction and tip-loss factors (Leishman, 2006). In Figure 3.1, the variation of the predicted curves for the 5° blade-pitch condition is shown against the measurements. It is seen that the curves for the power coefficient were in close agreement with results but thrust coefficients were under-predicted by approximately 10%. The corrected thrust using the Spera method provided the lowest least-squares fit residuals between the model and measurements.

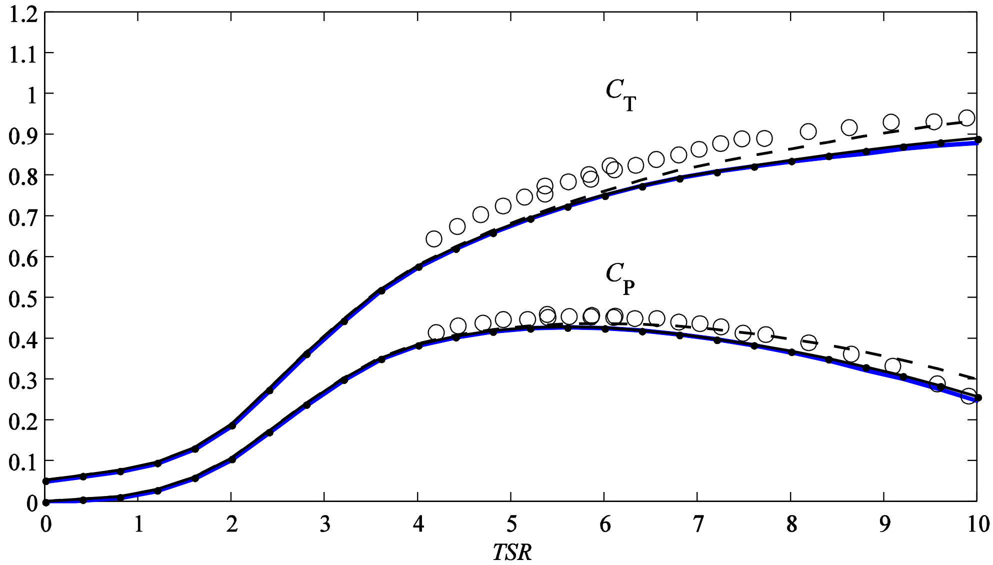

Figure 3.1 Thrust and power predictions compared to published measurements (○) for a pitch angle of $\gamma = 5^{\circ}$ (Bahaj, Batten, et al., 2007). — Buhl; --, Spera; ●-, Tidal Bladed high axial induction factors.

The BEM capability was also validated against current tests of a 3-bladed single rotor as described in Galloway et al. (2011). The blade sections of this rotor utilised NACA 48XX profiles. Lift and drag were provided by Galloway (2013) for different thickness over chord parameters and these were utilised as input data to the BEM model.

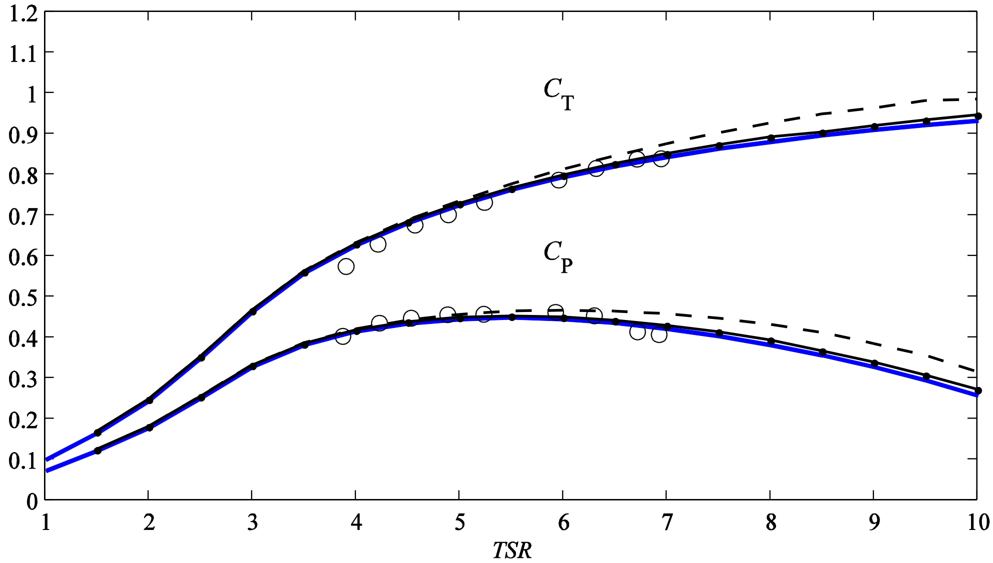

Figure 3.2 Thrust and power predictions compared to published measurements (○) of a 0.4 m diameter rotor (Galloway, 2013). Line types as Figure 3.1.

BEM predictions were in agreement with published values of mean thrust and power (Figure 3.2). Influence of high axial induced flow was obtained near the tip and for TSR greater than 6. Across this high axial factor range, the Tidal Bladed and Buhl thrust method were in better agreement than the Spera Method.

Simulations for a single 1:70th scale rotor with blade length of 0.135 m and maximum chord length of 0.03 m were finally contrasted to the predictions of GH Tidal Bladed. The Reynolds number (Re) operated based on this blade chord was approximately 30x10^3 for which a Goettingen 804 foil section was selected with radial variation of chord length and twist. For this Re, the blade's drag and lift relationships were provided by Hassan (1982) and these were employed as an input to the model.

The majority of the radial variation of axial induction factors across the operational TSR range 0 to 7 was found within the valid range of the Momentum Theory. Therefore, the use of two different tip loss factors and formulas each for high axial induction factors yielded fairly consistent power and thrust coefficient curves (Figure

3.3). Both thrust coefficient curves were close to the published data range. However, the use of the most appropriate high axial induced flow correction remains uncertain and must be verified against experiments.

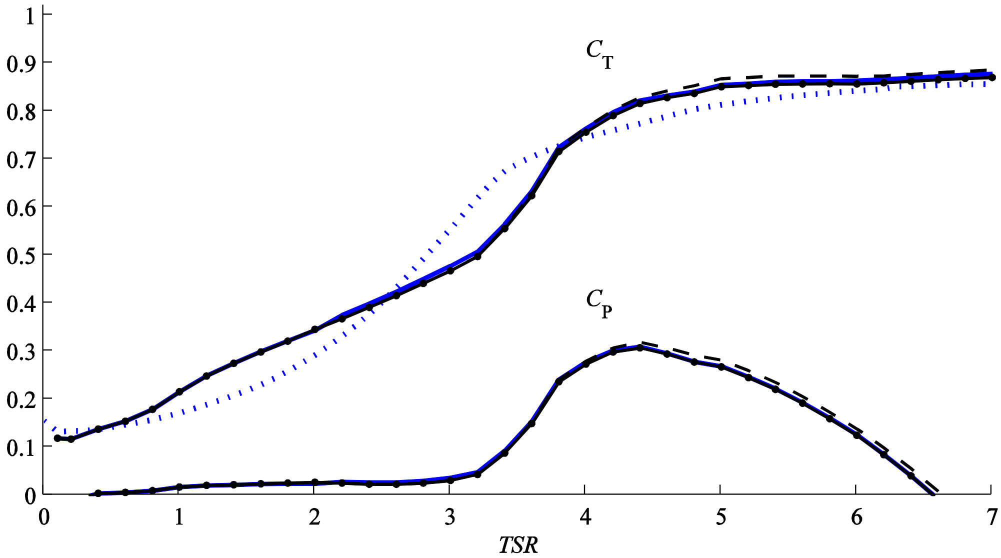

Figure 3.3 Power curve predictions for a single rotor using set of lift and drag coefficients obtained for Re=30000 against the published thrust coefficient's curve (--) (Whelan and Stallard, 2011). Predictions employing Buhl (—), Spera (--) and Tidal Bladed (●-) corrected high axial induction factors.

3.2 Mean Thrust and Power in Turbulent Channel Flow

To evaluate influence of flow's turbulent intensity on the rotor's power and loading, experiments were conducted in two representative tidal characteristics of the turbulent flows in a channel of width W =5 m and still-water depth h =0.45 m. This represents a channel of approx. 31 m deep at 1:70th geometric scale. The flow was developed by pumps located between outflow basin and inflow basin. Flow velocities, u_x, u_y, u_z, were measured using a Nortek Vectrino+ ADV sampling at 200 Hz. The flat bed of the channel was 12 m long and the turbine was located 6 m from the inflow. A porous plate was located over the inflow plane to produce a uniform level of inflow turbulence. This arrangement produced a depth-averaged velocity U_0 =0.46 m/s and turbulence intensity, $\frac{u'_{\mathrm{rms}}}{U_0}$, 12% at the rotor. For one test, a rough bed consisting of a series of pallets with height 0.1h was installed across the central 3 m of the channel width and entire length.

This arrangement produced a sheared velocity profile with depth-averaged velocity U_0 =0.46 m/s and turbulence intensity 14% at the rotor (Figure 3.4). The turbulent field at the inflow plane was characterised using Taylor's hypothesis of frozen turbulence. According to this hypothesis, turbulence is translated longitudinally by the mean flow velocity with the statistical properties of the perturbations remaining undisturbed, as they are shifted along the flow. If velocity measurements are extracted from a single fixed point, the time integral of its autocross-correlation then provides the time lag of the spatial separation between two synchronised perturbations. The time integral multiplied by the mean speed, then gives the spatial length characteristic of the flow, known as the turbulent length scale, which in turn characterises the average size of the largest eddies. The turbulent length scales and the magnitude of the turbulent intensity, have been found to contribute changes on the wake generated by a rotor and an equivalent disc (Blackmore et al., 2014). Furthermore, increased values of turbulent intensity have been found to increase the fluctuations of thrust (Mycek et al., 2014) and the root bending moments of the blade sections (McCann, 2007). The channel flow characteristics are therefore relevant for the design of the blades and for the study of single device loading and performance of array of rotors (Myers et al, 2013).

To obtain the average length scale, L_{ii}, the time integral of the temporal correlation factor was calculated with the hub-height velocity, $C_{\mathrm{i}}(\tau_{\mathrm{t}})$, and then multiplied with the depth-averaged velocity. They are:

$$C_{\mathrm{i}}(\tau_{\mathrm{t}}) = \frac{\langle u'(t)\, u'(t+\tau_{\mathrm{t}})\rangle}{\langle u'(t)^2\rangle} \qquad i = x, y, z \qquad \text{Eq. 3.1}$$

$$L_{\mathrm{ii}} = U_0 \int_0^{\infty} C_{\mathrm{i}}(\tau_{\mathrm{t}}) d\tau_{\mathrm{t}} \qquad \text{Eq. 3.2}$$

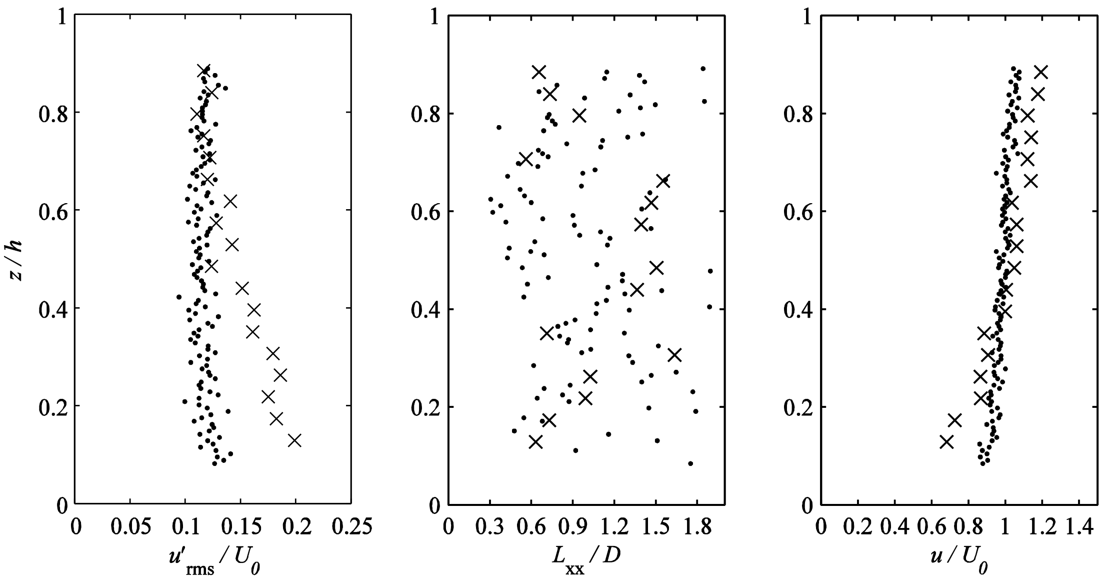

Figure 3.4 Characteristics of the turbulent currents in the streamwise direction for a porous plate at the inflow plane (●) and a rough bed across the channel bed (X) from 1-minute measurements. Source modified from Olczak et al. (2013).

The average length scale over the rotor depth from a 10 minute sample in the streamwise direction was approximately 0.6 and 0.9 times the water depth for the current flow with TI =12% and TI =14%. The energy spectrum of the hub-height velocity in the two ambient conditions exhibited a significant contribution of the turbulent fluctuations in the frequencies of 0.05-0.445 Hz (Figure 3.5). However, the frozen turbulence concept gives a time scale $\frac{0.26}{0.46}\sim 0.6$s (corresponding to a characteristic frequency of $\sim 1.7\ Hz$), which suggest that the frozen turbulence is not applicable in such constrained flows with very large length scales between the vertical and horizontal dimensions. The rotor axis was supported on a 15 mm outer diameter tower with centreline $0.4D$ downstream of the rotor. The support structure was rigidly attached to a gantry spanning the flume. The time-varying force on the rotor was measured by a strain gauge located at 0.8 m above the rotor axis by assuming that the bending moment was due to the force acting at the hub centre. The axial force on the rotor $F_x(t)$, was defined as the measured force minus the force on the immersed tower due to steady flow only. The tower load contributed around 8% of the mean thrust. The force range was 0 to 10 N. The tower stiffness was determined to be 1.47 N/mm with a natural frequency of around 11 Hz and so support was considered effectively rigid. Angular speed of the rotor was obtained by differentiation of angular position measured by an optical encoder providing a resolution of $\pi/100$. Mechanical torque applied to the rotor was the sum of mechanical friction and the torque developed by a 24 Volts electrical motor. Prior to each test, the motor torque was required to maintain constant angular speed of the axis to overcome the mechanical friction. During each test, constant torque was applied by specification of the motor torque. The angular position and force were sampled at 200 Hz.

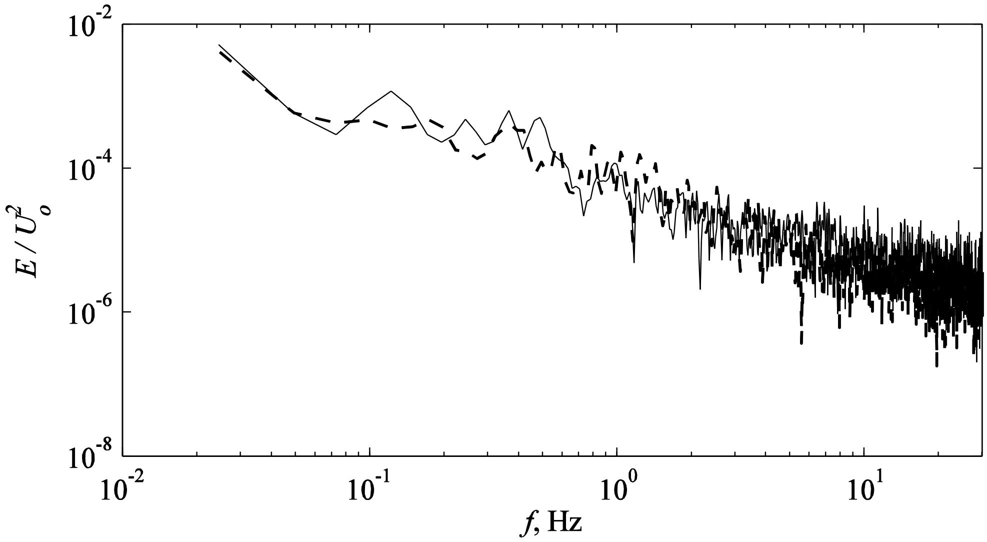

Figure 3.5 Spectrum of the operating flow with an average TI =12% (-) and TI =14% (--) obtained at the hub height from a single minute measurement.

The average speed, thrust and power of the rotor was obtained over a 60 s record interval. A comparison was drawn between the measurements in the current flow of TI =12% and the predicted power curves. Mean values of both thrust and power were found in reasonable agreement over the studied range of TSRs with a 10% difference (Figure 3.6). The empirical thrust based on Tidal Bladed formula was found to be the most appropriate to represent measurements of the rotor flow conditions.

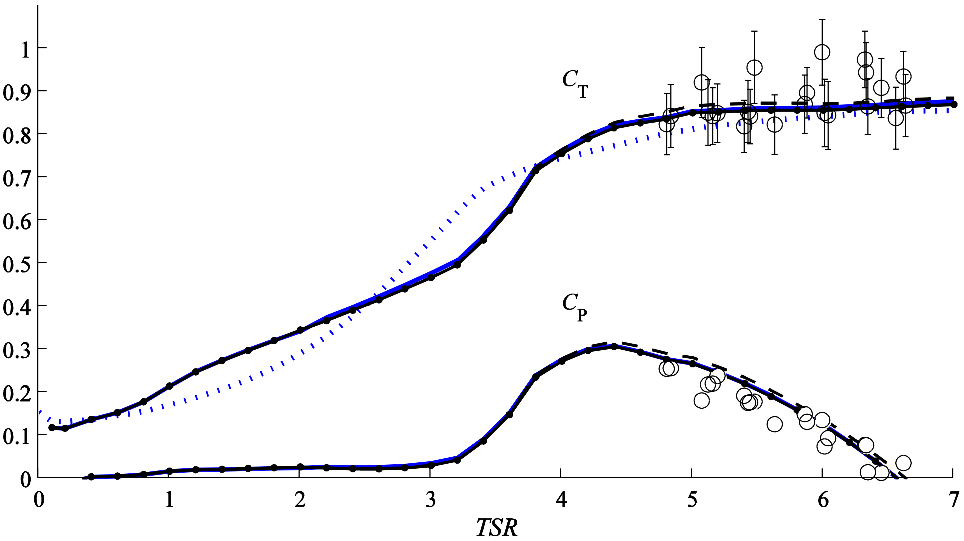

Figure 3.6 Numerical model compared to the predicted thrust coefficient's curve (Whelan and Stallard, 2011) and 1-minute average measurements (○) with their corresponding error bars. Line types as Figure 3.3.

The standard deviation of the force coefficient, $C_T{'}_{\text{rms}} = \frac{F'_{\text{rms}}}{1/2\rho A u_0{}^2}$, across the TSR range of 4.5 to 6.5 was 0.118-0.17. This as well produced a fluctuating ratio of $\frac{C_T{'}_{\text{rms}}}{u'^2_{\text{rms}}} = 2.4 - 3.3\ \frac{s^2}{m^2}$. The effect of blockage on the performance of the rotor was addressed with the methodology of the tunnel correction described in Bahaj, Molland, et al. (2007). The blockage ratio from laboratory scale using Eq. A.6 for the single rotor was:

$$\varepsilon = \frac{A}{A_0} = \frac{\pi R^2}{\mathrm{W}h} = \frac{\pi 0.135^2}{5(.45)} = 0.025447$$

.

The incident velocity (u_0), torque (Q) and thrust (T) were obtained as averages over a 60 seconds record. The disc, bypass, wake, and equivalent velocity were calculated using Eq. A.16, Eq. A.20, Eq. A.21 and Eq. A.25 respectively. The equivalent water velocity in unbounded flow using this approach was found to exceed the measured bounded flow by 0-1%. Measurements were corrected with the equivalent open channel velocity and a comparison was drawn against the unbounded BEM simulations (Figure 3.7).

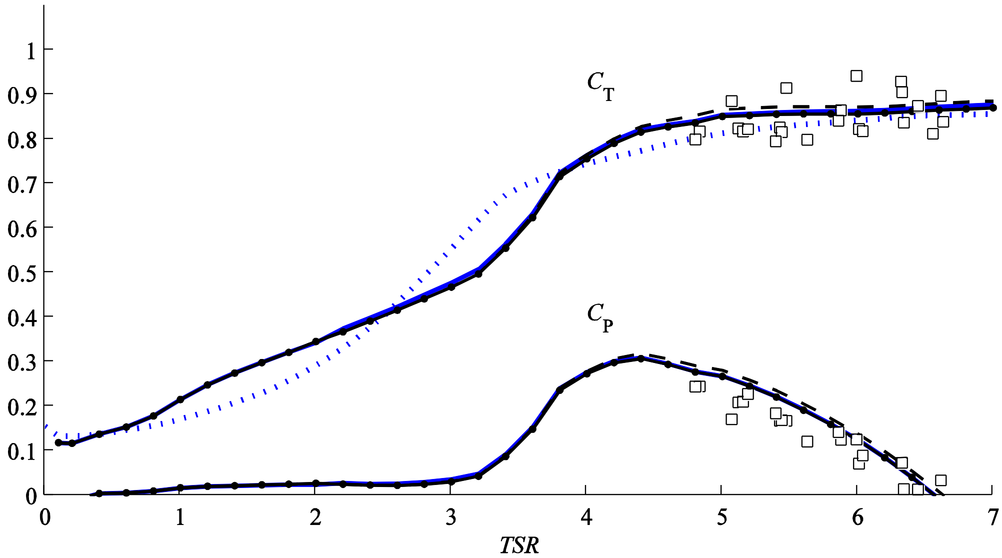

Figure 3.7 BEM predictions against published predictions (Whelan and Stallard, 2011) without blockage and average of 1-minute thrust sample with blockage correction (□). Line types as Figure 3.3.

The blockage effects were found to increase the experimental thrust coefficients by around 2-3% and to decrease both power coefficients by 2-4.5% and Tip-Speed Ratio by 0.5-1.5 %. This represented a small discrepancy in the rotor performance and so blockage effects could be ignored. The unbounded BEM predictions and corrected average thrust and power over a 60 s interval were found to be in reasonable agreement.

3.3 Variance of Rotor Thrust

Porous discs are often used for wake generation in Momentum Theory and as analogy for rotors in experimental studies of tidal turbines, particular at small geometric scale. The same analogy may also provide some insight into unsteady loading of a turbine. The force fluctuations experienced by a solid, square plate in turbulent winds was expressed by Bearman (1971) in proportion to the flow's turbulence characteristics, $\frac{fD}{u_0}$, the mean force and the aerodynamic admittance, $\chi^2|f|$, which defines the ratio of intensity fluctuations between force and incident velocity at given frequency (Jancauskas and Melbourne, 1983). The rms of the force is $F'_{\mathrm{rms}} = 2\,F_0\,\chi|f|\,\frac{u'_{\mathrm{rms}}}{u_0}$. The theoretical framework was based on the lattice plates work of Vickery (1965) and relates the diameter of the plate,

D, the turbulent intensity and peak frequency of the force spectrum with the spatial length scales of the turbulent flow, L_{xx}/D. The flat plate model provides different curves of admittance values for the turbulent conditions with length scales values of L_{xx}/D >0.375 against frequency parameters of $\frac{fD}{u_0}$ =10^{-3} to 10. The curves of the aerodynamic admittance for large length scales L_{xx}/D > 1.5 do not vary significantly and thus they approach an admittance curve predicted with $L_{\mathrm{xx}}/D = \infty$. The theory of aerodynamic admittance may be considered analogous to the rotor horizontal load and was used to predict the fluctuations experienced in turbulent channel flows at TSR=5.5.

For this Tip-Speed Ratio, the mean thrust in the turbulent channel flows was F_0 =5.5 N, with most of flow fluctuations energy located in the frequency range 0.1-0.445Hz. Hence, the frequency parameter was $\frac{fD}{u_0}$ =0.06-0.26. For the current flow of TI =12%, the measured standard force deviation normalised to the mean, F'_{rms}/F_0, was obtained as 0.14 with an average length scale L_{xx}/D ≅1. The theory of the aerodynamic admittance predicts for L_{xx}/D ≅1 an admittance of $\chi^2|f|$ ≅ 0.46-0.84 and corresponding fluctuation of F'_{rms}/F_0 = 16.2 – 22%. For the flow with TI =14%, the measured shear force fluctuation was $\frac{F'_{\mathrm{rms}}}{F_0}$ = 0.21 with a length scale parameter L_{xx}/D ≅1.5. For this case, an admittance corresponds to $\chi^2|f|$ ≅ 0.48-0.66 with a force ratio of $\frac{F'_{\mathrm{rms}}}{F_0}$ = 19-23%. These estimates were considered close to the results and transferable to the rotor thrust.

Discrepancy resulted from use of the rotor instead of the square plate and difference of the turbulence nature between open channels and grid lattice plates. The nature of channel turbulence is quite different from grid turbulence, with large horizontal length scales and vertical scales typical of unbounded turbulent boundary layers. The more coherent two-dimensional nature possibly explains the greater magnitudes of fluctuating force in low turbulent channel flow. The closer agreement at the increased turbulent channel flow, L_{xx}/D ≅1.5, is due to convergence of the aerodynamic admittance curves.

The turbulent intensity of the incident flow was also related to the standard deviation of the turbulent thrust with a multiplier factor, $K_{\mathrm{I}} = \left(\frac{F'_{\mathrm{rms}}/F_0}{u'_{\mathrm{rms}}/U_0}\right)$. The magnitude in the current flow with TI =12% and TI =14% was 1.16 and 1.5.

3.4 Peak Thrust in Turbulent Channel Flow Only

The objective of this section is to characterise the support structure loading that corresponds to a specified probability of exceedance. Turbulent flows generate load fluctuations on the rotor and hence affect fatigue and life of the support structure, as well as rotor performance, device reliability and total costs. It is intended that by developing techniques for prediction of the most commonly occurring forces relative to the turbulent intensity of the ambient flows, the design criteria for blade and support life span are both identified according to the operating site characteristics and this will enable design for long-term survivability. The method employed follows the approach of Sarpkaya and Isaacson (1981) for the prediction of wave height elevations (see review of Section 2.13). The forces exceeded by 1/100 (1%), 1/1000 (0.1%) and 1/10000 (0.01%) samples were considered using the peak-over-threshold technique. The basis of this approach is to identify the maximum forces, F_{j}, from independent events n_{exc} =1 to N over the measured interval divided by the wave period $0 < t < M$. Each event is defined as an interval during which the force, F_{x}, exceeds a threshold multiple of the mean force, F_{Th} (Figure 3.9a). The probability of exceedance of the given force is then $\mathrm{P}\,(F > F_{\mathrm{j}}) = n_{\mathrm{exc}}(F > F_{\mathrm{j}})/N$, the mean period between each event is $T_{\mathrm{p}} = M/(N+1)$ and the return period as $T_{\mathrm{R}} = T_{\mathrm{p}}/(1-\mathrm{P})$. The histogram of the forces greater than the unit threshold force ($F > F_{\mathrm{Th}}$) and the probability curve of independent events for a single minute measurement of rotor response in mean flow with TI=12% is shown in Figure 3.8. From recordings, there are approximately 0.84 independent events per second and therefore the mean period between each event (peak force) is T_{p} =1.18s.

The upper tail of the cumulative function of independent events for the range 0.4< $\mathrm{P}\big(F < F_{\mathrm{j}}\big)$<0.99 was approximated with a MATLAB function employing the GP distribution and best-fitted parameters. The Pareto tail was then applied to the Type-1 distribution to extrapolate from the measured data to forces with low probability of occurrence (Figure 3.8b).

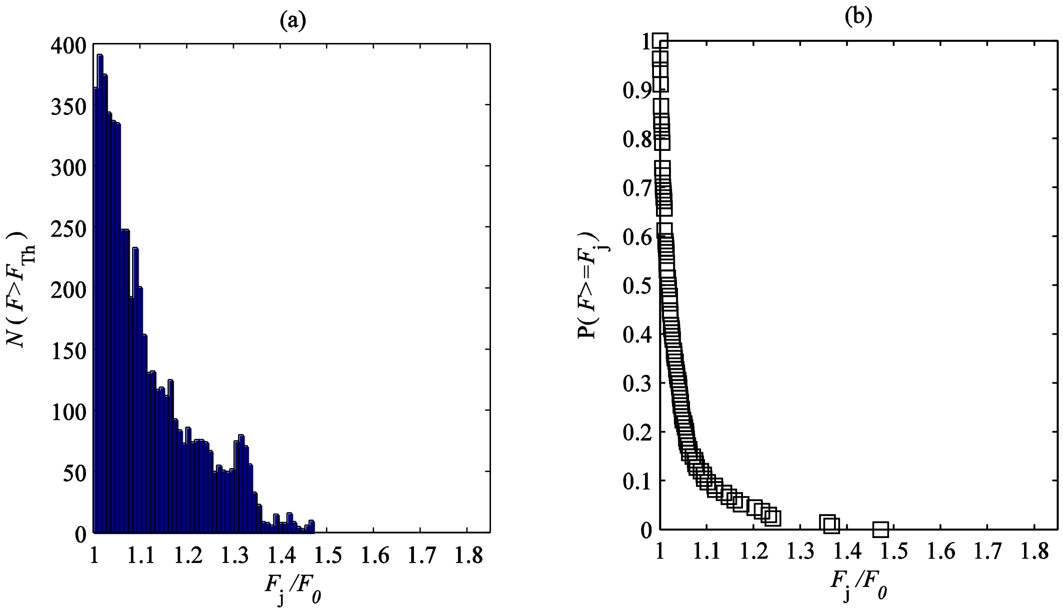

Figure 3.8 Statistical analysis of the measured and exceeded rotor forces. a) Histogram of the forces greater than threshold force of 1 due to turbulent channel flow for a single minute measurement. b) The probability of exceedance for the maximum forces obtained at each independent event.

The exceedance force calculated by this approach showed some sensitivity to the sample duration, the threshold force and the extreme-value method employed. Employing a Type 1 Extreme-Value distribution for a single minute measurement, the 1% force was determined as 1.34, 1.37 and 1.36 for threshold forces of 1.1, 1.2 and 1.3 times the mean force (Figure 3.9b).

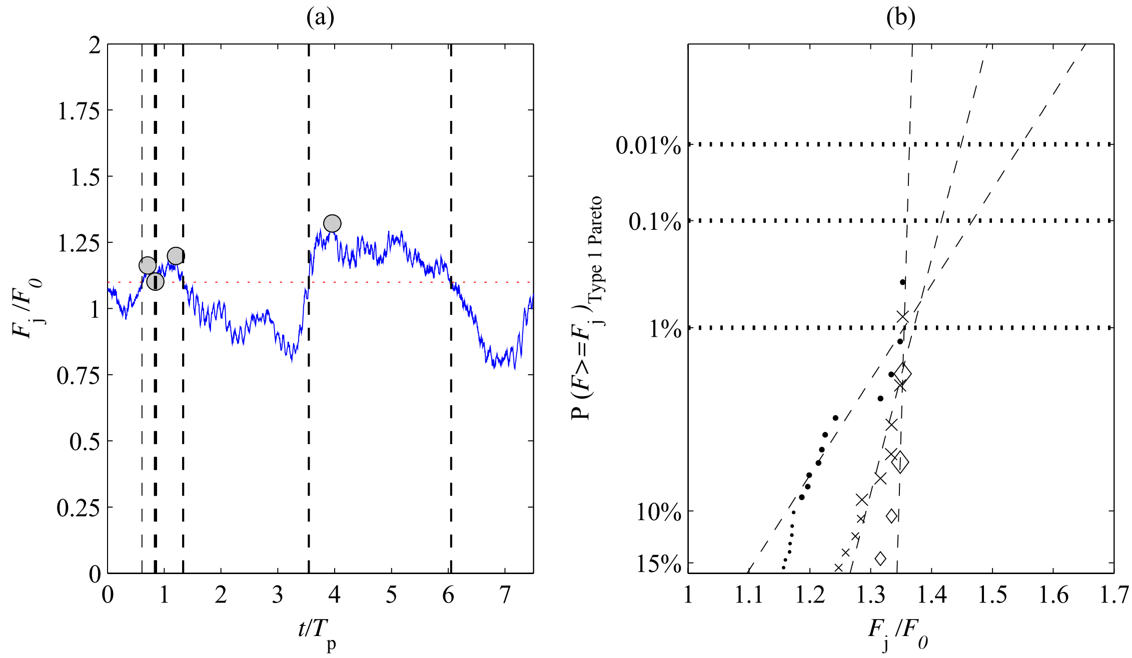

Figure 3.9 Statistical analysis of the exceedance rotor forces in a mean flow with $TI = 12\%$. a) Time-varying force normalised to the frequency of the velocity fluctuations $\frac{1}{T_p}$ =0.85 Hz, depicting successive exceedance intervals (| |) and maximum forces (●) (independent events) during each interval. b) Type-1 probability distribution of rotor forces with threshold forces of 1.1 (●), 1.2 (X), and 1.3 (◊) times the mean force.

In the probability plot for the three parameters, the threshold curve of 1.3 had the steepest slope and greater extreme variation since the fitting was carried out over a smaller set of independent events. Setting a high threshold force results in fewer independent events, a steeper probability slope, longer return period and a less convergent extreme value compared to that obtained using the long run measurements. Based on analysis of samples of between 1 and 30 minutes duration and threshold forces of 1.1 to 1.3, a sample duration of 7 minutes and threshold force of 1.1 was employed such that the 1% force obtained is within 3% (Figure 3.10). Applying Froude scaling to the 1:70$^{\text{th}}$ scale experiments, the 1% exceedance force represents a force with a return period, T_R, of approximately half an hour at full scale during a steady turbulent flow of 3.76 m/s.

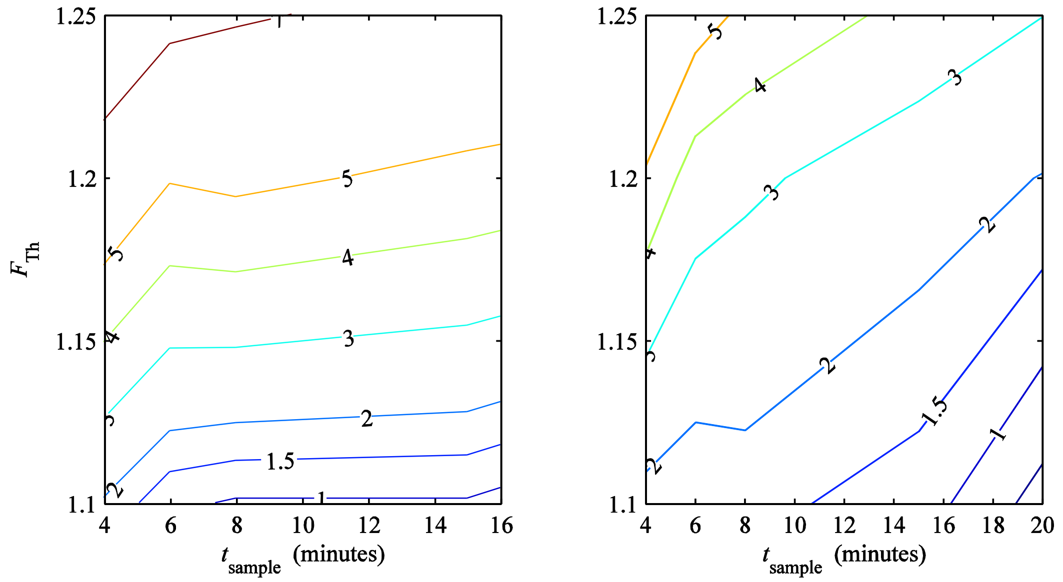

Figure 3.10 Percentage difference of the 1% (left) and 0.1% (right) loads obtained with different threshold forces and sample lengths based on the continuous 30 minutes of data.

The 1% load in the current flow with a *TI* of 12% was around 38% greater than the mean. The turbulence intensity of the flow had a negligible effect on the mean thrust but increased to a greater extent the fluctuations and hence the peak loads (Figure 3.11).

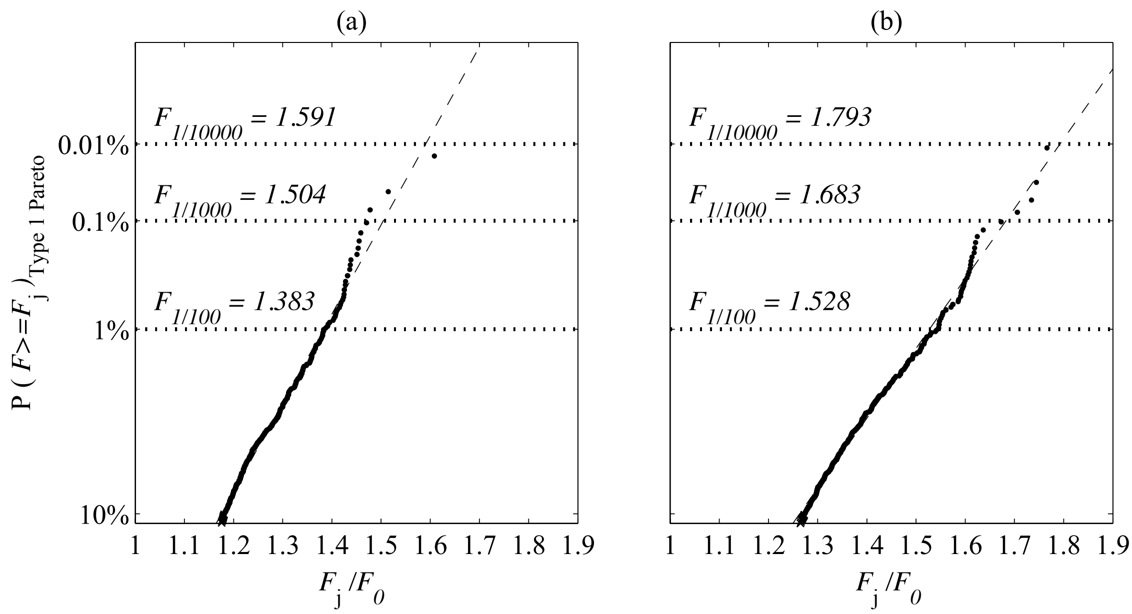

Figure 3.11 Probability plot for turbulent channel flow only. a) Current with *TI* of 12%. b) Sheared flow case with a *TI* of 14%.

The method based on extreme wave statistics was found suitable to characterise the support-structure forces experienced by a rotor when subject to flow representative of a full-scale turbine.

3.5 Extreme-Value Distribution

Two alternative probability distributions, Weibull and Normal were also considered for the rotor loading in the current flow condition of TI =12%. The previous peak-over-threshold technique with a threshold force of 1.1 was applied to the long run measurement for each distribution. The exceedance forces for the three methods were compared to those obtained with the Pareto method and the variation between each method was only 1% (Figure 3.12). The suitability of the two methods were also compared in terms of the fitting of the residuals to measurements, $R^2{}_{res}$ and convergence of the exceedance values against sample length, based on the extreme forces that are obtained with the Type 1 distribution using 30 minutes of continuous data (Figure 3.13).

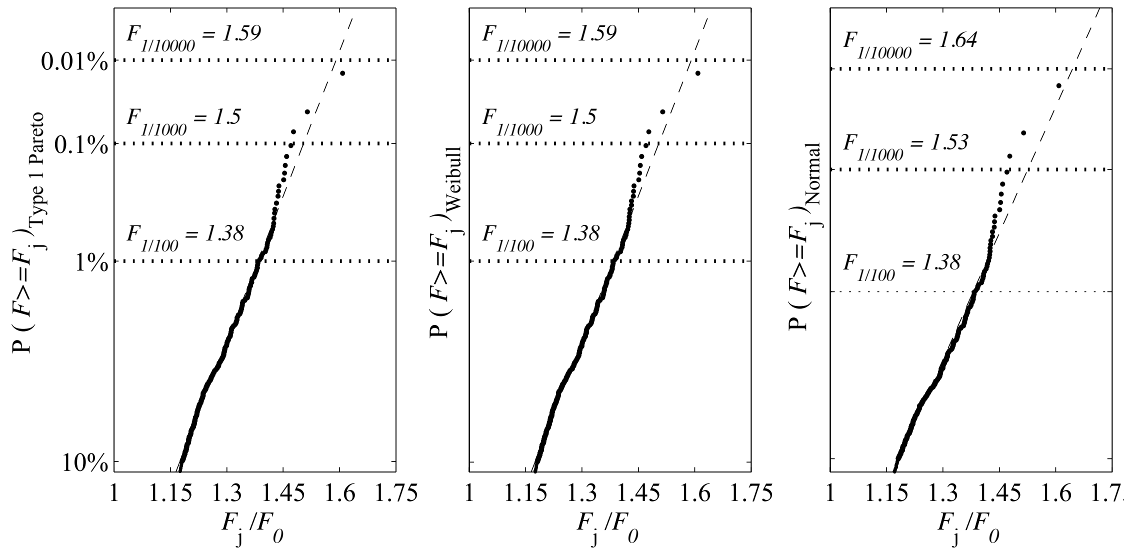

Figure 3.12 Probability force plots of three extreme methods in turbulent current with a TI =12% using a threshold force of 1.1 times the mean load. Modified from Fernandez-Rodriguez et al. (2014).

The Weibull distribution was found to provide a correlation coefficient of 0.98 and convergence of extreme values to less than 1% of the magnitude. The Weibull and

Type 1 method were concluded as more suitable than Normal since each method provided extreme values closer to that obtained from long run measurements with the use of a shorter sample.

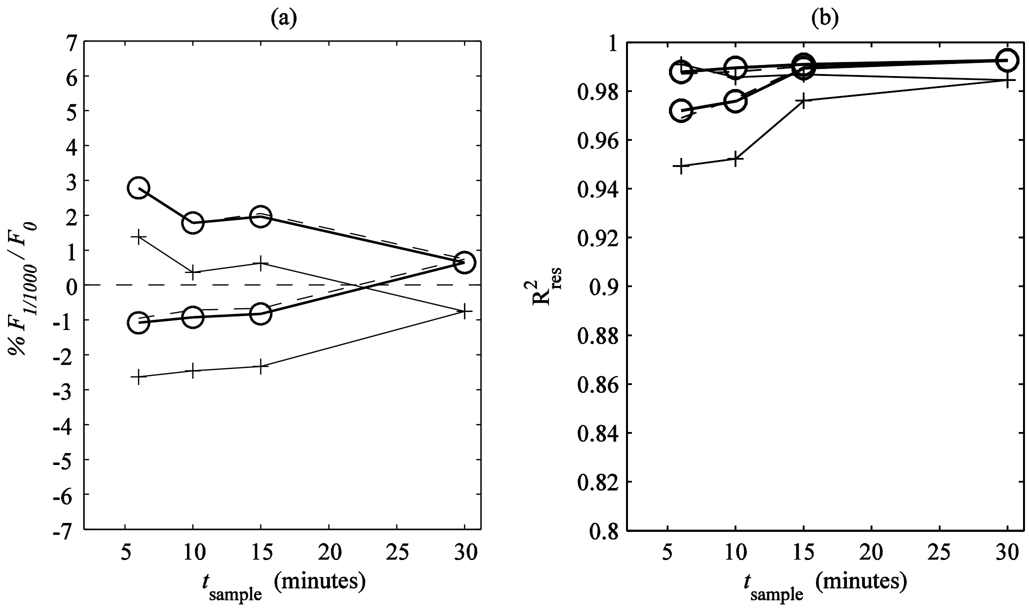

Figure 3.13 Comparison of the exceedance forces obtained using different extreme-value methods. a) Variation of exceedance loads obtained by the different methods. b) Square fit residuals against sample length using the Normal (+), Weibull (--), Type 1 Pareto (○-) and probability distribution. Modified from Fernandez-Rodriguez et al. (2014).

Prediction of exceedance force with each of the three extreme-value distributions provided similar magnitudes of extremes within 3% using a sample length of 10 min and a threshold force of 1.1 (Figure 3.13).

3.6 Conclusions

Implementation of a BEM method has been verified against published predictions and performance measurements of two 0.8 m diameter rotors in a uniform flow with low turbulence intensity and against measurements of a single 0.27 m diameter rotor in mean flow with TI =12%. The sensitivity of the power- and thrust-curve to high axial induction factors and tip loss corrections was investigated and indicated negligible variation due to overall rotor operation in low axial induction factors. A set of experiments was conducted to investigate the loading due to flows with turbulence intensity of 12% and 14%, representative of values at a tidal stream site. Mean values of thrust measured in the flow with TI =12% were 10% greater than those predicted with the BEMT. Blockage effects were applied to the experiments resulting in small percentage change to the thrust and power coefficient. Fluctuating thrust normalised to the mean, $\frac{F'_{\mathrm{rms}}}{F_0}$, was 0.14 and 0.21 respectively for the flows with TI =12% and TI =14% respectively. This compares with variance of 0.16-0.22 and 0.19-0.23 respectively, predicted based on an aerodynamic admittance model for load on a rectangular lattice in flow with comparable length scale in the streamwise direction.

A statistical analysis was employed to determine the force with probability of occurrence 1 in 100 (1%), 1 in 1000 and 1 in 10000 divided by their mean. The aim of the extreme load investigation was to characterise support structure forces in a turbulent channel-flow conditions representative of turbine design conditions. The 0.01% probability of occurrence force represents a return period of approximately 48 hours during this flow speed at full scale. A threshold value of 1.1 times the mean force was selected for the mean flow with TI =12%. The 0.1% force in the lower turbulent channel flow was 1.5 times the mean thrust. A 10-minute sample was found to be sufficient to obtain these parameters within 3% of the values obtained from the continuous, 30 minutes data. The prediction of loads was investigated with alternative extreme-value distributions providing extreme forces to within 3%. The Weibull and Type 1 probability function were found to converge using a shorter duration sample than the Normal distribution.

CHAPTER 4: LOADING OF OSCILLATING POROUS DISCS AND ROTORS

In this chapter, the loading on a tidal stream turbine due to time-varying onset flow is investigated to inform analysis of a rotor undergoing dynamic response. Loading is studied for a three-bladed rotor, as Chapter 3, and for a porous disc with equivalent mean thrust. The porous disc and rotor are forced to oscillate with sinusoidal motion in different flow conditions. The porous disc is initially investigated in still water and then, along with the rotor, in steady, turbulent channel flows. The inertia and damping coefficients of the rotor and disc are obtained for a range of amplitudes and frequencies of streamwise oscillations, characterised by Keulegan Carpenter (KC) number. The hydrodynamic parameters obtained from these experiments are employed in Chapter 6 as input to an analysis of the dynamic response of a support structure.

4.1 Introduction

It is increasingly recognised that in order to harness offshore wind and tidal resources at deep-water sites (>30m) in a viable and commercial manner, it is necessary to develop alternatives to bed-mounted turbine supports (Musial et al., 2004). Several systems where one or more turbines are supported on a moored floating platform have been proposed as cost-effective approaches, but require a further understanding of the support loading and the rotor's interaction. The floating platform is principally required to provide stability in all conditions, ensuring the system's survivability and conforming to the manufacturer's turbine specifications. For example, the rotor operation should be within the allowed angle of (rotor) pitch oscillation (<9˚) and within the limit for nacelle acceleration (Berthelsen and Fylling, 2011). Furthermore, to assess the reliability of an offshore system, the occurrence and magnitude of the support loads must be determined for return periods of 1 and 50 years (IEC61400-3, 2009). Such an approach, as followed in the thesis, may first consist of determining the forcing on the turbine due to the structure dynamics and incorporating the response in a structural model. Then available statistical methods can be applied to the time-history simulations to extrapolate the exceedance values.

The hydrodynamics of the support configuration may be approximated using linear diffraction methods such as WAMIT^{TM} (Lee and Newman, 2006) by neglecting turbulence in the ambient flow and accounting for the Doppler shift frequency of the wave due to the imposed current. However, a major restriction of this assessment method is that the rotor loading imposed under the motion due to a floating or flexible support structure is not fully defined. The dynamic rotor loading may be due to a combination of forces from the hydrodynamics and thrust in the ambient flow, and may also depend on the frequency and amplitude of the streamwise oscillations.

In this study, the aim is to quantify the hydrodynamic coefficients of added mass, C_{a}, drag, C_{D} and damping, C_{b}, of an operating turbine based on a system that forces oscillation of the rotor. This is to enable prediction of the force which will, in turn, enable prediction of response amplitude of rotor oscillation in a dynamic simulation. A comparison with the rotor hydrodynamics is made using a porous (perforated) disc that provides similar drag coefficients of 0.89±5% in incident uniform flows. Here, the definition of the steady drag coefficient is analogous to the rotor thrust, $C_{\mathrm{T}} = C_{\mathrm{D,c}} = \frac{2F}{\rho A {u_0}^2}$.

Thin porous discs are a simple representation of the rotor's energy extraction and have been used for the analysis of complicated flow phenomena such as the wake generated by a turbine, the array characterisation, and the impact on the natural tidal stream, as well as for the study of array-spacing effects (Myers and Bahaj, 2006; Harrison, Batten, and Bahaj, 2010; Batten et al., 2013; Draper et al., 2013).

The design of a disc equivalent to a rotor is quite complex due to the variation of the drag with the pattern of the holes, the shape of the disc and its dependence on the operating-flow characteristics such as turbulent intensity (TI), the Keulegan Carpenter Number (KC), the Reynolds number (Re), and the integral length scales in the streamwise direction (Blackmore et al., 2014).

The Keulegan Carpenter Number, KC, is a dimensionless parameter frequently employed to describe the amplitude of the velocity oscillation or planar motion, $\|x\|$, relative to the typical dimension, e.g. the diameter, D, of the structure. It is defined:

$$KC = \frac{2\pi\|x\|}{D} \qquad \text{Eq. 4.1}$$

The Reynolds number is the ratio of the inertia and viscous forces that describes the flow regimes relative to the surface of the porous plate and is defined with the dynamic viscosity of the working fluid, μ, the upstream velocity, u_0, and diameter of the disc, D:

$$Re = \frac{\rho u_0 D}{\mu} \qquad \text{Eq. 4.2}$$

An appropriate disc is typically obtained experimentally by adjusting the net thrust coefficient acquired with the number and size of the perforated holes, the area of the openings, the geometrical configuration and the thickness of the plate, t_{th}. The porosity ratio, τ, a particular characteristic of the employed disc, is defined as the area ratio between the holes and the total plate area (Molin and Nielsen, 2004). Values of the porosity ratio range from 0 to 1. An alternative porosity definition, not currently used in the present work but often referred to in literature reviews (Vu et al., 2004; Tao and Dray, 2008), is the area ratio between the openings and the solid portion. The discs normally employed to represent tidal rotors have porosity ratios in the range 0.14–0.6 (Xiao et al., 2013; Sun et al., 2008; Blackmore et al., 2014) and thrust coefficients 0.7-1.3 in flows with TI =10-13%.

Although studies have shown a comparable energy extraction and thrust characteristics within arrays of rotors and discs, little has been shown on the disc effectiveness in oscillatory motion, its interaction with wake reversal and the appropriate methods to quantify the hydrodynamics to achieve a rotor comparison.

Initially, the loading on a disc oscillating in the streamwise direction is investigated in a quiescent flow using the Morison equation and then compared with the performance in incident flows with turbulence. The equation of Morison et al. (1950) is a well-known formula to describe the loading imposed on bluff bodies due to oscillatory flow. Several alternative forms of the Morison force exist (see Section 2.12). For a disc undergoing forced oscillations in a quiescent flow, the force, F_{m}, is the sum of an oscillatory drag and inertia force. It is given from Eq. 2.39 and Eq. 2.44.

Likewise, the forcing of the disc due to streamwise motion may also be considered as analogous to hydrodynamic studies on representative dampers such as square or circular solid plates. These plates are forced to experience oscillations either in heave or surge, whereby the measured force is expressed as the sum of an added mass (a) and a damping (b) force, given by Eq. 2.50.

The use of heave damping plates has been applied on some oil floating platforms such as spar structures to increase the stability and reduce any possible resonance. Resonance results in large-vibration motions, due to the system's operation in its natural period, and can cause early failure of the floating support when the ultimate mooring force has been exceeded (De Silva, 2010; Feng et al., 2012).

Eq. 2.50 considers that damping of the disc follows a linear relationship with the velocity of oscillation. Nevertheless, the damping of the disc may be due to a combination of linear and non-linear mechanisms including viscous drag and damping. These individual (non-linear) effects are often difficult to solve in the time domain, but can be approximated over a cycle of motion as a total force with an equivalent viscous damping (Kelly, 2011; Norton et al., 2003). Two important parameters for a disc undergoing small oscillations are then determined using the linear damping formulation (Eq. 2.50) and total damping of the disc, given with the equivalent viscous damping. Sarpkaya and Isaacson (1981) provide the formula for cylinders in oscillating flows in terms of the oscillatory drag coefficient. The equivalent damping is:

$$b = \frac{1}{3}\mu\beta D C_{\mathrm{D}} KC \qquad \text{Eq. 4.3}$$

It is commonly accepted that the vortex shedding due to the sharp edges of the disc and the openings, along with the friction resistance of the disc determine the damping characteristic of the disc. The friction resistance is due to the forces acting parallel to the walls, which is dependent on the thickness of the disc. The effect of friction resistance is relevant for applications with small amplitudes of oscillations, in which the operating KC number is less than 0.2. The ratio $\frac{Re}{KC}$ characterises such flow condition in the boundary layers along the disc by relating the dynamic response of the disc relative to the operating fluid. It is referred to as either the Stokes number or Frequency number and is expressed as:

$$\beta = \frac{D^2 f \rho}{\mu} \qquad \text{Eq. 4.4}$$

Due to small thickness of discs often employed in the heave tests, variation of damping due to Frequency number is usually small. Variation due to symmetry of holes and shape of disc is hence of more relevance, which is described by the drag coefficient against the KC number.

4.2 Review of Hydrodynamics of Oscillating Porous Discs in Still Water

Solid plates have been used as external keels, truss structures, wave absorbers and dampers of an oil floating structure. Although the vertical motions experienced on various floating platforms are relatively small compared to the length characteristic of the structure, e.g. diameter (see Table 4.1), these can still be quite detrimental for the stability and drilling activities performed. For the safekeeping of the device and to prevent any possible resonance motion, either a limit is imposed on the dynamic system response or the properties of the platform are modified so that the operating frequency stays above the natural frequency. The current view held by many authors (Molin, 2001; Molin and Nielsen, 2004; Tao et al., 2007) is that the damping of a plate limits the response amplitude of the platform and its magnitude may be increased by the use of a perforated (porous) plate at the small Keulegan Carpenter range, KC<1. At KC numbers above unity, the damping of a solid plate is greater and there is no benefit in using plate porosity. According to Molin (2001) the use of a porous disc would be optimised at the low porosity range τ<0.2 providing damping coefficients up to 4.75 times of that obtained using a solid disc.

Table 4.1 Operational amplitude of motions of typical deep-water offshore structures.

Offshore Structure	KC
Spar or Truss spar	<1 (Tao and Dray, 2008)
Spar, $D/2$ =15m, $\|x\|$=1m, bilge keels	0-2 (Molin, 2001)
TLP (springing motion)	0-0.01 (Tao and Cai, 2004)

A particular consideration relates to the spar oil structures commonly used at deep-water locations. These structures ensure safe operation in harsh wave conditions by possessing large resonance periods in heave, surge and pitch, typically around 25, 160 and 60 seconds respectively (Rho et al., 2002; Kurian et al., 2008). Resonance motion is therefore mostly avoided in the sea states, except for a few deployment sites comprised of swell waves with comparable heave natural frequencies (Tao et al., 2007). Increasing the mass of the spar support is an approach to counteract the resonance motion (Tao et al., 2007), but nevertheless, it also contributes to detrimental issues such as higher capital costs and longer production time. Additionally, a larger hull is required and this produces higher forces due to waves, deep-water currents, vortex forces on the hull and hence increases the tension on the mooring lines, amongst others (Downie et al., 2000; Sadeghi et al., 2004). For these reasons, a type of support structure is designed with a truss attached to the cylinder hull with a series of horizontal solid plates to decrease the heave displacements (Figure 4.1). The cylinder height is thus shortened, reducing the loads in the tension lines, as well as material and capital costs. Increasing the damping of the plates by using the porosity property is therefore very simple and beneficial.

Figure 4.1 Scale model of a spar truss platform. Source from Montasir and Kurian (2011). The horizontal plates attached to the truss are employed to decrease the vertical motions of the structure.

The hydrodynamics of the heave discs typically vary with the ratio of thickness over diameter, porosity ratio, array spacing, operating Reynolds number and KC number (Lake et al., 2000; Tao et al., 2007; An and Faltinsen, 2013). The added mass and damping of the disc is usually quantified as a proportion of the added mass predicted for a non-perforated disc, M_{a} (see Section 2.12, Eq. 2.51). This added mass is equal to the water mass enclosed by a spheroid of major axis equal to D and minor axis equal to D/π, thus $M_{\mathrm{a}} = 1/3\rho D^3$. The hydrodynamic coefficients obtained using normalisation by mass into Eq. 2.50, are as stated in Eq. 2.52.

Several numerical and experimental studies have addressed the damping mechanisms in heave for solid plates and for those pierced with small holes. The damping coefficient of discs with porosity range, τ of 0.05 to 0.25, have been found to increase almost linearly with KC between 0 and1.6 with magnitudes between 0 and 0.2 and slopes of 0.2 (Vu et al., 2004). The damping obtained in discs with porosity ratios less than 0.1

have been shown to exceed the solid case (Vu et al., 2004; Tao and Dray, 2008). The maximum increase of damping of a porous over solid disc was obtained with porosity ratio .05-.1 for a KC of 0-0.2. For this range, the peak damping of the porous disc was approximately 2.4 times the damping of the solid disc.

The oscillatory drag coefficients, C_{D}, of low porosity discs of τ =0-0.18 have been found to decay exponentially to the limiting values of 5-7 with increasing KC. The added mass for the solid disc has been found to be similar to the value obtained by potential flow theory and was shown to decrease with increasing porosity, up to 50% for the porosity case of 0.18 (Tao and Dray, 2008).

4.3 Comparison of Forced Oscillation of Rotors and Discs in Uniform Flow

The performance achieved as a result of forced rotor (axial) motion has been of recent relevance for the design and study of wind and tidal floating offshore devices. Particularly, the mean and variance of the rotor loading resulting from dynamic response is a key factor for the life assessment of the floating systems. This response has been analysed with support-structural response methods coupled to aero-hydrodynamics and rotor performance outputs from standard BEM codes (Moriarty and Hansen, 2005; Salzmann and Van der Tempel, 2005).

The added mass of a wind turbine is often small relative to the mean aerodynamic load and the resultant damping is only significant for dynamic responses in the low frequency range, f<0.3 Hz (Karimirad and Moan, 2010). However, for tidal devices the added mass of the resulting wake and separation, tower interactions, and turbulence effects can be significant compared to the mean thrust due to high density of the operating flow. Variation of loading at the rotor frequencies, and higher frequencies, is also influenced by factors such as tower shadow, shear flow and vibration of the supporting structure. Nevertheless, unsteady processes associated with oscillation of the onset flow are typically considered to be a greater influence on overall performance of tidal stream devices. Operating conditions are often approximated by predictions performed in steady-state oscillations averaged over discrete-time intervals, characterised by a time ratio, e.g. $\frac{D}{u_0}$. Due to typical length dimensions of tidal stream turbines and speed range of the operating flows, the time scale to obtain a quasi-steady approach is T_{amb} ≈5-10 seconds

(McCann et al., 2008; Whelan et al., 2009b). A key uncertainty, discussed in the next chapter, is whether the oscillatory incident flows due to waves produce similar forces to the induced motions and if these can be accurately predicted using a quasi-steady approach.

It is known from the wind industry that abrupt changes to either the incident flow, angle of attack of the blade, or rotational speed of the rotor have a delayed effect on the formation of the wake. This condition is the result of loads not responding to the rapid change of incident flow speed, as flow requires a certain time to progress from the sections of the blade to downstream. The same effect of force on the blade sections is applicable if the angle of attack is rapidly modified, due to the rapid change of the blade's lift and drag. This is referred to as the dynamic inflow and is apparent as a time lag in the rotor's measured response (Hansen, 2012). The given behaviour has been accurately modelled and validated with methods such as that proposed by Pitt and Peters (1981), where an extra force due to the axial flow acceleration through the rotor is subtracted from the thrust calculated using numerical approaches such as standard BEM codes.

This analysis has been extended to study performance of tidal rotors when subjected to a mean flow combined with waves. Nonetheless, the extra force obtained from the force measurements and BEM predictions due to varying velocity and angle of attack of the blade has been found to be relatively small, contributing only 1-3% of the steady load (Maniaci and Li, 2011; Faudot and Dahlhaug, 2012; McNae and Graham, 2014). The mean thrust coefficient remained almost the same as the flow without waves.

Some experimental work has been conducted on rotors and discs undergoing dynamic forcing, whereby measured force is studied in an analogous manner to a circular cylinder. An extensive literature exists for hydrodynamics of circular cylinders undergoing streamwise oscillations in steady flows, where the measured force is quantified with a Morison equation in a relative plane axis. The predicted force is obtained from Eq. 2.39 and Eq. 2.45.

Whelan et al. 2009b studied the thrust on a rotor and disc undergoing streamwise oscillation within steady flow based on this approach and reported that the magnitudes of the oscillatory drag coefficients were between 1.8 and 2.4 for the range of KC 0-2. Nevertheless, it also indicated that given formulation is unsuitable for describing the time-varying load. Therefore, other methods should be re-considered. An alternative form, which has been found to fit the time-history measurements of thrust more accurately for porous plates, consists of separating the drag contribution of the oscillatory flow from the mean (Verley and Moe, 1979) and is given by Eq. 2.48.

Additionally, the unsteady performance of a tidal rotor and equivalent disc undergoing streamwise oscillations in a highly blocked channel provided the insight that the inertia was small for the amplitude ranges, KC of 0-2 (Whelan et al., 2009b).

4.4 Experimental Arrangement

The aim of this section is to investigate the loading of a single rotor in time-varying onset flow relative to the loading of rotor in steady flow and to evaluate the suitability of a porous disc of similar thrust to represent the rotor response. Experiments were conducted using a support structure that forces sinusoidal oscillation of the rotor in turbulent channel flows. The arrangement of the flume, the method of flow generation, the rotor geometry and constraint as well as angular measurement and thrust are as in Section 3.2. The turbine supporting structure is attached, above water level, on a base plate containing stub axles mounted to pillow bearings securely attached to a gantry that spans the flume. This configuration develops small oscillations in pitch, θ_{r}, around the stub axis located at distance $L = 790$ mm above the rotor axis. The length of the tower is 2.96 times the rotor diameter and thus, the imposed motion of the rotor is given as $x \approx L\theta_{\mathrm{r}}$. The drive train consists of a scotch yoke affixed to one stub axle, which is driven by a geared DC motor with a low-friction pin. Figure 4.2 shows arrangement of the equipment with the rotor being replaced by the equivalent disc.

A mechanical torque is applied to the rotor shaft to counteract the torque developed by the rotor in the quiescent and turbulent channel flows. Supply of a constant electrical current to the geared motor produces torque with magnitude in the range 0-5 N-m. The amplitude of the oscillation is specified by the eccentricity of the Scotch yoke mechanism, and the frequency specified by the electrical current supplied to the geared DC motor. The displacement in surge is measured with an optical encoder mounted at the far end of the right stub axle with a resolution of $\pi/100$. Since thrust curve of the rotor is almost flat for the TSRs of 4.5–6, a disc with one porosity ratio only was considered. The porous disc had a diameter, D, of 0.27 m with 264 holes of 12 mm diameter and hence the porosity ratio is 0.52. This porosity was selected experimentally following measurement of the thrust on porous discs with a range of porosity ratios and porosity geometry. The selected porosity ratio developed a drag coefficient comparable to the rotor due to turbulent flow of TI= 12%. The time-varying thrust and linear displacement was recorded for 60 s sampled at 200Hz. A thrust coefficient of C_{T} =0.87±4% was measured in steady flow with depth-averaged velocity, U_0 =0.46 m/s. The time-varying force was measured for oscillation amplitudes $\|x\| = [0.007 - 0.32]D$ and frequencies of 0.45-1.2 Hz corresponding to KC = 0-2.2. The corresponding range of Reynolds number, based on maximum velocity and disc diameter, and Stokes parameter were Re =[4.8-641]×10^3 and β =[29-87.4]×10^3.

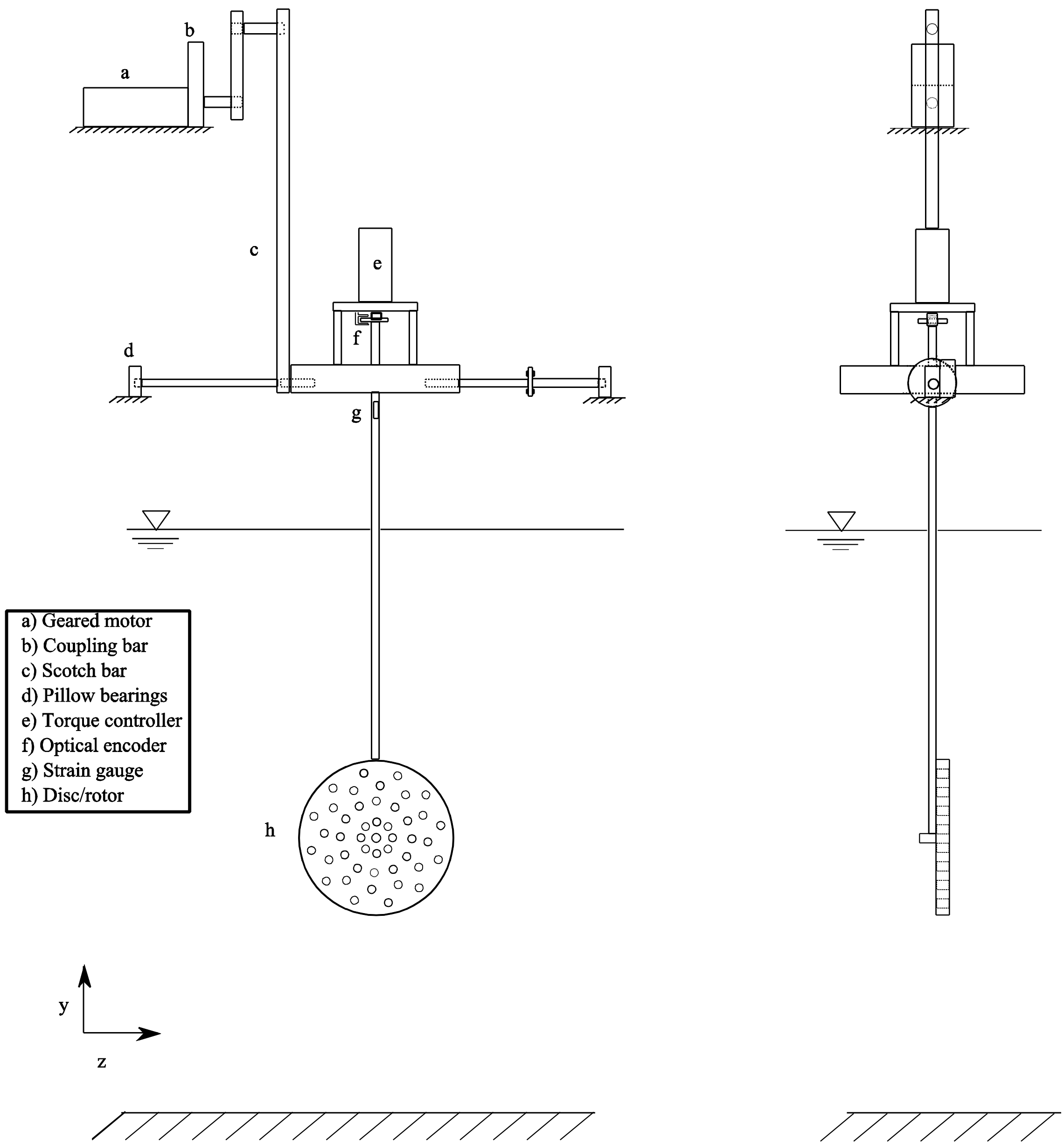

Figure 4.2 Diagram of the driving support structure. Front and side view of the equipment with description of main components. Not drawn to scale.

4.5 Drag and Damping of Oscillating Porous Discs in Still Water

The hydrodynamic force on the disc is approximated as the measured force, F_{m}, minus the mechanical force associated with drag of the oscillating support, $F_{\mathrm{mech,t}}$. The mechanical force is quantified prior to attachment of the disc in the same fluid condition characterised by the KC. Buoyancy forces on the disc are neglected due to the nearly constant depth of immersion of the rotor. The equation of motion of the rotor based on Eq. 2.50 and Eq. 2.52 is:

$$-\frac{2}{3}\omega\rho D^3 C_{\mathrm{b}}\dot{x}-\frac{1}{3}\rho D^3 C_{\mathrm{a}}\ddot{x} = F_{\mathrm{m}} = F_{\mathrm{osc}} - F_{\mathrm{mech,t}} \qquad \text{Eq. 4.5}$$

The measured amplitude of the streamwise motion is determined as the amplitude of a sine wave that is a best fit to the measurements using the least-squares method. The angular velocity and acceleration of the disc in the streamwise motion are thus estimated as the first and second time derivative of this fitted displacement. The hydrodynamic coefficients $(C_{\mathrm{a}}, C_{\mathrm{b}})$ are obtained by Eq. 4.5 as the least-squares best fit equal to F_{m} (Figure 4.3).

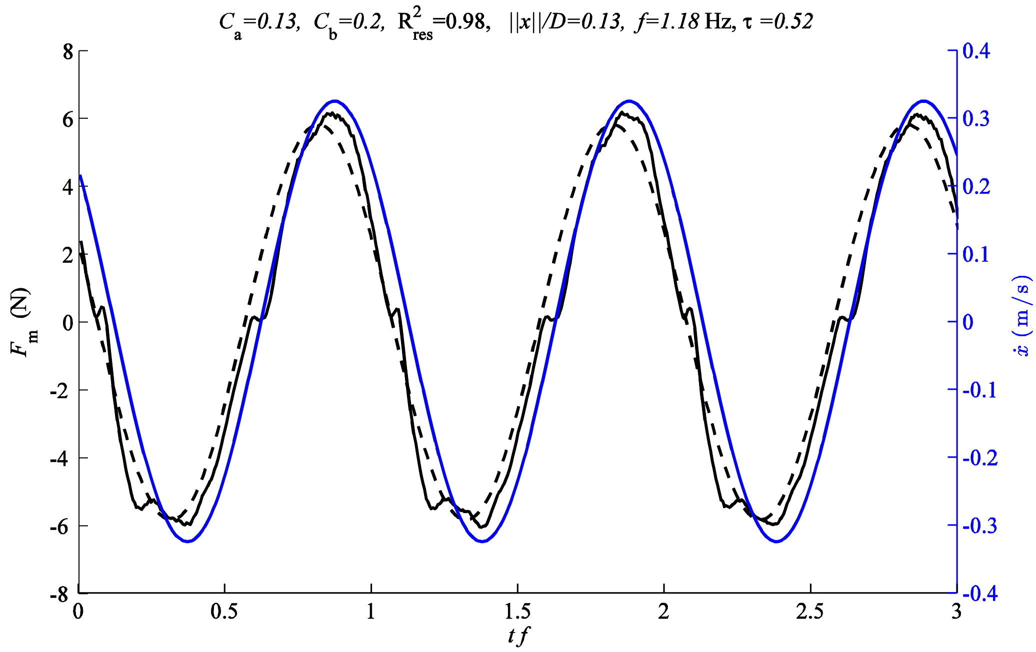

Figure 4.3 Excitation force of disc due to sinusoidal axial oscillation in quiescent flow. On the left axis, comparison of the measured (-) and predicted force (--) with the added mass and damping force for one amplitude of oscillation. On the right axis, the velocity of the disc due to forced motion in the streamwise direction (—).

The resultant added mass and damping coefficients from best fits with least-squares residuals R^2_{res} >0.95 vary with KC for different Frequency numbers (Figure 4.4). The damping coefficients for each β case were found to increase almost linearly with KC. Linear trend lines obtained by a least-squares approach had slopes of 0.152 with only a 6% variation with Frequency number (Figure 4.4). In the test conditions studied, a small phase difference was observed between the predicted velocity and the measured force due to a low added-mass contribution (e.g. Figure 4.3). The added mass coefficients fluctuated around a mean of 0.12 for the amplitude range, KC<0.5, but exhibited greater scatter at the higher amplitudes, perhaps due to a lower magnitude of the inertia relative to the increasing damping force. A similar low added mass contribution is expected on a full-scale rotor. It was also concluded from the review of heave studies of discs that increasing the porosity ratio to 50% reduces greatly the damping (slope) compared with a solid disc and the added mass becomes negligible.

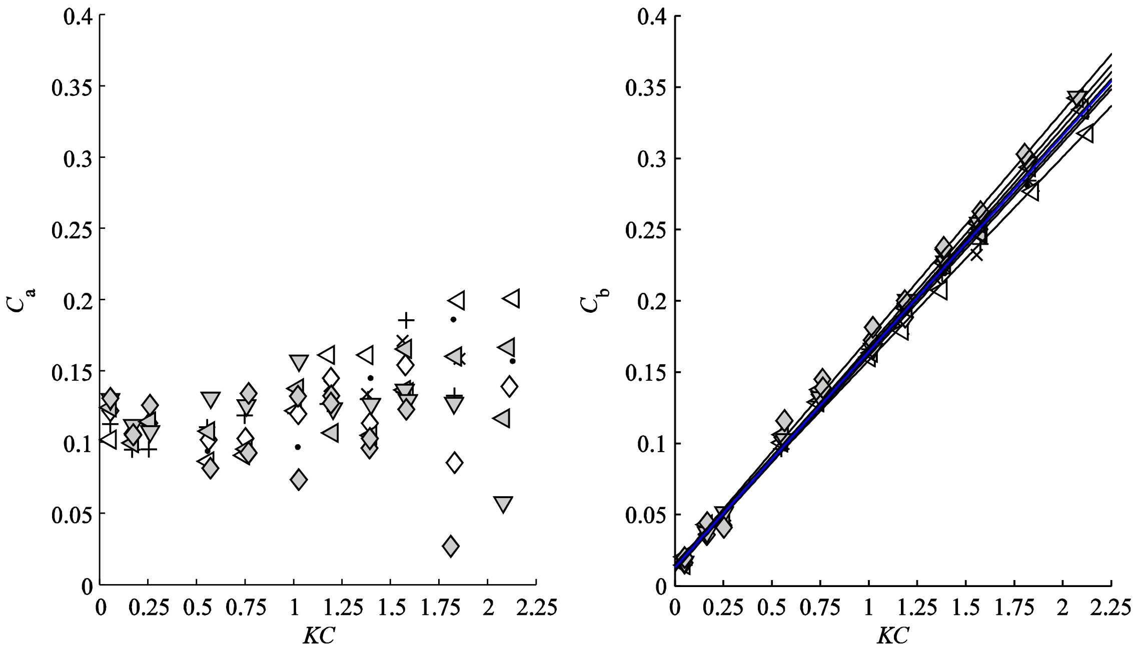

Figure 4.4 Variation of added mass (left) and damping coefficients (right) against KC for a disc of porosity ratio 0.52 at different β numbers. x, β =3.65×10^6±5%; ◁, β =4.37×10^6±5%; +, β =5.1×10^6±5%; ●, β =5.83×10^6±5%; ◊, β =6.56×10^6±5%; ◀, β =7.29×10^6±5%; ▼, β =8×10^6±5%; ♦, β =8.75×10^6±5%. Best least-squares fit line of the damping coefficients at each (-) and all Frequency numbers (—) using the linear force of Eq. 4.5.

The oscillatory drag coefficients from the linear viscous damping force were calculated from Eq. 4.1, Eq. 4.3, Eq. 4.4 and Eq. 2.52. A comparison was then made with the force coefficients obtained from the measurements using the Morison equation (Eq. 2.39 and Eq. 2.44) with added mass normalised to a spheroid (Eq. 2.51). The oscillatory drag coefficient and added mass coefficient were obtained with a least-squares fit giving residuals within the range R^2_{res}>0.93.

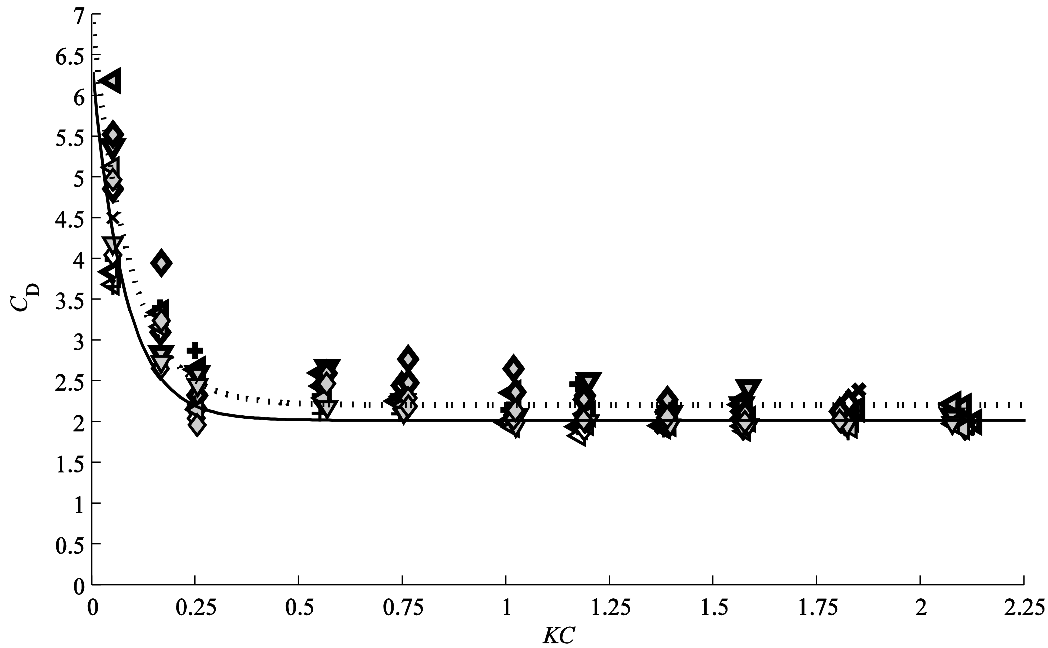

Figure 4.5 Measurements compared to the average trend of the linear (--) and Morison drag coefficient (—) in the quiescent flow with the KC number for different β numbers. Markers for β describing the linear (thick edge) and drag coefficient (thin edge) are as shown in Figure 4.4.

The linearised oscillatory drag coefficient across different β was found to decay exponentially with KC to the limiting magnitude of 2.22. For all the tests, the decay formula given by a best least-squares fit was $C_D = 2.22 + 4.54e^{-\xi KC}$ (Figure 4.5), where ξ =9.61 represents the attenuation rate of the oscillatory drag with KC, and its magnitude, as stated by He et al. (2008), is proportional to the damping coefficient of the plate. The attenuation rate varied with the β employed, and this was within 13% of the average trend. The highest discrepancy of the drag coefficient with the average trend occurred at KC of 0.1-0.75 with the largest β number employed. The Morison oscillatory drag coefficient was similar and in good agreement with the linear viscous drag. It decayed exponentially with KC to the limiting drag coefficient of 2.03. The mean added-mass coefficient across the KC range of 0-2 was around 12% of that for a solid disc (Figure 4.6). This behaviour was consistent with the results of Eq. 4.5.

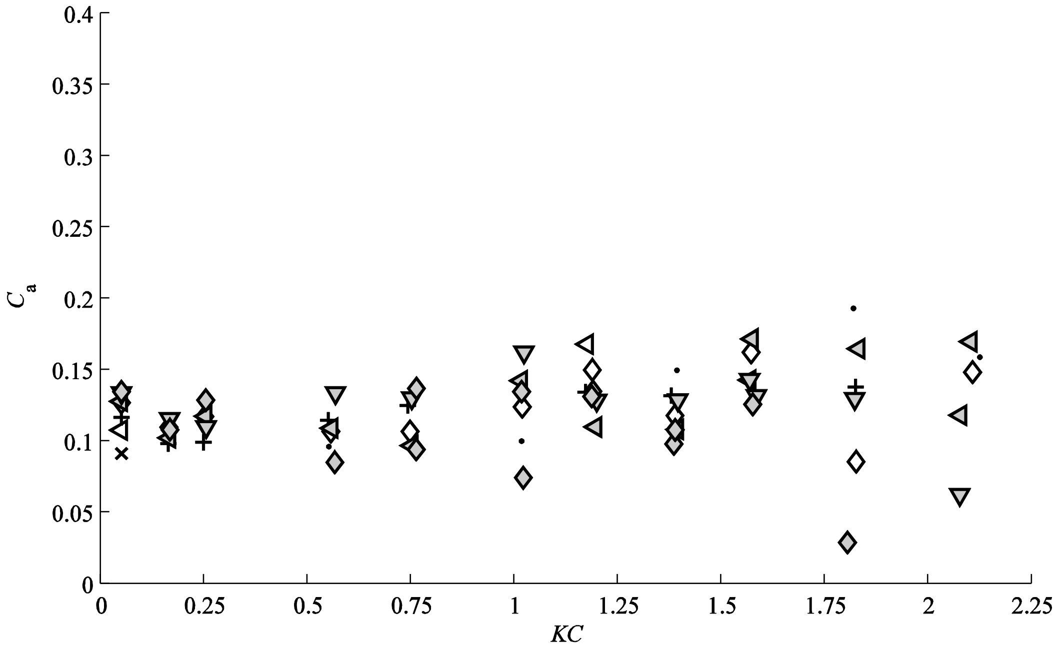

Figure 4.6 Inertia coefficient in the quiescent flow using Eq. 2.39 and Eq. 2.44 with KC parameter and different β numbers. Markers for β number are as shown in Figure 4.4.

4.6 Drag and Damping of Oscillating Porous Discs and Rotors in Turbulent Flow

The time-varying force due to forced harmonic oscillation was also measured for the porous disc and for a single rotor in turbulent channel flows of mean velocity 0.32, 0.39 and 0.46 m/s at the hub height. For some combinations of mean incident speed and amplitude of streamwise oscillation, the minimum speed of the relative motion between the water and rotor is lower than the operating speed for the rotor, which means angle of attack is increased and stall would occur. Force on the rotor was therefore analysed for conditions in which the rotor operated continuously, corresponding to a limited KC range and velocity ratio, $\frac{\|\dot{x}\|}{u_0} < 0.5$. However, force on the disc was measured for the same KC

range as in still water. The stationary mean thrust of the disc in the turbulent channel flows was F_0 =5.5N±4% corresponding to a thrust coefficient C_{T} =0.87±4%.

The presence of a mean flow changes the formation of the wake compared to oscillation in quiescent fluid and so the drag due to oscillation in still water differs from drag (or damping) due to oscillation in steady flow. Most authors (Chakrabarti, 1987; Journée and Massie, 2001; Sumer and Fredsøe, 2006; Nakamura et al., 2013) address the discrepancy by defining a Morison equation based on the relative axial velocity between the water and the body as stated in Eq. 2.39.

However, several studies of rotors undergoing forced axial motion (Whelan et al., 2009b; Milne et al., 2011) have stated that the excitation force is better represented as a stationary disc in steady flow added to a force due to the relative axial motion between the water and the rotor, F_{osc}. The mechanisms involved in such observations and the flow regime relationships acquired in the rotor between the mean flow and the axial motions have not been fully understood.

The dynamic force was initially investigated using Eq. 2.39 and Eq. 2.46 with a method similar to Eq. 4.5. This approach consisted of the axial force being equal to the measured force, minus the mechanical drive and force on the tower obtained, $F_{\mathrm{mech,t}} \sim 0.08 F_0$, without the disc, for KC in the range 0–1. The incident flow had a constant velocity, u_0. However, the simulations employing Eq. 2.39 and Eq. 2.46 were found to provide a poor approximation to the measured time-varying force with least square residuals typically less than 0.4.

Following the alternative form of force (Eq. 2.49), the components of the relative axial velocity between the disc and the water were then expanded, to treat the drag due to the current and streamwise oscillation as separate forces. The volume of the rotor was expressed with the water mass enclosed by a spheroid (Eq. 2.51).

In Eq. 2.49, drag force due to steady flow and drag force due to oscillator flow are proportional to different drag coefficients. Furthermore, if the time-varying displacement is provided by an equation such as $\dot{x} = \|\dot{x}\| \cos(\omega t)$ and the range of velocities is limited to $u_0 > \|\dot{x}\|$. The first component of drag in Eq. 2.49 is:

$$F_{\mathrm{D,1}} = \frac{1}{2}\rho A C_{\mathrm{D,1}} u_{\mathrm{c}} |u_{\mathrm{c}} - \dot{x}| = \frac{1}{2}\rho A C_{\mathrm{D,1}} {u_{\mathrm{c}}}^2 - \frac{1}{2}\rho A C_{\mathrm{D,1}} \dot{x} u_{\mathrm{c}} \qquad \text{Eq. 4.6}$$

From this arrangement, it is seen that the first expression on the right hand side approaches the force acquired on a rotor that is rigidly supported in a mean flow with turbulence present. Here, the drag coefficient is assumed to remain the same and is defined analogous to the drag or thrust coefficient for the ambient flow with u_0 =0.46 m/s, thus $C_{\mathrm{D},1} = C_{\mathrm{D,c}} = C_{\mathrm{T}}$ =0.89 m/s. The second term in Eq. 4.6 becomes an extra force with drag coefficient proportional to the velocity of the streamwise oscillation multiplied with the turbulent current. For the speed ranges considered, the magnitude of this force, $F_{\text{neglected},1} = \frac{1}{2}\rho\dot{x}u_{\mathrm{c}}AC_{\mathrm{D},1}$, is small when compared to the first term, and is thus neglected. Following rearrangement and simplification, this first component of the drag force, associated with the turbulent flow is (see Eq. 2.39 and Eq. 2.41):

$$F_{\mathrm{D},1} \approx F_0 + F' \qquad \text{Eq. 4.7}$$

where $F_0 = \frac{1}{2}\rho AC_{\mathrm{D,c}}u_0{}^2$ is a mean force and $F' = \frac{1}{2}\rho AC_{\mathrm{D,c}}\left(u'^2 + 2u_0u'\right)$ is the force due to the turbulent fluctuations. For the second drag in Eq. 2.49, the drag contribution of turbulent fluctuations is separated from the streamwise oscillation component, by re-writing the turbulent current as the sum of a mean and a zero-average fluctuation component (Eq. 2.40). This provides an arrangement, such that the second drag is mainly attributed to a single force with drag coefficient, $C_{\mathrm{D},2}$, which is proportional to the multiplication of velocities between the relative flow (disc and water) and the rest frame associated with the streamwise oscillations. The second component of the drag force becomes:

$$F_{\mathrm{D},2} = -\frac{1}{2}\rho AC_{\mathrm{D},2}\dot{x}|u_{\mathrm{c}} - \dot{x}| = -\frac{1}{2}\rho AC_{\mathrm{D},2}\dot{x}|u_0 - \dot{x}| - \frac{1}{2}\rho\dot{x}u'AC_{\mathrm{D},2} \qquad \text{Eq. 4.8}$$

In Eq. 4.8, the force $F_{\text{neglected},2} = \frac{1}{2}\rho\dot{x}u'AC_{\mathrm{D},2}$ is assumed with a drag coefficient similar to the first part. It remains small for the range of streamwise speeds considered and is thus neglected.

The Morison equation for the disc and rotor subjected to streamwise oscillations in a mean flow with turbulence, ignoring the small terms in Eq. 4.6 and Eq. 4.8, is approximately due to the force of a rigid disc in the turbulent channel flow, which is then added to a drag and inertia force due to the streamwise oscillations. The modified expression is:

$$\frac{1}{2}\rho AC_{\mathrm{T}}u_{\mathrm{c}}{}^2 - \frac{1}{2}\rho AC_{\mathrm{D},2}\dot{x}|u_0 - \dot{x}| - \frac{1}{3}\rho D^3C_{\mathrm{a}}\ddot{x} = F_0 + F' + F_{\mathrm{osc}} \approx F_{\mathrm{m}} \qquad \text{Eq. 4.9}$$

This approach provided a best fit to the measured data with residuals greater than 0.85. To assess the accuracy of the oscillatory drag coefficient, the higher frequency oscillatory forces, which are included in Eq. 4.9 as F' only, were extracted from the measured force using a third-order band-pass Butterworth filter. The oscillatory force was defined for a frequency range with threshold values of ±20% of the frequency of forced oscillation, f.

The hydrodynamic parameters for both the disc and single rotor in the turbulent channel flows were then calculated from measurements using a best-fit force (Eq. 4.9) with the least-squares residual R^2_{res}>0.92. The trend of the oscillatory drag coefficients in the quiescent flow tests were also compared to the mean flow with turbulence present. The variation due to the β number was small and thus neglected.

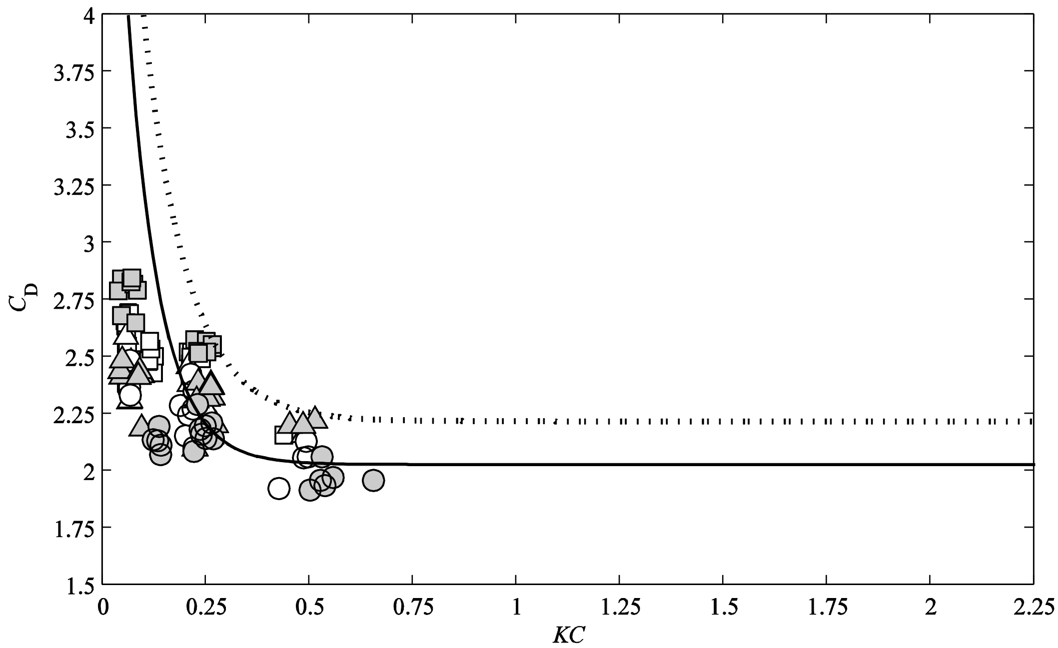

Figure 4.7 The oscillatory drag coefficients obtained in the quiescent and mean flow conditions with turbulence against KC number. □, disc in flow of u_0 =0.35 m/s; Δ, disc in flow of u_0 = 0.39 m/s; ○, disc in flow of u_0 =0.46 m/s. ■, rotor in flow of u_0 =0.35 m/s; ▲, rotor in flow of u_0 =0.39 m/s; ●, rotor in flow of u_0 =0.46 m/s. Trend line of oscillatory drag for quiescent flow using linear viscous (--) and Morison Equation (—).

The drag coefficient of the porous disc and single rotor in the turbulent channel flows decayed exponentially with KC to a constant drag coefficient in an analogous manner to the quiescent flow tests, thus $C_{D,2} \approx C_D$ (see Figure 4.7). The trend line of the drag coefficient using the linear viscous damping was above the measured results in the highest mean incident speed but was in better agreement for the lower two speeds of turbulent channel flow over the KC range 0.25–0.5.

The added mass remained close to zero across the studied flow conditions, $C_{\mathrm{a}} \approx$ -0.3 to 0.2. The negative values may have been due to the calculation method and the low inertia relative to the damping force.

The Morison force (Eq. 4.9) was found suitable for the range of KC<0.65 defined with amplitudes of streamwise velocities, $\|\dot{x}\|$, less than 0.5 times the mean flow, u_0. For this range, the magnitude of drag coefficient of the rotor in the turbulent flows was similar to a porous disc that produces similar thrust coefficient in steady flows. The difference between the drag coefficient for rotor and disc scattered at the range of $KC < 0.65$ was approx. 12.5%. The discrepancy of results was due to the approximation of the non-linear velocity and the neglected terms in the full Morison force (Eq. 2.39).

It can be inferred from Eq. 4.9 that at higher values of velocity ratios, $\|\dot{x}\|/u_0$>0.5, the influence of hydrodynamic forces over the mean current is greater and thus force assumption would be less accurate at velocity ratios approaching the unity. Increasing further the turbulence intensity would also cause variation of the drag coefficients due to the neglected terms of turbulent fluctuations ($F_{\mathrm{neglected,2}}$, see Eq. 4.8) that would become relevant for small velocity ratios, $\frac{\|\dot{x}\|}{u_0} \ll 0.5$.

For the rotor, differences in thrust coefficients would be expected with change of onset flow speed since a constant retarding torque is applied. As onset flow changes, rotational speed, flow relative to the foil and resultant lift and drag of the foil also change. For the rotor studied lift and drag may also vary with Reynolds number over the range of onset velocities considered. However, the thrust coefficient of the rotor varies by less than 5% over a range of tip-speed-ratios 4-6. A full-scale rotor would be a different geometry to develop the same variation of the scaled rotor thrust coefficient with tip-speed ratio. Similarly a full-scale disc of different geometry may develop the same thrust coefficient since the contribution of viscous effects may differ.

The drag of the scaled disc would be only different to a full-scale rotor if the viscous effects of the porous disc in the same flow speeds cause a different drag and thrust coefficient. Therefore, if the thrust coefficient of the disc is representative of the thrust coefficient of the full-scale rotor, in the range of most onset flow speeds of interest. Then the drag coefficient between the full-scale rotor and the equivalent disc would be the same. The added mass for both disc and rotor has been measured small relative to the drag force and its contribution can be neglected.

4.7 Extreme loads on Oscillating Rotors in Turbulent Channel Flow

An extreme prediction method is evaluated against rotor measurements due to forced axial motion with high frequencies (0.7 Hz) against mean flow at highest speed with turbulence. The methodology of Section 3.4 is applied to the thrust measurements to obtain the magnitudes exceeded in 1 in a 100, 1 in a 1000, and 1 in a 10000 samples with the Type 1 Pareto method. The extreme-value analysis was applied to samples of 420 s duration. The range of tests represents large amplitudes of streamwise velocities up to 60% of the mean flow. This numerical approach consisted in using the findings of Eq. 4.9, for the determination of the peak forces such that the measured force is approximated by:

$$F_{\mathrm{m}} \approx F_0 + F' + F_{\mathrm{osc}} \qquad \text{Eq. 4.10}$$

The extreme force on the rotor was calculated as the sum of peak forces resulting from each component in Eq. 4.10. These values were then divided by the mean thrust $(\bar{F})$ acquired in the forced streamwise motions with the incident flow. It is:

$$\frac{F_{\frac{1}{\mathrm{n}}}}{\bar{F}} = \left[\frac{F_0 + F'_{\frac{1}{\mathrm{n}}}}{\bar{F}}\right] + \left[\frac{F_{\mathrm{osc,max}}}{\bar{F}}\right] \qquad \text{Eq. 4.11}$$

In Eq. 4.11, the first term denotes the force with probability of occurrence, $F_0 + F'_{\frac{1}{\mathrm{n}}}$, for a rotor operating in turbulent flow with no streamwise oscillation, whilst the second term corresponds to the maximum force due to the relative axial motion between the rotor and the water. The second force is modelled from Eq. 4.9 as:

$$F_{\mathrm{osc}} = -\frac{1}{2}\rho A C_{\mathrm{D}} \dot{x} |u_0 - \dot{x}| \qquad \text{Eq. 4.12}$$

From Eq. 4.12 the peak rotor force occurs at the highest amplitude of combined velocity from the streamwise motion and incident flow. It is:

$$F_{\mathrm{osc,max}} = \frac{1}{2}\rho A C_{\mathrm{D}} \|\dot{x}\| (u_0 + \|\dot{x}\|) \qquad \text{Eq. 4.13}$$

The variation of the time-average force in the operating flow was investigated for a small range of velocities limited to $\|\dot{x}\| \ll u_0$. For the given velocity range, the component of velocity in Eq. 4.12 is:

$$\dot{x}|u_0 - \dot{x}| = \dot{x}u_0 - \dot{x}^2 = \|\dot{x}\| \cos(\omega t) u_0 - \|\dot{x}\|^2 \cos^2(\omega t) \qquad \text{Eq. 4.14}$$

Therefore, averaging these components for a complete period:

$$\frac{1}{\mathrm{T}} \int_{-\mathrm{T}/2}^{\mathrm{T}/2} \cos(\omega t) \mathrm{dt} = 0 \quad \text{and} \; \frac{1}{T} \int_{-\mathrm{T}/2}^{\mathrm{T}/2} \cos^2(\omega t) \mathrm{dt} = \frac{1}{2} \qquad \text{Eq. 4.15}$$

and substituting them into the components of the oscillatory force (Eq. 4.14). The mean of the combined force from current and streamwise oscillation using the modified Morison equation (Eq. 4.10) becomes:

$$\bar{F} = F_0 + \frac{1}{4} \rho A C_{\mathrm{D}} \|\dot{x}\|^2 \qquad \text{Eq. 4.16}$$

To verify the increase of mean thrust with velocity ratio, $\|\dot{x}\|/u_0$, the thrust coefficients measured in the three mean flows with turbulence present were compared with predictions using Eq. 4.16. The thrust and drag coefficient employed for simulations accounting the current and streamwise oscillations corresponded to 0.89 and 2 respectively. It was observed that the thrust for the disc remained similar to the rotor in three current flows and for both rotor and disc, the mean thrust coefficient tended to increase with velocity ratio (Figure 4.8). Predictions of increase of thrust were found reasonable for the three mean flows with velocity ratios less than 0.5. A discrepancy was observed in higher amplitude of motion and low incident flow speeds due to the lower accuracy of the Morison force. The high velocity ratio resulted in a over prediction of the mean thrust by Eq. 4.16.

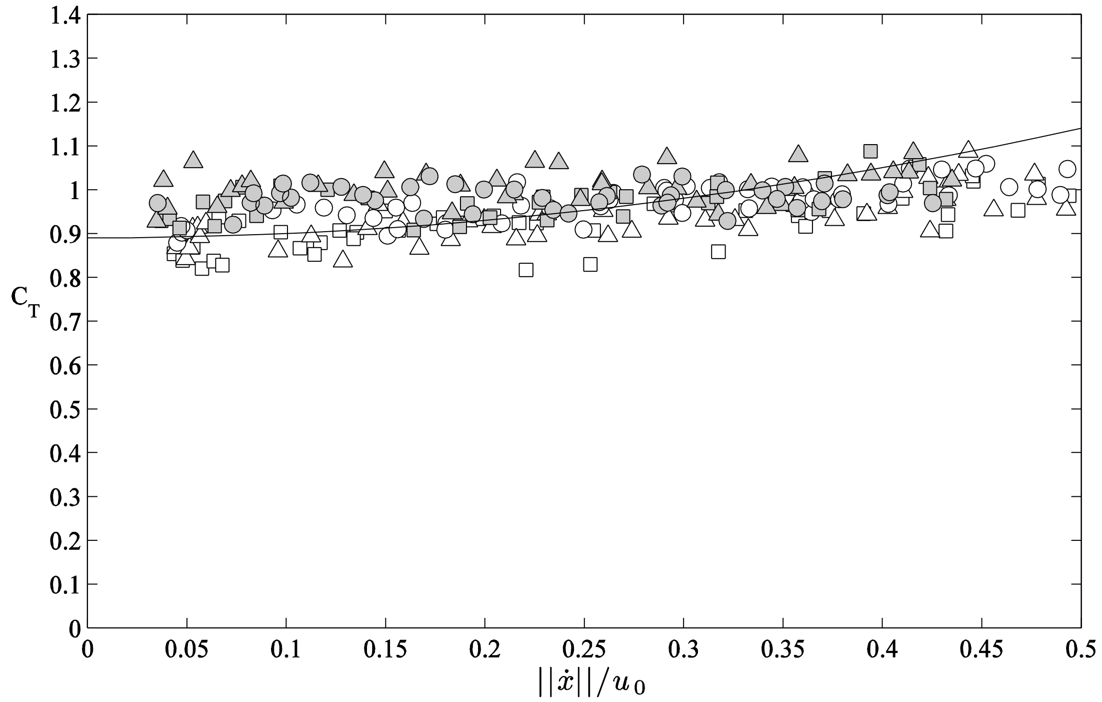

Figure 4.8 Mean thrust coefficient against velocity ratio for disc and rotor. Predictions using Eq. 4.16 (—). Markers of measurements as Figure 4.7.

After substituting the force terms from Eq. 4.13 and Eq. 4.16 into Eq. 4.11, the extreme force is:

$$\frac{F_{\frac{1}{n}}}{\overline{F}} = \frac{F_0 + F'_{\frac{1}{n}} + \frac{1}{2}\rho A C_D \|\dot{x}\|(u_0 + \|\dot{x}\|)}{F_0 + \frac{1}{4}\rho A C_D \|\dot{x}\|^2} \qquad \text{Eq. 4.17}$$

The statistical influence of the turbulent fluctuations was obtained from rotor measurements in turbulent flow without streamwise oscillations. The oscillatory force was specified for the range of rotor surge oscillations with velocity ratios of $\frac{\|\dot{x}\|}{u_0}$ =0–0.85 by using C_D ≈2 for 0.25<KC<1. This range was selected to investigate the trend of peak thrusts with increased streamwise velocity, extending beyond the range of conditions studied experimentally for either rotor or disc. The predictions of force are in good agreement (within 15%) with the measurements of the rotor operating in an incident flow with turbulence present and without oscillation in the streamwise direction.

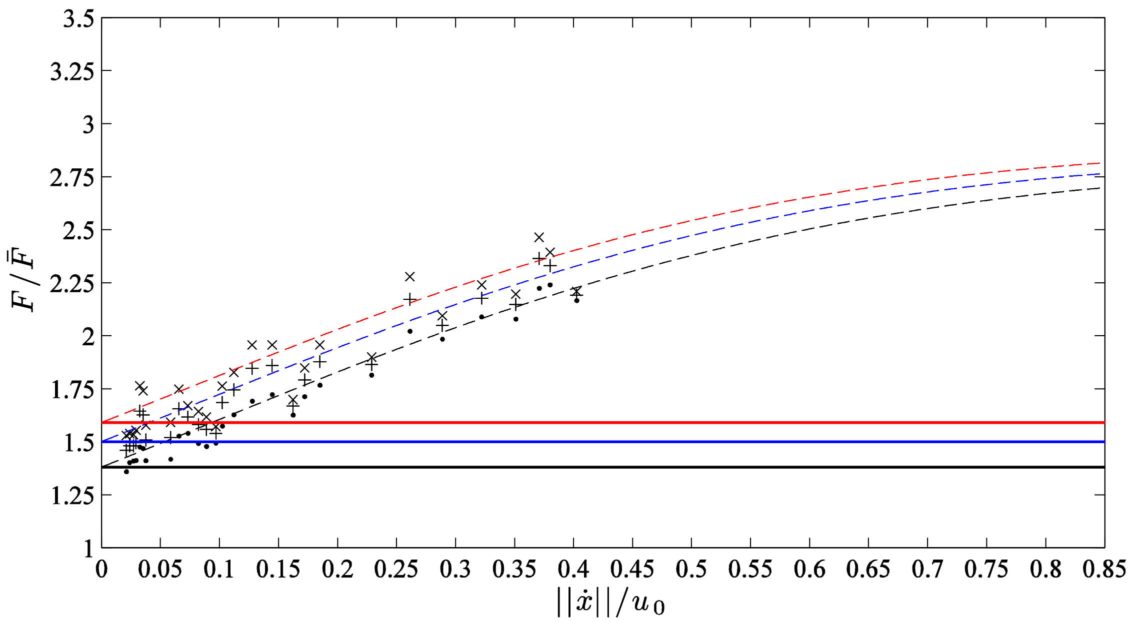

Figure 4.9 Predictions of the exceedance loads 1% (--), 0.1% (--) and 0.01 % (--) using an oscillatory drag coefficient of 2 against measurements of rotor undergoing streamwise oscillations in a mean flow with TI =12%. The 1-minute measurements of the 1% (●), 0.1% (+) and 0.01% (X) rotor forces are also shown against the 1% (-), 0.1% (-) and 0.01% (-) rotor loads obtained in a turbulent flow without streamwise oscillation.

From Eq. 4.17 and its derivative in respect to the streamwise velocity, the extreme force increases from the values obtained due to turbulent channel flow only and tend to a limit as the amplitude of the imposed streamwise oscillation approaches the incident flow velocity (Figure 4.9). However, increasing the amplitude of oscillation further would cause the minimum incident velocity to approach zero leading to stalling of the rotor. The latter effect, resulting from the high angles of attack in which the blades operate, due to the relatively low speed acquired between the rotor motion and the water. The rotor loading was predicted well in the studied range using the Morison force of Eq. 4.11.

4.8 Summary

Measurements of added mass and drag coefficients were compared for a rotor and a porous disc subject to forced oscillation in steady flow. The disc porosity was selected such that the rotor and disc developed similar thrust coefficient in steady flow. The time-varying force and displacement were obtained with a dynamic structure for both a rotor and disc in turbulent flow of three different mean speeds and for the disc only undergoing oscillation in a quiescent flow. The added mass and damping were made non-dimensional by the mass of a spheroid. The variation of linear damping (Eq. 4.5) and Morison type drag variation (Eq. 2.39) with Keulegan Carpenter number was studied and its effect with small range of frequency number (Stokes parameter) was shown to be small.

For both a 3-bladed rotor and a porous disc that develops equivalent mean thrust, the added mass due to oscillation in quiescent flow was approximately 12% of the mass of a spheroid. Damping coefficient was a linear function of Keulegan Carpenter number for $KC < 2$ and variation of this relationship with frequency number was less than 6% (Figure 4.4). The oscillatory drag coefficient exhibited an exponential constant decay form to a limiting value of 2 (Figure 4.5). This magnitude was found to be within the range of oscillatory drag coefficients of 1.8-2.4 reported for a rotor undergoing streamwise motion in steady flows which was described using an equivalent form of Morison equation (Whelan et al., 2009b). The measured force in turbulent channel flows was studied with a drag term using the Morison equation (Eq. 4.9). This approach consisted in summing the force obtained on the rotor, when supported on a stiff tower in a turbulent channel flow, with an oscillatory force using an oscillatory drag coefficient based on the streamwise oscillation. Good agreement of drag coefficient was obtained in the three turbulent channel flows between disc and rotor in the studied range of velocities and amplitude of forced axial oscillations. The inertia of the rotor and disc was found to be negligible in the turbulent channel flows. The mean thrust coefficient increased with velocity ratio $\|\dot{x}\|/u_0$, but remained close to the rotor thrust in turbulent channel flow over the range $\|\dot{x}\| < u_0/2$.

A reasonable approximation to the time-varying force on a rotor undergoing forced oscillation in turbulent channel flow is obtained by summing the force of the rotor, when supported in a stiff tower in turbulent channel flow, with a Morison type drag force (Eq. 4.10) defined by the product of velocity amplitude and the maximum velocity,

$\|\dot{x}\|(u_0 + \|\dot{x}\|)$, and using a drag coefficient of approximately 2. This method was used to assess the influence of the rotor oscillation amplitude on extreme forces due to imposed oscillation within a turbulent channel flow. Rotor forces with 1 in 100, 1 in a 1000 and 1 in a 10000 probability of exceedance were shown to increase with amplitude of streamwise velocity, with good agreement with measurements over the range $\|\dot{x}\| < u_0/2$ and asymptoting to a limit at higher values of oscillation amplitude.

CHAPTER 5: LOADING DUE TO WAVES COMBINED WITH TURBULENT CHANNEL FLOW

The loading experienced by a turbine undergoing forced oscillation in turbulent channel flow provides some insight into the loading of a turbine subject to waves when operating in a mean flow with turbulence present. These flows differ due to the depth variation of velocity and the time variation of dynamic pressure within waves. However, these flows are analogous for waves of small amplitude and long period. Experiments are conducted with waves opposing a turbulent channel flow to evaluate the suitability of the drag and inertia terms obtained in the preceding section for predicting loading due to these combined flows. Comparison is also drawn to the extreme forces predicted using the methods evaluated in earlier chapters.

5.1 Introduction

For shallow and intermediate waters, rigid-bed-connected and gravity structures have been utilised to support wind turbines. Turbines are currently being developed for electricity generation from tidal streams and rely on similar structural approaches. These devices are usually designed to operate continuously and implement protective procedures such as turbine shutdown and retrieval procedures in the presence of an extreme wave condition. The rotor loading in such flow conditions is relevant to the design of cost-effective support structures.

In this chapter, an extreme-value analysis is applied to the thrust developed on a tidal stream rotor due to a turbulent and oscillatory flow. The variation of extreme rotor force with wave height is studied using a Morison force equation based on the approach evaluated for oscillation in turbulent flow in earlier chapters. The variation of thrust with Tip-Speed Ratio of the rotor is comparable to a full-scale turbine.

5.2 Experimental Measurement

Experiments are performed in a turbulent channel flow of $TI = 12\%$ with co-generation of eighteen wave conditions to obtain the time variation of the rotor thrust. The rotor and equipment employed, along with a description and methodology of the flume, recordings of the flow kinematics, axial force and rotor's rotational speed is explained in Section 3.2. The mean flow velocity, water depth and configuration of the rotor and support structure in the wave conditions are all comparable to the turbulent channel-flow tests. Opposing waves are specified with amplitudes [10-20] mm and frequencies [0.5-1] Hz by piston-type wave paddles located 12.5 m from the inflow and 6.5 m from the rotor. The surface elevation, $\eta(t)$, is recorded with a pair of wave probes located at the mid X-Y plane of the channel flume, each 1 m apart from the rotor axis (Figure 5.1). For all tests, the motor torque was specified such that the mean Tip-Speed Ratio, TSR, was 5.5 ±6%. For this Tip-Speed Ratio range, the mean thrust coefficients obtained from recordings and predictions using the BEM were 0.91 ±7% and 0.84-0.86. Time-varying parameters were recorded at 200 Hz for a 60 s interval. Measurements were repeated 44 times for each oscillatory flow.

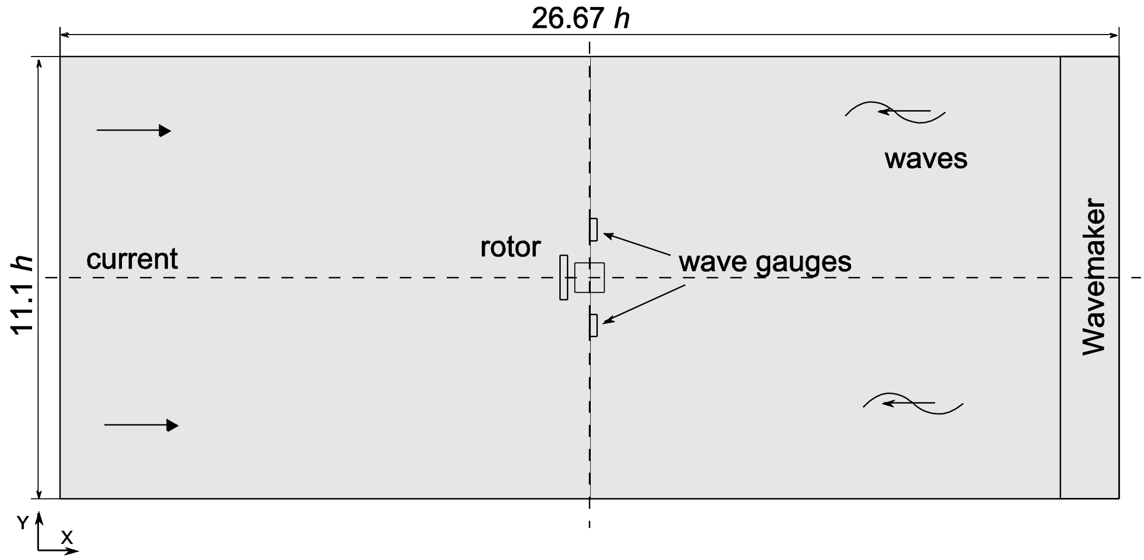

Figure 5.1 Experimental arrangement for the sea states conditions. Waves are generated at the right opposing the turbulent current flow. Rotor installed at mid depth with a pair of wave probes recording the surface elevations.

5.3 Variation of Extreme Loads with Wave Height

The measured force is analysed to determine the force exceeded by 1%, 0.1% and 0.01% of samples. Extreme value anlaysis methods of Chapter 2 are evaluated for all wave conditions such that the extreme values obtained with different sample durations and threshold magnitudes were within 3% of those obtained employing 44 minutes of continuous thrust data. A threshold force of 1.25 times the mean force and 10 min sample length was found to provide reasonable convergence of extremes. Higher values of threshold values gave similar extreme results, but required larger samples. In Figure 5.2, the sensitivity of the threshold against the sample duration is depicted for a wave condition of a specified frequency 0.6 Hz and amplitude 10 mm. The return period of the 0.01% represented the force likely to occur in a full-scale turbine at long-run average intervals of 48 hours during continuous rotor operation in the same flow. From recordings of wave-gauge monitors, statistical heights and elevations ($H \approx 2\sqrt{2}\eta_{\mathrm{rms}}$) were utilised to contrast the extreme loads acquired at the eighteen oscillatory flows. The highest studied flow condition represented a wave height of approximately 10 m in a full-scale turbine. Additionally, the measurements for the combined flow were compared to the turbulent channel flow only (TI =12%).

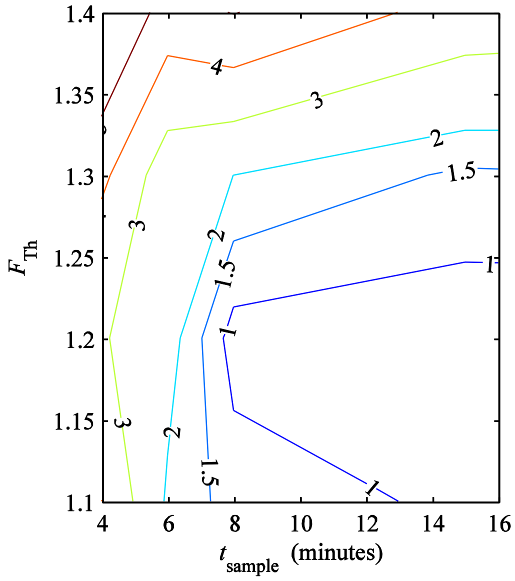

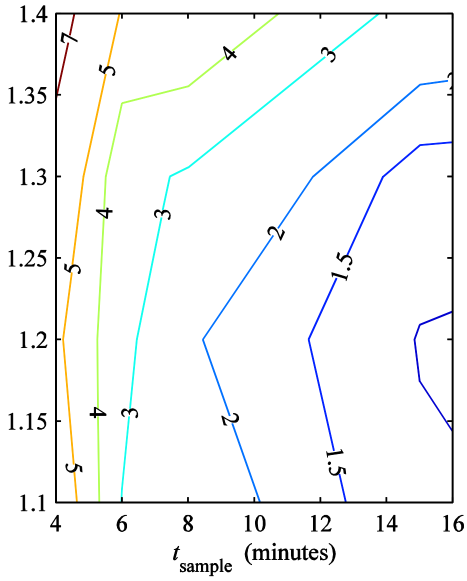

Figure 5.2 Difference in percentage of the 1% (left) and 0.1% (right) loads obtained with different threshold forces and sample lengths based on the continuous 44 minutes of data for waves specified with 0.6 Hz and amplitude of 10 mm opposing a mean flow with turbulence present (TI =12%).

The extreme thrust in the combined flows exhibited an approximately quadratic increase with the amplitude of the wave. Waves specified with frequencies greater than 0.9 Hz did not propagate to the rotor due to their small velocity relative to the current and so the extreme thrust experienced remained similar to the turbulent channel flow only.

The flow with wavelength $3.16h$ (h=water depth) and amplitude $0.12h$ provided the highest 1% thrust with a magnitude of 220% of the mean force in the turbulent channel flow only. The spectrum of force in the combined flow for a small height regular wave was studied and compared to the force imposed in a turbulent channel flow only. The spectrum in the combined flow exhibited a comparable behaviour to linear sum of the spectrum of force in turbulent channel flow with the narrow-band force spectrum that is associated with the wave frequency (shown in Figure 5.3). Dominant frequencies in the oscillatory flow corresponded to the specified wave frequency, $f_{\text{wave}} = 0.6$ Hz, natural frequency of the device, f_{n}, the mean rotational speed $f_{\text{r}} = \frac{\omega}{2\pi}$, and a harmonic of the rotational speed, $3f_{\text{r}}$, corresponding to the blade-passing frequency.

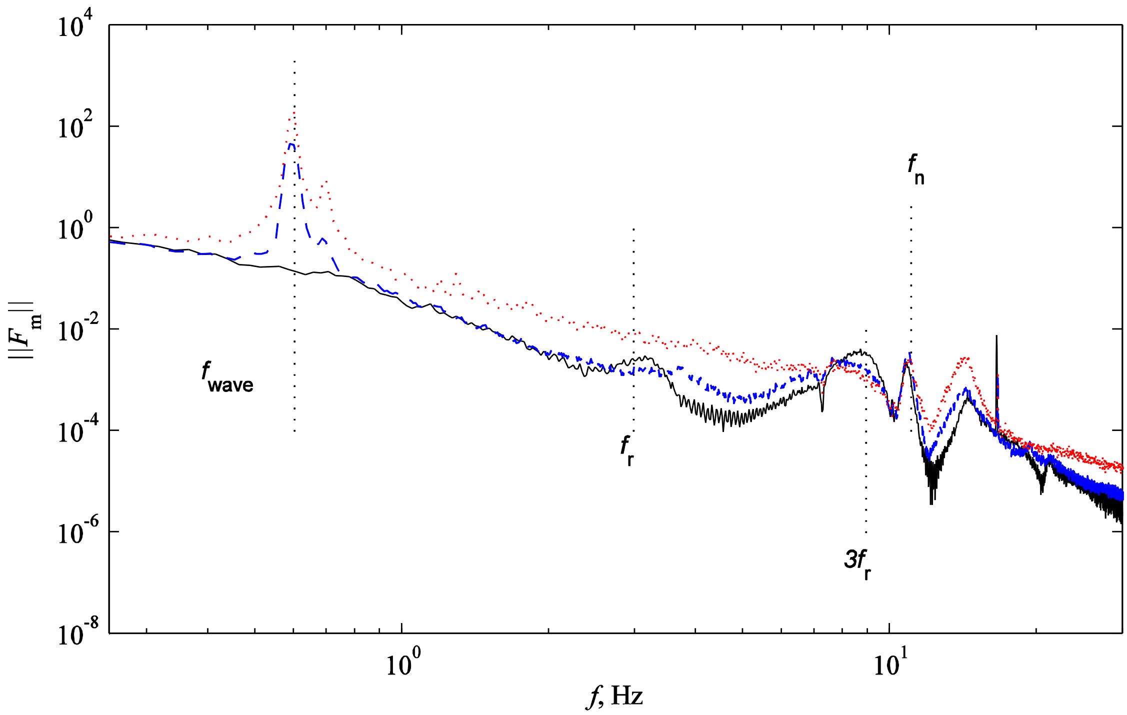

Figure 5.3 Force spectra for flow conditions without waves (-) and with waves of low (--) and high amplitude of elevation (--). Peak frequencies correspond to the wave, f_{wave}, mean rotational speed, f_{r}, third rotational harmonics, $3f_{\text{r}}$, and support natural frequency, f_{n}.

For conditions of wave heights above $0.26h$, the extracted power of the rotor was low due to the high fluctuations of the incident flow velocity. For these wave conditions, the thrust spectra exhibited a partial combination of forces due to overlapping of the amplitude spectrum of the wave velocity with the ambient flow (Figure 5.3). This produced a quadratic increase of the extreme thrust with the wave height, but to an initial force lower than obtained in a turbulent flow without waves (see Figure 5.4). In practice, turbines are likely to be shut down in the given flow conditions and so drag on the stationary rotor and structure would be considered rather than thrust on the rotor. However, this case was investigated to provide insight of extreme loads in a possible operating condition.

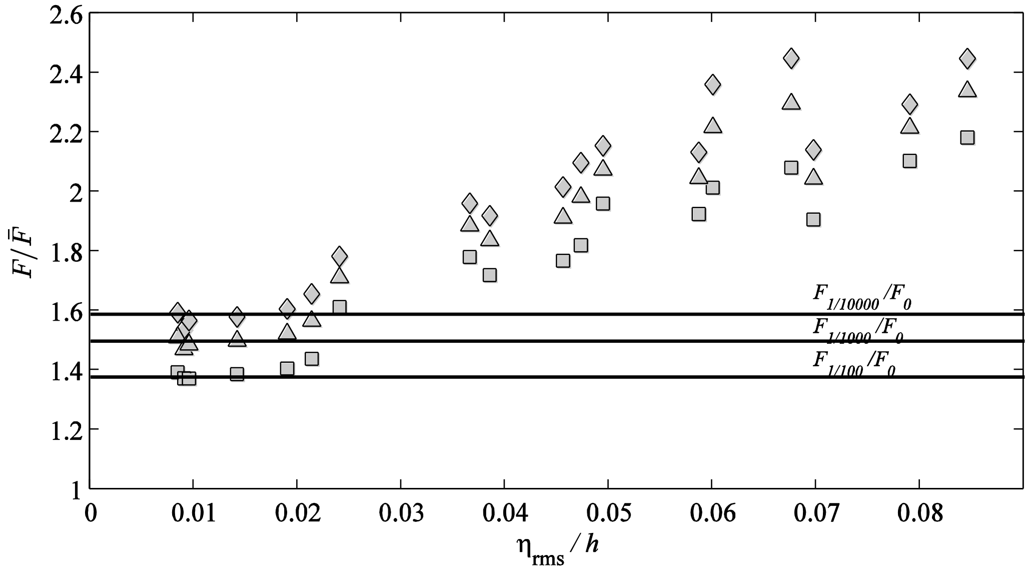

Figure 5.4 The extreme load variation from the measured time-varying force compared with the statistics of the surface elevations. The 1% (■), 0.1% (▲) and 0.01% (♦) rotor forces obtained in oscillatory flows due to a current opposing waves against the extremes in flow of TI =12% (─) without waves.

The statistics of the wave heights and forces obtained in the eighteen oscillatory flows are summarised in Appendix B.

5.4 Extreme Loads due to Turbulent Channel Flow with Waves: Drag Prediction

The Morison equation is an approach regularly used to analyse the forces occurring on bluff bodies due to sinusoidal time-varying flows. The full Morison force is expressed as $F_{\mathrm{m}} = \frac{1}{2}\rho A C_{\mathrm{D}}(U_{\mathrm{a}} - \dot{x})|U_{\mathrm{a}} - \dot{x}| + \rho V C_{\mathrm{a}}(\dot{U}_{\mathrm{a}} - \ddot{x}) + \rho V \dot{U}_{\mathrm{a}}$ where $A, U_{\mathrm{a}}, x, V, C_{\mathrm{a}}$ and C_{D} denote the swept area, incident velocity, body motion, volume, the added mass and drag coefficient of the body respectively (see Section 2.12). However, other alternative forms of the Morison equation exist and have been addressed as more appropriate for the wave loading on porous objects, which are representative of offshore jacket structures and scaled tidal stream turbines (Whelan et al., 2009b; Taylor et al., 2013).

The loading on the rotor in turbulent channel flows combined with waves is investigated on the basis of the extreme values of thrust, both measured and predicted, based on the wave-induced hub-height velocity predicted assuming linear wave theory. The force is given analagous to the Verley and Moe's (1979) formula (see Eq. 2.48) by summing the force due to the turbulent channel flow with an oscillatory force due to the wave component of velocity only. The oscillatory thrust is expressed with a drag coefficient of unknown magnitude, $C_{\mathrm{D,wave}}$, kinematics of the mean flow with turbulence present, u_{c}, and a thrust coefficient based on the turbulent channel flow, C_{T} =0.89. The inertia of the rotor is assumed to be small and is thus neglected. The force is:

$$F \approx F_{\mathrm{turb}} + F_{\mathrm{p,wave}} \approx \frac{1}{2}\rho A C_{\mathrm{T}} {u_{\mathrm{c}}}^2 + \frac{1}{2}\rho A C_{\mathrm{D,wave}} u_{\mathrm{wave}} |u_{\mathrm{wave}}| \qquad \text{Eq. 5.1}$$

For this method, the extreme force in the combined flow is due to the statistics of the measured force in a turbulent flow, which are then added to the maximum force due to the presence of the waves. The maximum thrust due to the wave kinematics only is obtained as:

$$F_{\frac{1}{n},\mathrm{wave}} = \frac{1}{2}\rho C_{\mathrm{D,wave}} \pi R^2 \|u_{\mathrm{wave}}\|^2 \qquad \text{Eq. 5.2}$$

where R denotes the rotor radius and u_{wave} is the amplitude of the wave velocity at the hub height obtained from measurements ($u_{\mathrm{wave,m}}$) or predictions ($u_{\mathrm{wave,p}}$) of the combined current and wave flow.

The wave velocity is predicted using linear wave theory and measurements of the surface elevations in the combined flow. The oscillatory flow is modelled as opposing waves propagating parallel to a mean flow of constant velocity (U_0) assumed constant over the depth. Wave breaking, reflection and non-linearities are neglected. The horizontal velocity for the oscillatory flow is expressed as (Phillips, 1977; Dean and Dalrymple, 1991):

$$u_{\mathrm{wave,p}} = \frac{(\omega - k u_0) A_{\mathrm{wave}} \cosh\big(k(z+h)\big) \cos(kx - \omega t)}{\sinh(kh)} \qquad \text{Eq. 5.3}$$

The variable z represents the distance from the mean free surface (+ve upward), h represents the water depth and A_{wave} the surface wave amplitude. The angular frequency, ω, is estimated with the Doppler effect:

$$\omega = U_0 k + \sqrt{gk \tanh kh} \quad \text{Eq. 5.4}$$

where g is the gravity constant and k is the wave number obtained relative to a reference frame moving with the mean flow speed. The amplitude of the wave height is estimated from the peak amplitude of the spectra measurements of the surface elevations. Wave conditions in which breaking waves occurred were not considered. The assumed wave height range is $\frac{\|\eta\|}{h}$<0.05. This linear prediction was in good agreement with measured kinematics at hub height, to within 7% for the small amplitude waves considered in the extreme force analysis (Figure 5.5).

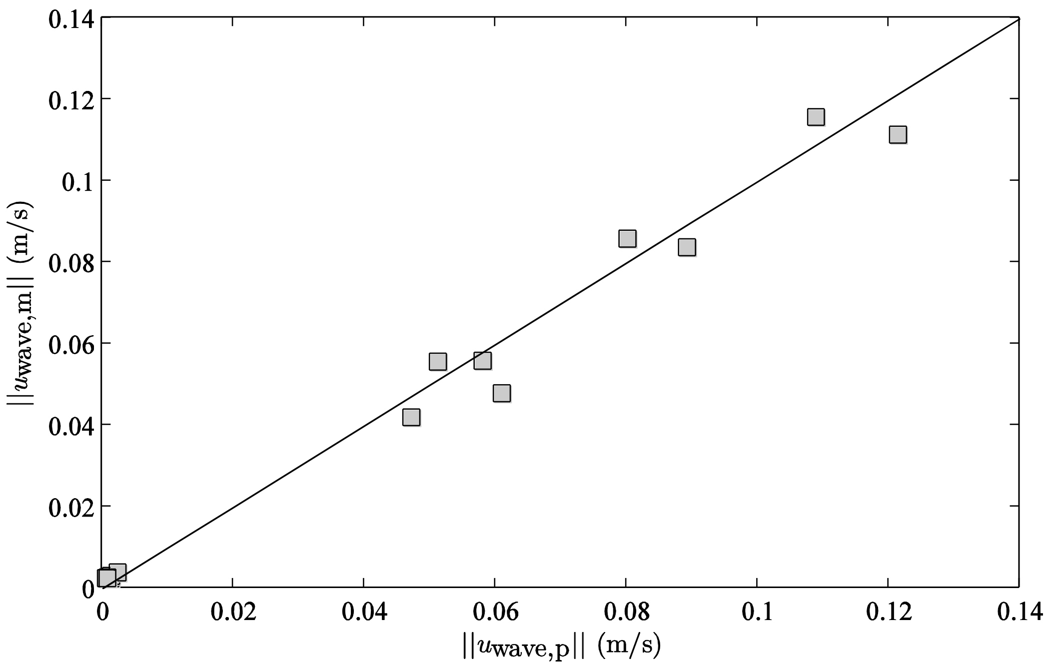

Figure 5.5 Comparison of the measured and predicted amplitude of wave velocity at the hub height (■) using linear wave theory and measurements of the surface elevations.

Subsequently, the drag coefficient was determined using Eq. 5.2 with the predicted amplitude of the wave-hub velocity, as a best-fit approach of the measurements of extreme rotor force in the combined flow (Figure 5.4). For this method, a drag coefficient, $C_{\mathrm{D,wave}} = 11$ provided the 1%, 0.1% and 0.01% and steady flow thrust coefficient of 0.89 provided forces to within 8%. The uncertainty of the drag coefficient due to discrepancy of predicted hub velocities against kinematic measurements (7%) was also considered. For this purpose, Figure 5.6 depicts the uncertainty of the peak thrusts with velocity magnitude (smaller markers) and contrasts this with the extreme force simulations accounting for velocity variation (using Eq. 5.2). This approach provided different fitted drag coefficients (shown in bands) and the mean of these lines remained with a value of 11.

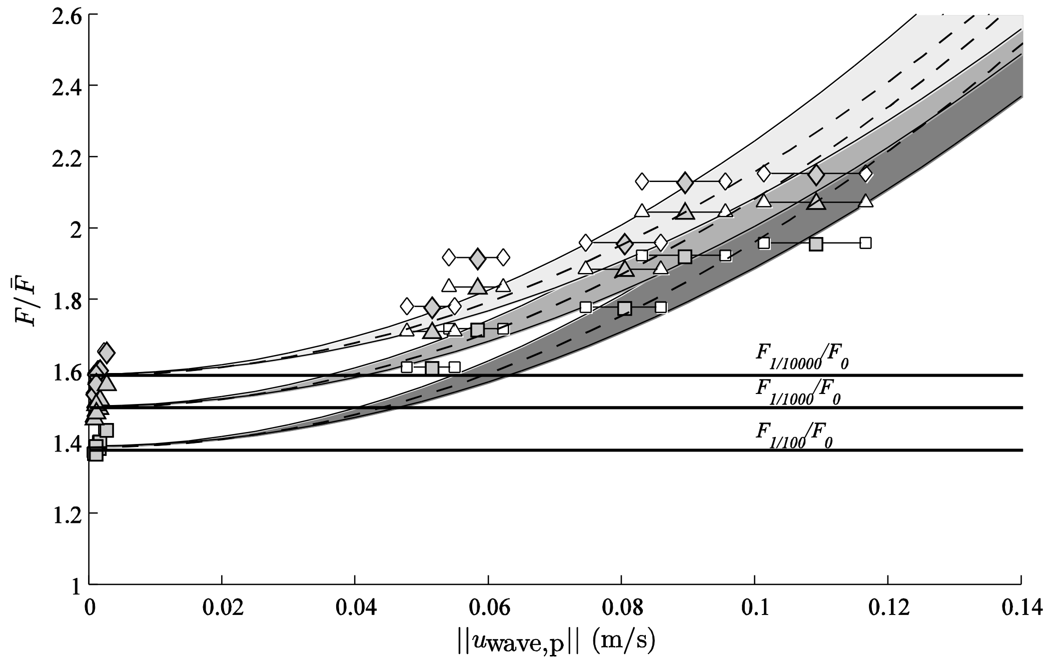

Figure 5.6 The measured exceedance forces in waves with probabilities of 1% (■), 0.1% (▲) and 0.01% (♦) and same forces (□, Δ, ◊) due to uncertainty of the wave velocities ±7%. Simulations are shown using wave kinematics with a drag coefficient of 11 (--) and a range of drags accounting for velocity variation of 7% (█). Extreme loading in turbulent channel flow of $TI = 12\%$ (—) is also compared.

5.5 Time-varying Kinematics and Drag due to Waves and Turbulence

The loading on a rotor is known to be dependent on the pressure drop across the rotor and this is dependent on the flow characteristics occurring along the rotor's blades and downstream. Unsteadiness in an onset flow for a tidal stream turbine is due to several processes and these result in unsteady loads. Waves alone impose dynamic wave pressures and accelerations both varying in time and space whilst the current alone may contain depth variation of flow and high-frequency fluctuations due to turbulence (McCann et al., 2006). Although several studies have assumed minimal interactions on the average thrust imposed on a rotor in uniform flow and combined uniform flow with waves, little has been done on the interactions of the extreme rotor loads due to the waves. In this section, the forcing in waves combined with turbulent channel flows is investigated in an analogous manner to the loading on a rotor undergoing forced streamwise oscillations in turbulent channel flows (Chapter 4). This approach suggests that the rotor's response in waves combined with turbulent flows is approximately given as the sum of a thrust in ambient flow and a drag due to the relative wave velocity predicted at the hub height. However, for flows combined with waves, the wave velocity over the channel depth decays in proportion to the height and frequency of the surface wave. This effect of varying velocity over the rotor is not considered. Therefore, for the wave conditions with small wave heights and wave numbers, such as $kh \rightarrow< \pi/10$ (see Eq. 5.3), the thrust assumption may be found acceptable.

Time varying force due to waves with turbulent flow is modelled using the Morison force described in Section 4.6, by replacing the axial motion of the rotor with the wave-induced component. To evaluate its suitability against rotor measurements in waves and thus compare the oscillatory drag with the findings of using Eq. 5.2. The thrust due to wave kinematics, F_{osc}, is extracted from the measurements using the band-pass filter techniques of Section 4.6. The added mass of the rotor and support is ignored.

The wave kinematics are predicted with the linear wave theory as explained in Section 5.4 and the drag force due to relative wave velocity becomes:

$$\frac{1}{2}\rho A C_{\mathrm{D,wave}} u_{\mathrm{wave,p}} |u_0 - u_{\mathrm{wave,p}}| = F_{\mathrm{osc,p}} \qquad \text{Eq. 5.5}$$

The magnitude of the drag coefficient for small wave conditions is obtained as the least-squares fitting of Eq. 5.5 with the measured wave force, F_{osc}. The comparison between measurements and simulations using this approach for a wave condition is shown in Figure 5.7.

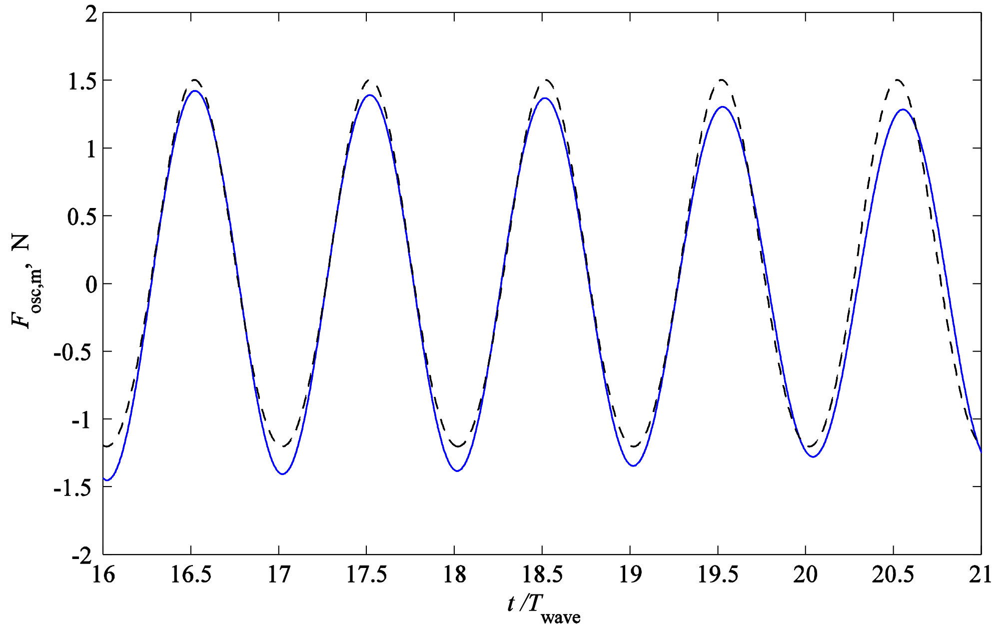

Figure 5.7 Time-varying force due to waves against predictions employing linear wave kinematics at the hub height. --, predictions;—, measurements.

Drag coefficients with the least square fit residuals above 0.9 were selected and plotted against the operating KC, based on the frequency and amplitude of the wave velocity at the hub height (Figure 5.8). The wave loading in turbulent channel flows produced time-varying forces and oscillatory drag coefficients of 2 with standard deviation of 0.0805. These values were comparable to a rotor subjected to streamwise oscillations in a flow of the same TI =12% with drag coefficients tending to a magnitude of 2 with increasing KC number (shown in Section 4.5). The flows were concluded to be analogous.

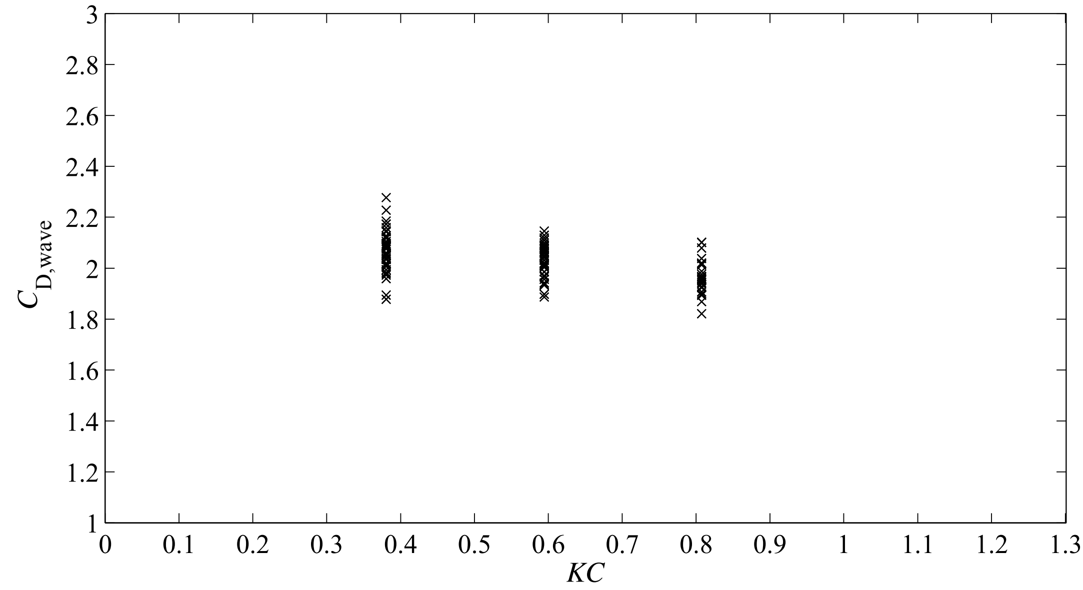

Figure 5.8 The oscillatory drag (X) of a rotor on a fixed support structure in turbulent channel flow with opposing waves. KC based on hub-height velocity predicted by linear theory from measured wave height.

5.6 Prediction of Extreme Loads based on Forced Streamwise Oscillations of the Rotor in a Turbulent Channel Flow

The prediction method of extreme force described in Section 4.7 for a rotor subjected to streamwise oscillation is evaluated against the loading for a rotor in waves opposing a turbulent channel flow without forced streamwise oscillations. This approach shows that the force distribution due to streamwise oscillation in turbulent channel flow is approximately due to the peak thrust based in mean flow with turbulence present, which is then added to the maximum value of the wave-induced drag, F_{osc}, defined by relative velocity and using a mean oscillatory drag, C_{D} =2, for the amplitudes of surge oscillation given in the KC range 0 to 1. The extreme force, quantified in proportion of the mean thrust of the combined flow, becomes:

$$F_{\frac{1}{\text{n}}} = \left[\frac{F_0 + F'_{\frac{1}{\text{n}}}}{\bar{F}}\right] + \left[\frac{F_{\text{osc,max}}}{\bar{F}}\right] \quad \text{Eq. 5.6}$$

Here $F'_{\frac{1}{\text{n}}}$ is the peak force measured due to turbulent channel flow only and $F_{\text{osc,max}}$ is by Eq. 5.5. The 1%, 0.1% and 0.01% predicted forces with this method were compared against measurements of extreme thrust in turbulent channel flow combined with wave and turbulent channel flow only (Figure 5.9). The curves of the peak loading departed from the statistical forces in the turbulent channel flow and headed towards a horizontal limit as the wave velocity amplitude approached the mean incident speed (as shown in Figure 4.9). The rotor loading was predicted well with the Morison approach using an oscillatory drag coefficient of 2 for the time-varying force and a thrust coefficient of 0.89 for the mean force. The discrepancy of results was only 5.6% employing velocity at the hub height with a discrepancy of 7%.

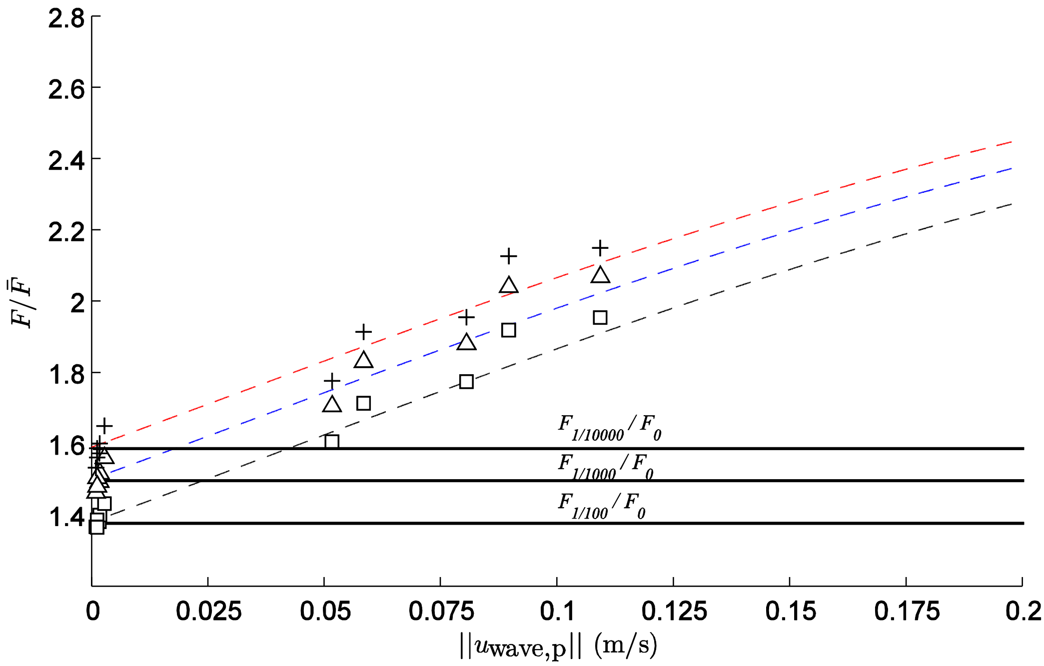

Figure 5.9 Predictions for the 1% (--), 0.1% (--) and 0.01% (--) wave forces using an oscillatory drag coefficient of 2 against measurements of a rotor supported on a stiff tower in a mean flow with TI =12% and opposing waves. Measurements of the 1% (□), 0.1% (Δ) and 0.01% (+) rotor wave forces against the exceedance loads in turbulent channel flow without waves (—).

5.7 Summary

.

A set of experiments was conducted to investigate the loading in representative tidal characteristics of turbulent channel flow with opposing regular waves. The mean thrust coefficient in the oscillatory flow conditions was found to be comparable to predictions in uniform flow using the BEM method. A Type 1 distribution method with a Pareto tail fitting technique was employed to determine the 1%, 0.1% and 0.01% rotor forces divided by their mean. These maximum forces were obtained with a peak-over-threshold technique. A threshold of 1.25 times the mean force was selected for all the turbulent wave conditions. For this approach, a 10-minute sample was required to ensure convergence of extremes within 3% of the values obtained from continuous 44 minutes data. The maximum 1% force was encountered with the wave frequency condition of 0.7 Hz and had a magnitude of approximately 220% of the mean force. The extreme loading in the combined flow showed an approximately quadratic growth with the amplitude of the wave velocity and as wave velocity decreased, the force approached to the condition in a mean flow with turbulence present only.

A drag term (Morison Eq.) was employed to investigate the rotor loading in turbulent channel flows with opposing waves. This method was based on the rotor tests undergoing streamwise oscillation in turbulent flow (Eq. 4.9), in which velocity of rotor was imposed by forced oscillation and the resultant force was predicted by summing the peak thrust due to turbulent channel flow with a maximum force defined by relative velocity due to the wave. The simulations of extreme loads employed a thrust coefficient of 0.89 for the turbulent channel flow and a drag coefficient of magnitude 2 for the wave condition. The extreme forces departed from the statistical turbulent forces and asymptote to a limit with increasing amplitudes of wave velocity. Extreme forces predicted using Eq. 5.6 were within 6% of measurements, within the uncertainty associated with the prediction of hub-height velocity from linear kinematics.

CHAPTER 6: SUPPORT-STRUCTURE DYNAMICS

In this chapter, the influence of support platform dynamic response on the loading of horizontal-axis turbines is investigated by time-domain solution of a one and two-degree-of-freedom coupled equation of motion. The particular interest is the influence of the support-structure dynamics on the response and extreme loads experienced by a tidal stream turbine when subjected to a combined turbulent channel flow with opposing waves. The intention is to identify support structure properties that reduce the variance and peak value of rotor thrust, to inform design optimisation of floating platforms.

Dynamic response is caused by wave forcing on the immersed part of the supporting platform and loading on the rotor. Forcing on the rotor is modelled following the approaches of Chapter 4 and 5. The onset velocity encountered by the turbine is time-varying due to a combination of mean flow, turbulence, waves and the support-structure motion. Response is modelled for two different systems: surge only and coupled surge and pitch. The single mode model provides identification of the properties of a supporting platform – specifically wave induced excitation force, radiation damping, stiffness and added mass – that would reduce peak force on the turbine in comparison to a rigid structure, such as a bed-connected support. The dynamic response for the coupled surge and pitch motion is applied to a typical semi-submersible structure. Hydrodynamic parameters for the support are obtained by linear diffraction theory. To assess benefits of the dynamic response, a comparison is made of the mean variance of thrust between the semi-submersible platform and a bed-mounted support in a wave condition representative of tidal stream sites.

6.1 Introduction

Many of the offshore wind and prototype tidal stream turbines that have been developed employ either gravity support systems or stiff bed-connected structures and have been located in shallow and intermediate water depths, typically less than 30 m. Exploitation of the deeper sites is the aim of many wind-farm projects (DEA/CADDET, 2000), but employing the conventional turbine supports is both impractical and expensive. Several floating moored systems have been proposed to support one or more turbines but these have not yet been widely deployed at offshore sites. For these platforms, the rotor may oscillate relative to a fixed reference due to mooring line deformation, excitation of the support structure by surface waves and excitation of the rotor by unsteady loads during operation. The reliability and design life of a turbine is dependent on the magnitude and frequency of occurrence of the loading experienced during the design life (McCann, 2007; Val et al., 2014). To inform design, it is important to predict dynamic response of the floating system with sufficient accuracy to ensure reliability, stability and safe keeping of the device. Several numerical tools accounting for rotor and support response are being evaluated to gain understanding of the complex, dynamic behaviour (Francis and Hamilton, 2007; Way et al., 2013; Van der Plas, 2014). The extent to which dynamic response may mitigate the peak loads experienced by a turbine during operation has not been documented and this is the aim of the present chapter.

6.2 Support Structures for Horizontal-Axis Wind and Tidal Stream Turbines at Shallow and Intermediate Water Depths

Wind turbines are a mature technology that has been widely deployed onshore and, particularly in Europe, at offshore locations. Compared to onshore, offshore sites offer greater resource (Troen and Petersen, 1989), more predictable winds, little visual impact and typically, the operating flows have lower levels of turbulence. The support structure is required to resist the thrust due to wind variation, the compression forces by turbine weight, and induced wave-current loads. Many of the offshore wind farms are located on sandbanks and so driven monopiles are commonly used. Alternatives include braced piles, tripods, suction caissons and heavy gravity foundations (Figure 6.1).

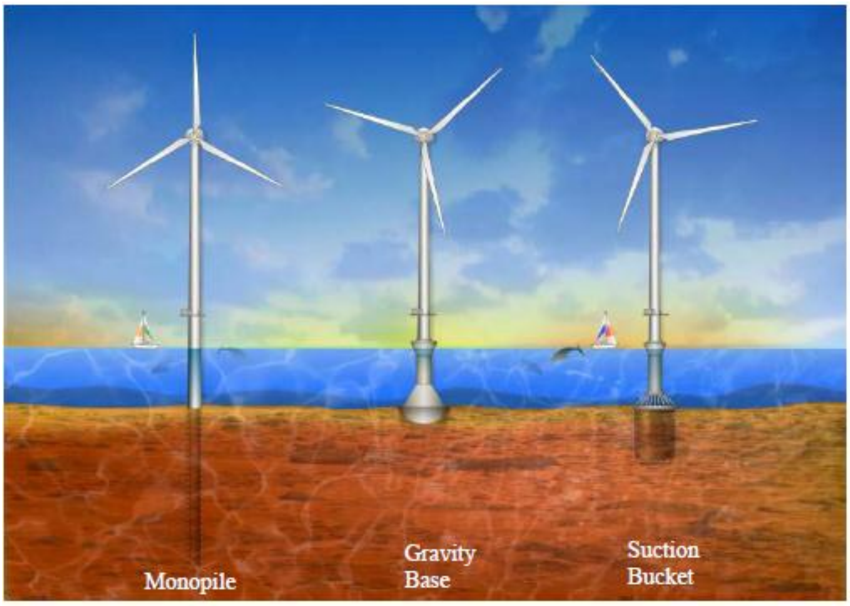

Figure 6.1 Different concepts of support structures for wind turbines deployed at shallow water depths. Source from Musial and Ram (2010).

Design and deployment of tidal stream turbines is largely based on the experience gained from development of wind turbines at offshore sites. The majority of the prototype systems currently in development are horizontal-axis turbines rigidly fixed to the seabed in a similar manner to wind turbines (Figure 6.2). Due to the speed of tidal streams, the bed material at tidal stream sites is often scoured rock. Therefore, braced monopiles or tripods are preferred. The magnitudes of rotor loading for wind and tidal turbines differ and so different support design criteria apply. Winter (2011) shows that the mean thrust on a tidal stream turbine rated at 1 MW is 6.4 times higher than that imposed on a wind turbine of the same rated power. Tidal turbine blades may thus be designed for higher ultimate and fatigue criteria than wind turbines.

It is not trivial to identify a single structure type that is most suitable for tidal devices, since total costs are determined by several aspects, such as the structure material and fabrication, as well as the costs of installation, maintenance and retrieval. Each support structure requires sufficient stability to counteract the wave-induced loading and the turbine cyclic thrusts. Orme and Masters (2006) compare six alternative support structure types for tidal stream turbines in terms of the system cost and benefit. For each system, the name and description is summarised as:

- Telescopic system - a tidal turbine mounted on a set of telescopic towers, which can be expanded or contracted to adjust the height.

- Guyed tower - a tidal turbine with a self-buoyant nacelle bounded by four chains attached to the sea floor.
- Top mounted - a tidal turbine supported on a fixed tower with the hub height at mid-depth (e.g. Figure 6.2b, Figure 6.2c).
- Shrouded concept - a tidal turbine inside a venturi-type duct.
- Sheath - a turbine supported on a tower where it can slide all the way upwards and downwards (e.g. Figure 6.2a).
- Anchored system - a tidal turbine chain anchored and kept in position with the nacelle's buoyancy.

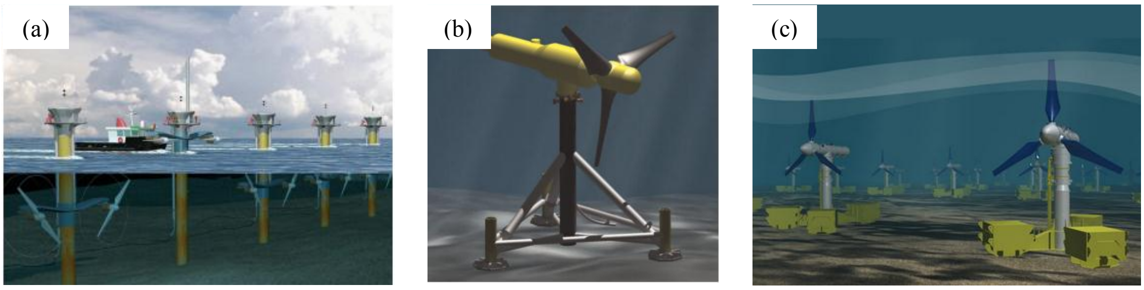

Figure 6.2 Concepts and illustrations of fixed supported configurations a) Marine Current Turbine (MCT Ltd) b) Alstom Tidal stream Turbine (Walker et al., 2013) c) a gravity based concept (Atlantis Resources Ltd).

A key factor affecting the total cost of bed-connected supporting structures is the cost of deployment since this is typically dependent on use of specialist vessels. Most bed-connected structures appear to be prohibitively expensive when deployed in deeper waters. In addition, the deployment of monopiles above 25 metres depth has not been proven to withstand the large moments and shear stresses that will be generated by the thrust imposed on a turbine (de Vries and Krolis, 2007). For surface-piercing structures, wave-breaking effects encountered at intermediate depths magnify the horizontal force of the reaction support almost up to 3 times, when compared to the non-breaking wave condition (Stansby et al., 2013). These constraints to bed-connected structures have motivated the development of alternative floating concepts for tidal turbines.

6.3 Floating Support Structures for Horizontal-Axis Turbines

Several floating and moored platforms are now in development as an alternative approach to rigid-bed-connected structures. Examples of moored systems are given in Figure 6.3 and Figure 6.4. These structures allow small rotation of the platform resulting in approximately linear displacement of the rotor with the requirement to provide stability in all operating conditions. However, the extent of rotor motion and of dynamic loading may affect the reliability and integrity of the gearbox, blades, bearings and nacelle. Modern turbine designs typically permit a higher amplitude of the rotor pitch during operation in comparison to a rigidly supported turbine. For example, dynamic operation is acceptable for pitch of the rotor of up to 9 degrees from the vertical (Berthelsen and Fylling, 2011).

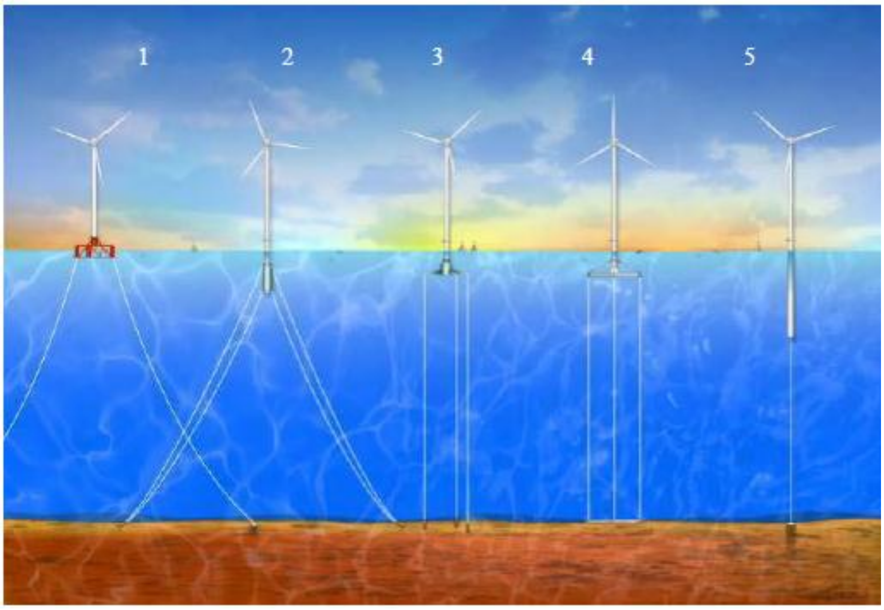

Figure 6.3 Demonstration systems for deep-water regions. Different floating structures denoting a 1) semi-submersible type 2) spar buoy design 3) Tension leg platform 4) TLP gravity 5) spar system. Source from Musial and Ram (2010).

The different types of floating system can be classified by the operational means for achieving stability: the ballast, mooring and buoyancy class. Several technical reports have described their status, total costs, possible environmental effects, and the engineering challenges usually encountered (Henderson et al., 2010; Butterfield et al., 2007; Laura and Vicente, 2014). These can be summarised as:

- Ballast class - uses the weight of ballast placed below the water, to counteract the moment due to turbine and tower force and thus minimise the oscillation response. The minimum depth required is normally above 150 m. A typical support is the spar buoy (Figure 6.4a). The disadvantages can be the high capital cost and the reaction to wave and external loads.
- Tension leg type - mooring lines attached to the seabed provide sufficient tension to stabilise the system. A common example is a tension leg platform, TLP, which restrains vertical motions but allows small horizontal displacements and rotations. The depth of deployment is above 50 metres and is considered as a practical approach in terms of present offshore experience. However, anchor failure leading to slack mooring lines compromise the stability of the whole system.
- Buoyancy - the structural arrangement and water plane area are selected to counteract the applied overturning moment and dynamic loads. The semi-submersible structure with wind turbine above or tidal turbine below (Figure 6.4b) is an example of this concept. Typically these systems are slack-moored. The main advantage of this method is the low draft which simplifies deployment. Additionally, some electrical components could be placed in compartments above the free surface to minimise corrosion and to facilitate maintenance of the system. The disadvantages of a buoyancy-mooring device are the high reaction to waves and external loads, the uncertainty in the dynamic response and the design of appropriate engineering tools.

Turbine system designs are still evolving and, as a result, progress in this field has been increasing. Perhaps the earliest trial of a floating platform, is the Hywind system (Sun et al., 2012), which has been tested offshore for nearly two years (Figure 6.4a). This 2.3 MW wind turbine was constructed by the Norwegian Statoil Hydro Company and had a spar buoy support 120 m long. It has gained considerable offshore experience and multiple devices are currently undergoing trials as part of a small farm.

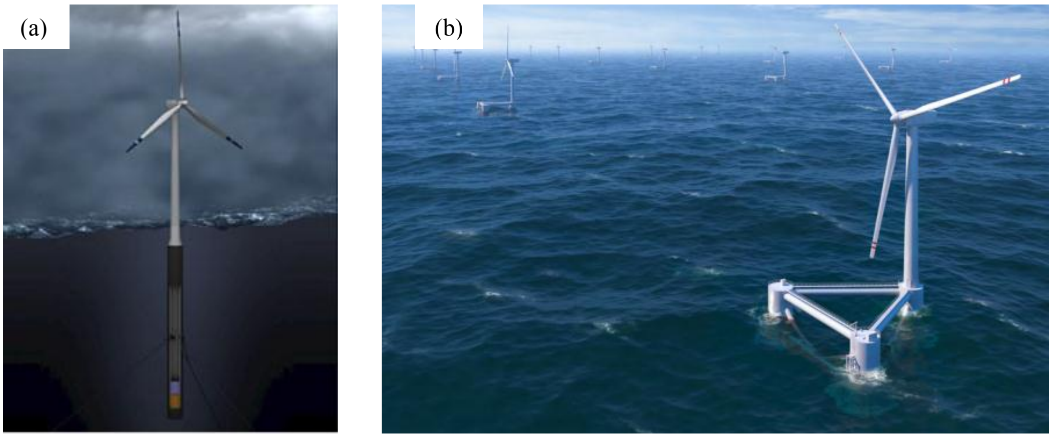

Figure 6.4 Floating offshore turbines configurations for wind turbines at deep waters a) Deployment of Hywind spar buoy turbine (Sun et al., 2012). b) Novel concept of a floating offshore turbine for deep waters (Weinstein et al., 2012).

Another concept is the semi-submersible WindFloat designed by Principle Power Inc. (Weinstein et al., 2012; Roddier and Cermelli, 2014). The system supports a 2 MW turbine and employs conventional anchoring and mooring lines. The platform consists of three cylindrical floats connected by a rigid triangular framework. The damping and buoyancy properties of the cylinders reduce the dynamic motion and maintain the turbine in a vertical position. The scope of deployment is for intermediate and deep waters.

Floating structures similar to those proposed for wind turbines have been proposed for deployment of tidal turbines. An advantage of such support structures is that the turbine will be self-aligning with the incident flow. Furthermore, due to the typical vertical profiles of velocity at tidal sites, the velocities in the upper region of the water depth are typically greater than near the bed surface, thus increasing the kinetic energy flux available at hub height. Perhaps the main advantage is that the cost of deployment, retrieval and removal may be substantially lower than for fixed seabed foundations.

Several concepts employ the buoyancy of a component such as the nacelle to keep the structure afloat, whilst depth of immersion is controlled through the length of taut bed-connected mooring. The prototype devices TidEL (Ben Elghali et al., 2007) and CoRMaT (Clarke et al., 2009) are based on this approach. TidEL comprises two contra-rotating turbines located side-by-side downstream of a buoyant crossbar which is taut moored to the seabed. The unit is intended for operational water depths greater than 30 metres and has a nominal rated power of 1MW. By contrast, CoRMat comprises a buoyant single body with two contra-rotating turbines arranged in-line with very small streamwise spacing, of the order of 0.1 diameters. Both rotors operate a single direct-drive generator and two rotors are employed to maximise generator speed for a given flow-speed and to minimise net torque. The support structure is minimal, comprising only a buoyant nacelle and a taut mooring, however stability during operation remains a design issue (Clarke et al., 2010).

Other semi-submersible floating platform concepts have been proposed, such as ScotRenewables (Keysan et al., 2010) and BlueTEC (Van der Plas, 2014). These structures are located at the free surface and are rigid, typically with slack moorings, which may be beneficial for protecting the device and for providing rotor stability with the damping properties of the support. The ScotRenewables prototype comprises an approximately cylindrical tube aligned with the flow direction and with two vertical arms at the stern supporting turbines. The geometry of the structure creates minimal drag with the waves that are propagated in-line with the rotor. It has more reaction to the surface waves but also provides a large moment to counteract the turbine's response. The main advantage is that the system allows protection from peak loads and undesirable operating conditions by raising an arm that supports each turbine (Scotrenewable Tidal Power Ltd.). The BlueTEC design is analogous to the ScotRenewables and is also intended as a generic slack moored system to provide stability for supporting either two horizontal or vertical-axis turbines.

In order to support the development of tidal stream turbines on the floating platforms, several design and operating issues need to be established. These include the prediction of the variance and mean rotor loading in uniform flow, turbulent flow, and waves combined with mean flow as well as dynamic loading due to rotor oscillatory motion. Likewise, it is necessary to account for the effects of structure response in waves combined with a mean flow that has turbulence present and the coupling of this motion with the rotor response. In general, it is desired for a support structure to have a large water plane area, a low centre of gravity, and natural period distinct from the wave period to minimise motion due to waves.

Since a tidal stream turbine is located underwater, there are also other design issues to consider which do not affect wind turbines. These include the selection of the blade materials (Grogan et al., 2013), prevention of cavitation (Bahaj, Molland, et al., 2007), bio fouling (Walker et al., 2014) and corrosion.

6.4 Floating Platform Dynamic Models

At present, a few numerical models account for the mooring load and the coupling of support structure and rotor. For these dynamic models, the force on the rotor has been modelled using BEM (Way et al., 2013) and CFD methods (Francis and Hamilton, 2007), in order to predict the response of scaled semi-submersible systems, such as the Bluetec (Van Riet Bergen et al., 2013; Van der Plas, 2014), ScotRenewables (Francis and Hamilton, 2007) and other mooring concepts (Hayman et al., 2013), in flow conditions that are representative of tidal stream sites. These approaches have been used to model loading of two rotors attached to a semi-submersible structure located at the free surface, under the assumption that the thrust from each turbine is self-aligning with the mean flow and limits to a large extent the yaw moment applied to the support structure. If the heave response and velocity variation of the wave-current flow over the rotor is small, only the surge and pitch motion of the dynamic support contribute significantly to the rotor's variation of incident flow and hence affect the developed rotor thrust (Van der Plas, 2014). For a surface-piercing support platform, the tower supporting each rotor will also add thrust moments and oscillations to the system which must be counteracted by the mooring lines and dynamic response of the support.

The force ratio obtained between the rotor and the semi-submersible support due to uniform flows of different speeds, in which the range of the flow speeds is within the time-varying velocity of the wave-current flows, has been reported to be as much as 4 to 15 (Way et al., 2013). Therefore, the prediction of rotor force due to combined waves, mean flow and streamwise oscillations plays a crucial role in the design of tidal floating supports.

An approach to predict the dynamic response of a floating support, as followed here, consists of decoupling the rotor forces from the structure dynamics and then incorporating the rotor loading, support loading and external constraints into a coupled model (see Figure 6.5) of system response. The characteristic length of the supporting platform is typically greater than one-fifth of a wavelength, $D > 0.2L_{\mathrm{w}}$. As such wave induced forcing is in the diffraction regime and viscous effects are typically neglected. The response of the support structure develops a radiation damping force defined by forcing of the body in still water $X_{\mathrm{h,i,j}} = -a_{\mathrm{i,j}}\ddot{x}_{\mathrm{j}} - b_{\mathrm{i,j}}\dot{x}_{\mathrm{j}}$, where $a_{\mathrm{i,j}}$ and $b_{\mathrm{i,j}}$ denote the added mass and damping of the support platform oscillating with complex velocity amplitude $\dot{x}_j$. This is linearly superposed with the wave-induced force on the body when held stationary in regular waves X_i. Here, the subscript i=1…6 denotes the force or moment corresponding to surge, sway, heave, roll, pitch and sway and j=1…6 the components of the coupled motion in the same notation. The excitation force from n, the number of rotors is obtained using a Morison equation based on relative velocity at the rotor, following the approach of Chapter 4.

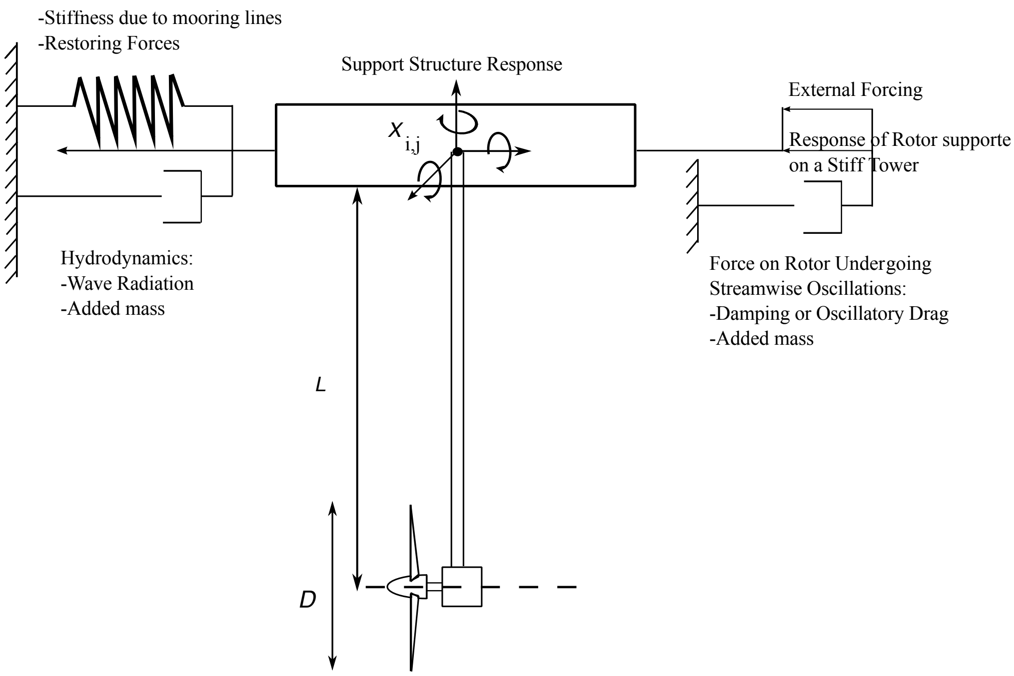

Figure 6.5 Scheme of the forces modelled from the floating system for six-degree freedom of motion.

The force on the rotor is then dependent on the inertia and drag force from the drive train, $F_{I,11}$, $F_{D,11}$, which are dependent on the added mass and drag coefficient, C_a, C_D, the mean flow velocity (u_0), the wave induced velocity, ($u_{wave,p}$) and the velocity of the rotor in surge mode ($\dot{x}_{rotor,1}$) due to surge ($\dot{x}_1$) and pitch ($\dot{x}_5$) of the supporting platform. The force due to turbulent fluctuations is not simulated. Instead, the force associated with the turbulent predictions (F', $F'_{\frac{1}{n}}$) is superposed with the simulated force due to steady flow, waves and response. This approach was shown to provide reasonable prediction of peak force due to oscillation in turbulent flow in Chpater 4 and due to turbulent flow with waves in Chapter 5.

The force on a rotor, $F_{\mathrm{I},11} + F_{\mathrm{D},11}$, is approximated with drag and added mass coefficients of $C_{\mathrm{D}} = 2$ and C_{a} =0.12 over the KC range 0 to 2 (see Chapter 4). In Chapter 4, the added mass was normalised to the water mass of a spheroid enclosing the rotor , $M_{\mathrm{a}} = \frac{1}{3}\rho D^3$. To facilitate solution of an equation of motion, it is convenient for all the masses to be consistent. Herein the added mass coefficient is thus expressed in terms of the water mass enclosed by a thin disc, $\rho V = \frac{1}{4}\pi D^2 t_{\mathrm{h}}$ where $t_{\mathrm{h}} = 0.022D$ is the thickness of the disc, as per the Froude-Krylov force. The added mass coefficient is $C'_{\mathrm{a}} = 0.12\frac{M_{\mathrm{a}}}{\rho V} = 2.28$. The inertia and drag force per rotor is obtained from Eq. 2.39 and Eq. 2.47.

The general equation of motion for the rotor is obtained by coupling a six-degree-of-freedom equation of motion for the floating support (Faltinsen, 1993; Journée and Massie, 2001) with rotor forcing, inertia and damping:

$$\sum_{\mathrm{j}=1}^{6}\left(m_{\mathrm{i,j}} + a_{\mathrm{i,j}}\right)\ddot{x}_{\mathrm{j}} + \mathrm{n}m_{\mathrm{rotor,i,j}}\ddot{x}_{\mathrm{rotor,j}} + b_{\mathrm{i,j}}\dot{x}_{\mathrm{j}} + c_{\mathrm{i,j}}x_{\mathrm{j}} = X_{\mathrm{i}} + X_{\mathrm{e,i}} + \mathrm{n}X_{\mathrm{D,i,j}}\left(\dot{x}_{\mathrm{rotor,j}}, u_0, u_{\mathrm{wave,p}}\right) + \mathrm{n}X_{\mathrm{I,i,j}}\left(\ddot{x}_{\mathrm{rotor,j}}, \dot{u}_0, \dot{u}_{\mathrm{wave,p}}\right) \quad \text{Eq. 6.1}$$

where $X_{\mathrm{D,i,j}}$ and $X_{\mathrm{I,i,j}}$ correspond to the force or moment due to the drag and inertia of the rotor in the six coupled modes. Restoring force and moment of the support structure, $c_{\mathrm{i,j}}$, is due to the buoyancy forces in each mode. External forcing, $X_{\mathrm{e,i}}$, is applied to the system to represent, wave drift and other non-linear effects such as mooring line constraint. The response from the mooring lines is approximated as a spring with a constant stiffness, $k_{\mathrm{i,j}}x_{\mathrm{j}}$.

The particular focus of this study is the effect of waves and induced motion of the support on the peak value of rotor thrust. This may be either, increased or decreased due to the combination of turbulent flow and oscillatory flow due to both wave-induced kinematics (Chapter 5) and due to motion of the rotor rigidly connected to the supporting platform (Chapter 4). It is desirable to identify the support platform properties that would result in a reduction of rotor response in slowly-varying oscillating motions that are representative conditions for tidal flows.

The investigation is limited to two modes of support platform response – pitch and surge. Motion in other modes would affect rotor orientation but would have limited influence on velocity normal to the rotor plane. The length of the tower, L, is considered large compared with the rotor displacement and so the pitch oscillation imposed on the support is approximated as surge of the rotor thus $x_{\text{rotor},1} = x_1$ and $x_{\text{rotor},5} = x_5 L$.

The equation of motion for surge is (i=1):

$$\sum_{\text{j}=1,5} \left(m_{11} + a_{1\text{j}}\right)\ddot{x}_\text{j} + \text{n}m_{\text{rotor},11}\ddot{x}_{\text{rotor,j}} + b_{1\text{j}}\dot{x}_\text{j} + c_{1\text{j}}x_\text{j} + k_{1\text{j}}x_\text{j} = X_1 + X_{\text{e},1} + \text{n}F_{\text{D},1\text{j}}\left(\dot{x}_{\text{rotor,j}}, u_0, u_{\text{wave,p}}\right) + \text{n}F_{\text{I},1\text{j}}\left(\ddot{x}_{\text{rotor,j}}, \dot{u}_0, \dot{u}_{\text{wave,p}}\right) \quad \text{Eq. 6.2}$$

and for pitch (i=5)

$$\sum_{\text{j}=1,5} \left(m_{55} + a_{5\text{j}}\right)\ddot{x}_\text{j} + \text{n}Lm_{\text{rotor},11}\ddot{x}_{\text{rotor,j}} + b_{5\text{j}}\dot{x}_\text{j} + c_{5\text{j}}x_\text{j} + k_{5\text{j}}x_\text{j} = X_5 + X_{\text{e},5} + \text{n}LF_{\text{D},1\text{j}}\left(\dot{x}_{\text{rotor,j}}, u_0, u_{\text{wave,p}}\right) + \text{n}LF_{\text{I},1\text{j}}\left(\ddot{x}_{\text{rotor,j}}, \dot{u}_0, \dot{u}_{\text{wave,p}}\right) \quad \text{Eq. 6.3}$$

A typical platform is then approximated using a horizontal circular cylinder of length $5D$ and width D with hemispherical ends of radius of the half width ($0.5D$). A diameter $D = 0.27$ m is considered consistent with the lab-scale studies of previous chapters. The length of the tower is 3 times the rotor diameter. The system modelled here is approx. 1:70th scale based on the rotor's diameter. The support is intended for operational water depths of 60-80 metres such as found in the deep Pentland Firth. The configuration of the semi-submersible structure supporting two contra-rotating rotors is as shown in Figure 6.6. These dimensions are indicative of the systems studied by Van der Plas (2014) and Francis and Hamilton (2007) at a reduced scale of 1:5-10.

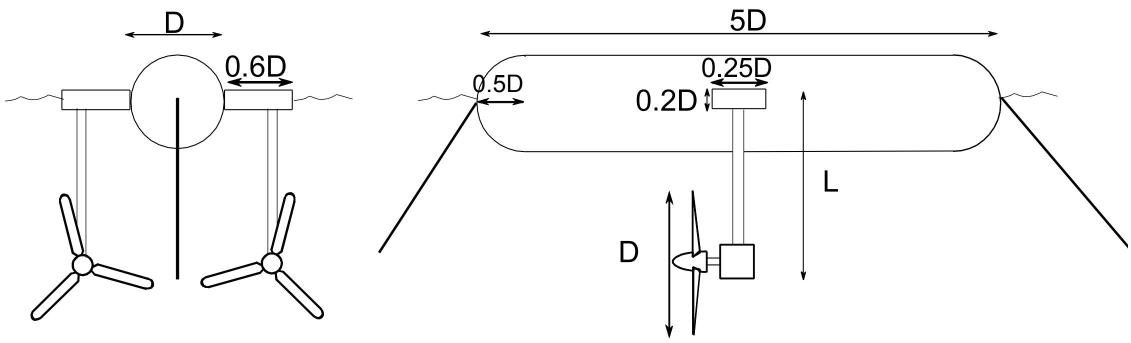

Figure 6.6 Idealised platform supporting two rotors. Concept analogous to the Bluetec (Van der Plas, 2014) and ScotRenewables (Francis and Hamilton, 2007) device. Not drawn to scale.

6.5 Hydrostatic and Hydrodynamic Coefficients of Floating Support Structures

The diffraction code WAMIT^{TM} is employed to obtain the wave-induced moments, forces, added mass and radiation damping for each mode of motion for the geometry of typical tidal support structure. WAMIT^{TM} is an industry standard code used for the design of many offshore structures with extensive validation (Lee et al., 1996; Jonkman and Buhl Jr, 2007; Gao and Moan, 2009).

The hydrodynamic forces and moments of geometries are obtained by solving the flow potential around the body. This velocity potential is estimated using Green's second theorem to convert the potential flow of the volume into a set of integral equations represented by sources and dipoles distributed at the body surface over panels of a computational mesh. Bodies of arbitrary geometry can be analysed using this approach and the accuracy depends on the number of panels employed. The user provides the inputs of wave conditions, geometry, constraints and modes of response. WAMIT^{TM} provides the potential coefficients in the frequency domain with no current interaction. To account for wave frequency shift due to the current due to the Doppler effect, the frequency of waves incident to the floating platform is evaluated by $f = \frac{\omega - ku_0}{2\pi}$. Wave excitation force in the surge mode is determined via the Haskind relations and is described by amplitude ($\|X_\mathrm{i}\|$) and phase (δ) relative to the incident wave. Hydrodynamic restoring force in the surge mode is zero. Restoring moment in the pitch mode, c_{55}, is obtained from the water mass displaced per unit rotation.

Forcing, added mass and radiation damping are obtained for the pitch and surge mode for the range of wave frequencies of 0.6-1.5 Hz in 0.01 Hz increments and for a wave amplitude of 15 mm. These wave conditions represent wave periods of 5.5-14 s for a unit wave amplitude at a full scale. The half section of the immersed part of the support, shown in Figure 6.7, is modelled applying geometric symmetry in the *y*-*z* plane about *x* = 0.

The hydrodynamic coefficients, moment and forces obtained for the support are then made proportional to the mechanical properties imposed on the rotor. The intention of the normalisation is to investigate the relative rotor and support contribution to the dynamic response, allowing identification of the range of support parameters (using Eq. 6.2 and Eq. 6.3) that mitigate peak loads on the rotor.

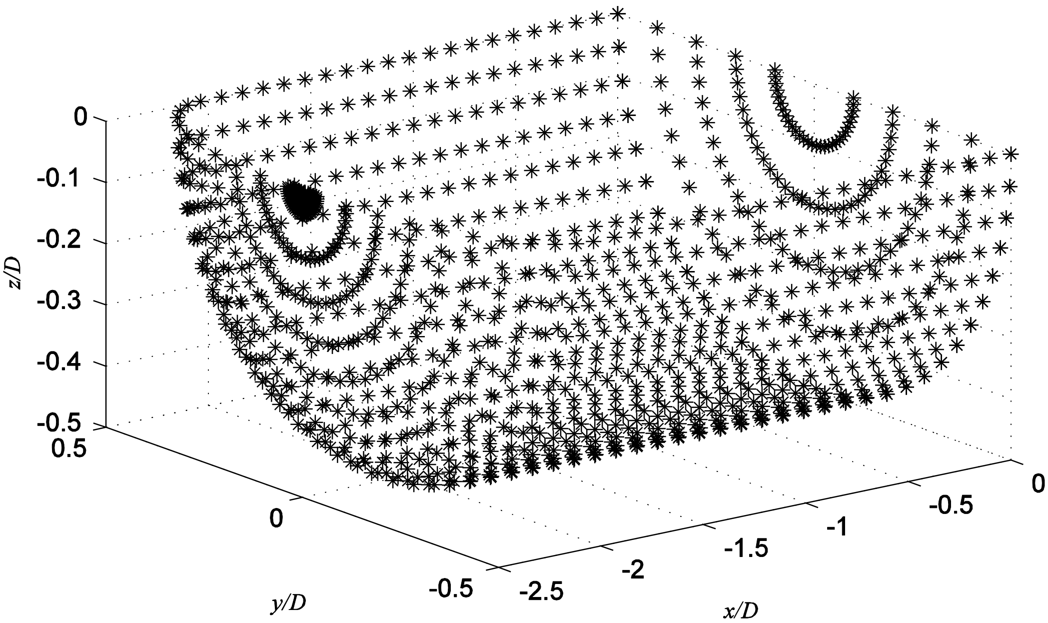

Figure 6.7 Half section of the immersed cylindrical body with hemispherical ends.

6.6 Wave Induced Forces and Moments

The force and moment on the platform for each mode are related to the surface elevation, $\eta = A_{\text{wave}} \cos\ (kx + \omega t)$. The wave excitation force amplitude is proportional to the wave elevation, A_{wave}, and the force phase differs to the elevation depending on frequency. For a given frequency, the force on the support structure is:

$$X_{\text{i}} \propto A_{\text{wave}} \cos\ (kx + \omega t + \delta) \qquad \text{Eq. 6.4}$$

To relate with the rotor forces in the coupled modes, the amplitude of the force on the platform is divided with the peak response of the dynamic rotor operation. The force on the support is then expressed as:

$$X_{\text{i}} = \mathrm{K}_{\text{i}} \cos\ (kx + \delta + \omega t) \qquad \text{Eq. 6.5}$$

where K_{i} represents the ratio of force or moment on the support to the force on all supported rotors. For the surge mode, the force multiplier is $|X_1| = \mathrm{K}_1 F_{\text{D,max}}$, where $F_{\text{D,max}}$ denotes the maximum force on the rotor due to forced oscillation in mean flow. The rotor force is estimated from Eq. 4.13, with an oscillatory velocity amplitude of 40% of mean flow velocity ($\|\dot{x}_{\text{max}}\| = 0.4u_0$, see Figure 4.9) and a drag coefficient of 2.0. Peak force for the n supported rotors is then:

$$F_{\mathrm{D,max}} = \mathrm{n}F_0 + \mathrm{n}\frac{1}{2}\rho A C_{\mathrm{D}} \|\dot{x}_{\mathrm{max}}\| (u_0 + \|\dot{x}_{\mathrm{max}}\|) \qquad \text{Eq. 6.6}$$

The force in the support for surge motion becomes:

$$X_1 = \mathrm{K}_1 F_{\mathrm{D,max}} \cos\,(kx + \delta + \omega t) \qquad \text{Eq. 6.7}$$

Similarly to the surge force (using Eq. 6.5), the wave excitation moment on the support in pitch is assigned an amplitude of the maximum moment generated by number of supported rotors, $LF_{\mathrm{D,max}}$ multiplied by a factor, K_1. The moment is:

$$X_5 = \mathrm{K}_5 F_{\mathrm{D,max}} \cos\,(kx + \delta + \omega t) = \mathrm{K}_1 L F_{\mathrm{D,max}} \cos\,(kx + \delta + \omega t) \qquad \text{Eq. 6.8}$$

The ratio of the support forces and moments over the rotor obtained for this geometry for wave amplitude of 15 mm and a range of wave frequencies is shown in Figure 6.8. It is observed that the amplitude of the force and moment for the support tends to decrease with the frequency and its magnitude is around 0.05–0.35 times the peak rotor force. The phase difference between the force and surface elevation, in the surge mode is approximately at maximum and minimum at the frequency range of 1.03-1.08 Hz and reaches to 0 at the frequency of 1.5 Hz. For the phase difference between pitch force and surface elevation, values close to $\pm\pi$ and 0 are obtained at the frequencies of 1.22-1.28 Hz and 1.6 Hz approx.

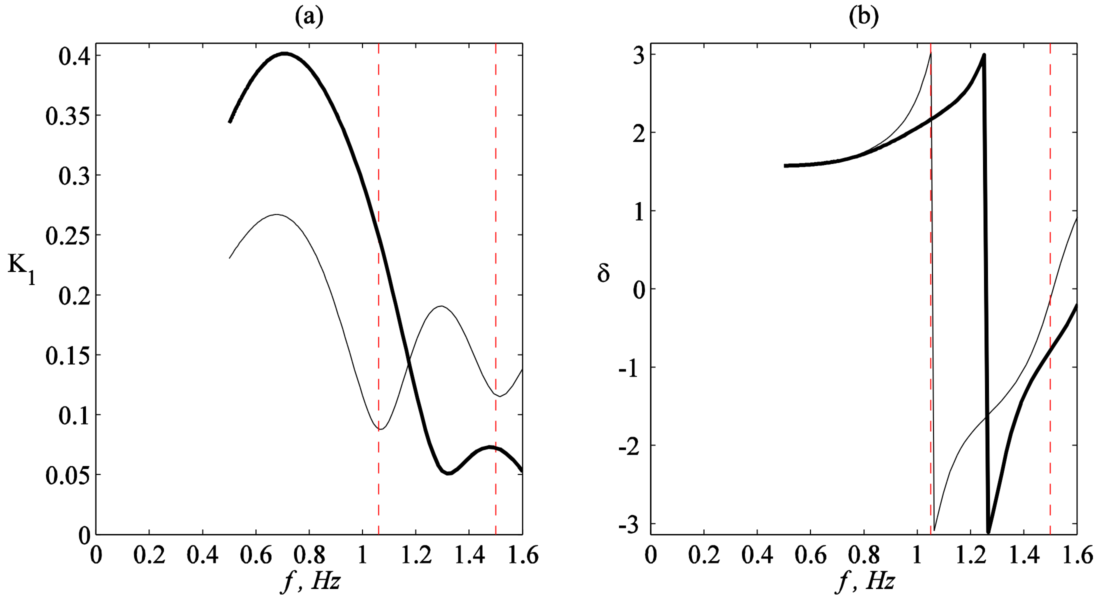

Figure 6.8 Forcing of the semi-submersible structure relative to the rotor for modes in surge (-) pitch (**—**). a) Ratio of forces acquired on the support relative to the rotor. b) Phase difference (radians) between the wave force on the support and the surface elevation. Two wave conditions (¦) providing a phase difference between the surge force and surface elevation close to 0 and $\pm\pi$.

In Figure 6.9, the forcing obtained for this geometry is plotted against the time-varying surface elevation for regular waves of 1.05 Hz and 1.5 Hz. The force is in phase with surface elevation for the higher frequency and there is a phase lag of delta $=[-0.98\ 0.964]\pi$ for the lower frequency. The phase lag of the lower frequency is approximated to π or $-\pi$ and this has a negligible effect on the time-varying force. These wave conditions represent a 1 m wave amplitude with periods of approx. 5.5 s and 8 s at a full scale.

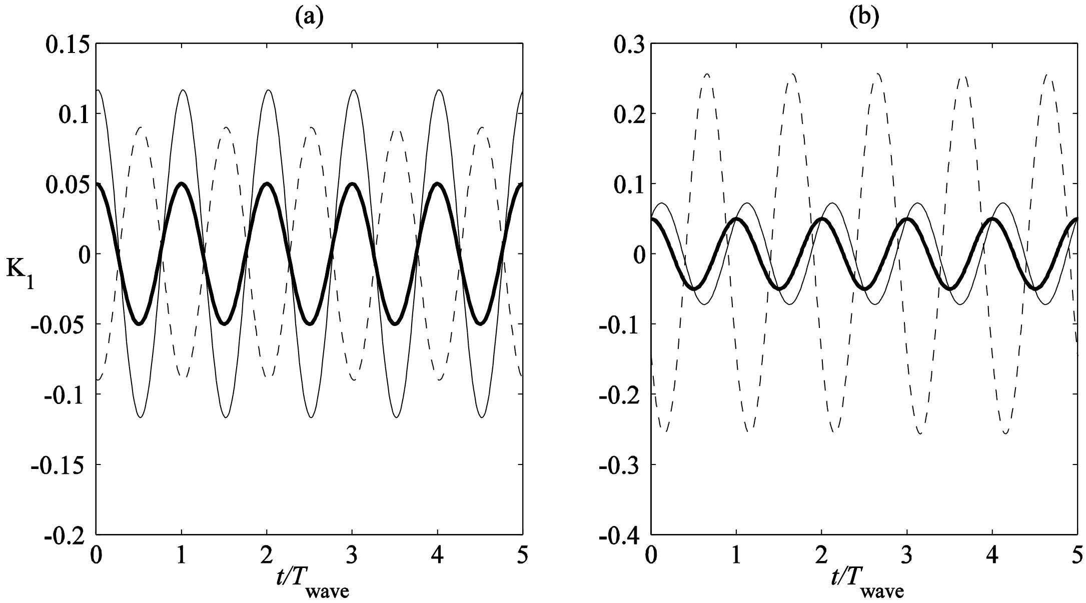

Figure 6.9 a) Ratio of surge force, $X_1/F_{\mathrm{D,max}}$ and b) pitch moment, $X_5/(LF_{\mathrm{D,max}})$, on the support relative to the surface elevation (thick line) for two studied wave conditions.(thin line), f =1.5 Hz; (dashed line), f =1.05 Hz. Surface elevation has unit amplitude and shown on this scale to illustrate phase difference only.

6.7 External Forcing

External forcing on the support is considered due to fluctuating drag on the towers connected the support to each turbine and due to mooring lines. Force on each rigid tower is taken approximately as 8% of the mean thrust in the turbulent channel flow only, $X_{\mathrm{e},1} \approx$ n$0.08F_0$ (see Chapter 3 and 4). For a floating platform, the surge stiffness, k_{11}, would be dependent on the mooring line tension. Aspects of stiffness design of the mooring lines must be appraised for the safe keeping of the device in extreme wave conditions. However, these are not considered and mooring-line constraints are approximated as a spring of a low constant stiffness so that the platform is flexible enough to allow rotor displacements, $\|x_{\mathrm{rotor},1}\|/D$, up to 0.06. This range of displacement represents approx. pitch oscillations of the rotor up to 1 degree, well within the range typically required for safe turbine operation (Berthelsen and Fylling, 2011). To obtain that range of rotor displacements, herein, the stiffness for surge and coupled surge-pitch mode is defined as 6% and 15% of the experimental rigid rod structure. Stiffness of the mooring due to coupled pitch and surge (k_{15}, k_{51}) is neglected.

6.8 Damping and Added mass

The damping of the support structure in each mode is normalised to the maximum damping due to rotor dynamic response, $b_{\mathrm{max,i,j}}$. This damping ratio is:

$$b_{\mathrm{k,i,j}} = \frac{b_{\mathrm{i,j}}}{b_{\mathrm{max,i,j}}} \qquad \text{Eq. 6.9}$$

In the surge mode, the damping of a disc equivalent to the rotor varies with KC and has a best-fit trend as (see Figure 4.4 and Eq. 4.5):

$$b = \mathrm{n}0.152 C_{\mathrm{b}} KC \qquad \text{Eq. 6.10}$$

Therefore, the damping in the surge mode is calculated by substituting the velocity ratio,$\|\dot{x}_{\mathrm{max}}\| = 0.4u_0$ into Eq. 6.10. The maximum value considered is:

$$b_{\mathrm{max,11}} = \mathrm{n}\|\dot{x}_{\mathrm{max}}\| 0.152 \frac{4}{3}\pi\rho D^2$$

Support structure inertia is expressed with a factor, $M_{\mathrm{k,i,j}}$, that denotes the relative mass between the support and the mass of the rotors supported. The ratio of mass is:

$$M_{\mathrm{k,i,j}} = \frac{m_{\mathrm{i,j}} + a_{\mathrm{i,j}}}{\mathrm{n}\left(m_{\mathrm{rotor,i,j}} + \rho V {C'}_{\mathrm{a_{i,j}}}\right)} \qquad \text{Eq. 6.11}$$

where $m_{\mathrm{rotor,i,j}} = \frac{\pi D^2 t_{\mathrm{h}}}{4}$ denotes the mass of a disc equivalent to a rotor. The added mass of the support platform is defined in a similar manner:

$$a_{\mathrm{k,i,j}} = \frac{a_{\mathrm{i,j}}}{\mathrm{n}\rho V {C'}_{\mathrm{a_{i,j}}}} \qquad \text{Eq. 6.12}$$

For motion in pitch, the moment of inertia of the support is obtained from geometry about an origin at the centre of mass of the supporting platform. The tower supporting each rotor is considered as a rigid cantilever connecting to the centre of the support platform and hence the moment of inertia at one end of the rigid rod is $m_{\mathrm{rotor,55}} = \frac{1}{12}mL^2$. Since the rotor displacement is considered much smaller than the tower length, the moment of inertia of the support relative to the rotor is written:

$$M_{\mathrm{k,5,5}} = \frac{m_{55} + a_{55}}{\mathrm{n}L m_{\mathrm{rotor,11}} + \mathrm{n}L\rho V {C'}_{\mathrm{a}}} \qquad \text{Eq. 6.13}$$

and the ratio of the added mass is:

$$a_{\mathrm{k,55}} = \frac{a_{55}}{\mathrm{n}L\rho V {C'}_{\mathrm{a}}} \qquad \text{Eq. 6.14}$$

In a similar way, the relative damping (in pitch) between the support and rotor is obtained from the damping of the rotor in surge multiplied by the lever arm as:

$$b_{\mathrm{k},55} = \frac{b_{55}}{Lb_{\mathrm{max},11}} \qquad \text{Eq. 6.15}$$

The ratio of damping and inertia for both surge and pitch modes obtained for the typical platform using the damping and inertia of two rotors, $\mathrm{n} = 2$, is shown in Figure 6.10.

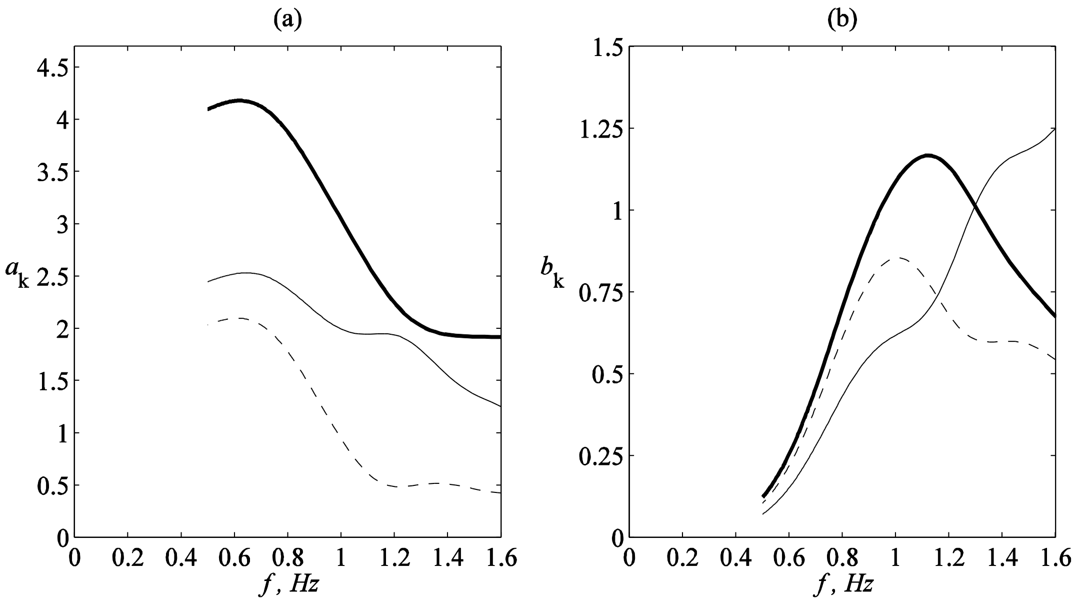

Figure 6.10 Ratio of hydrodynamic coefficients between the semi-submersible structure and the rotor for modes corresponding to surge (-), pitch (**—**) and surge respect to pitch (--).

For the two modes, the added mass of the support tends to be larger than for the rotor and this decreases with the frequency of the wave. The damping of the support for the surge mode is observed to increase with the frequency. However, for the mode in pitch, damping is maximum around 1 Hz and decreases at higher values.

6.9 Single Mode Response: Surge Only

The objective of this section is to identify a combination of support-structure parameters – forcing, added mass and damping – that mitigate peak rotor loads compared to a rigid support. The approach taken is to characterise the contribution of structure dynamics to the extreme loads experienced by the rotor with the range of damping, mass of support and ratio of forces analysed in Sections 6.6, 6.7 and 6.8. Initially motion in surge only is considered (mode j=1 in Eq. 6.2). The time-varying response of the rotor motion, x_1, is obtained and the corresponding force (F_{osc}) is then analysed for the peak force applied to the dynamically responding rotor. The equation of motion for response in surge only is:

$$X_1+X_{\text{e},1}+\text{n}\left(F_{\text{I},11}\left(\ddot{x}_1,\dot{u}_0,\dot{u}_{\text{wave,p}}\right)+F_{\text{D},11}\left(\dot{x}_1,u_0,u_{\text{wave,p}}\right)\right)$$
$$=\left(m_{11}+a_{11}+\text{n}m_{\text{rotor},11}\right)\ddot{x}_1+b_{11}\dot{x}_1+k_{11}x_1 \qquad \text{Eq. 6.16}$$

The extreme force imposed on the rotor due to dynamic response is obtained using the process of Section 4.7, by superposing the maximum force due to relative velocity, mean flow and turbulence alone, $F'_{\frac{1}{\text{n}}}$. The extreme force is made proportional to the mean thrust of the dynamic response, $\bar{F}$ and written as:

$$\frac{F_{\frac{1}{\text{n}},\text{dynamic}}}{\bar{F}}=\left[\frac{F_{\text{osc,max}}}{\bar{F}}\right]+\frac{F'_{\frac{1}{\text{n}}}}{\bar{F}} \qquad \text{Eq. 6.17}$$

The influence of the structure dynamics on the extreme support loads is described by the ratio of extreme forces imposed on a rotor supported on a stiff tower and subjected to the same operating flow, which consists of a turbulent flow combined with opposing waves. A ratio between peak force on the flexible and rigid supports is calculated from Eq. 4.17 and Eq. 6.17 as:

$$F_{\text{K}}=\frac{F_{\frac{1}{\text{n}},\text{dynamic}}}{F_{\frac{1}{\text{n}},\text{rigid}}} \qquad \text{Eq. 6.18}$$
$$=\frac{F_{\text{osc,max}}+F'_{\frac{1}{\text{n}}}}{\text{n}\left(F_0+F'_{\frac{1}{\text{n}}}+\frac{1}{2}\rho A C_{\text{D}}\left\|u_{\text{wave,p}}\right\|\left(u_0+\left\|u_{\text{wave,p}}\right\|\right)+X_{\text{e},1}\right)}$$

The procedure to obtain rotor response and force is as follows. Initially, the dynamic force on each rotor due to sum contribution of the drag and added mass is rewritten from Eq. 2.39 and Eq. 2.47 as:

$$F_{\mathrm{D},11}(\dot{x}_1, u_0, u_{\mathrm{wave,p}}) + F_{\mathrm{I},11}(\ddot{x}_1, \dot{u}_0, \dot{u}_{\mathrm{wave,p}}) = \frac{1}{2}\rho A C_{\mathrm{D}}(u_0 + u_{\mathrm{wave,p}} - \dot{x}_1)|u_0 + u_{\mathrm{wave,p}} - \dot{x}_1| + \rho V C'_{\mathrm{a}}(\dot{u}_0 + \dot{u}_{\mathrm{wave,p}} - \ddot{x}_1) + \rho V \dot{u}_{\mathrm{wave,p}} \quad \text{Eq. 6.19}$$

Since the added mass force of a rotor in the turbulent channel flow is typically small compared to the drag force (see Section 4.5), the added mass component is simplified as

$$\rho V C'_{\mathrm{a}}(\dot{u}_0 + \dot{u}_{\mathrm{wave,p}} - \ddot{x}_1) \approx -\rho V C'_{\mathrm{a}} \ddot{x}_1 \quad \text{Eq. 6.20}$$

and so inertia force is

$$F_{\mathrm{I},11}(\ddot{x}_1, \dot{u}_0, \dot{u}_{\mathrm{wave,p}}) = -\rho V C'_{\mathrm{a}} \ddot{x}_1 + \rho V \dot{u}_{\mathrm{wave,p}} \quad \text{Eq. 6.21}$$

Rewriting only the drag force in Eq. 6.19, and by treating the drag due to the mean current velocity separate to drag due to relative velocity associated with waves and rotor motion, the force applied per rotor is:

$$F_{\mathrm{D},11}(\dot{x}, u_0, u_{\mathrm{wave,p}}) = \frac{1}{2}\rho A C_{\mathrm{D},1} u_0 |u_0 + u_{\mathrm{wave,p}} - \dot{x}_1| + \frac{1}{2}\rho A C_{\mathrm{D},2}(u_{\mathrm{wave,p}} - \dot{x}_1)|u_0 + u_{\mathrm{wave,p}} - \dot{x}_1| \quad \text{Eq. 6.22}$$

Assuming that the mean flow is much greater than the maximum of the net velocity due to wave-induced flow and rotor oscillation, the first term in Eq. 6.22 is approximated as:

$$\frac{1}{2}\rho A C_{\mathrm{D},1} u_0 |u_0 + u_{\mathrm{wave,p}} - \dot{x}_1| = \frac{1}{2}\rho A C_{\mathrm{D},1}(u_0{}^2 + u_0 u_{\mathrm{wave,p}} - u_0 \dot{x}_1) \quad \text{Eq. 6.23}$$

For the range of wave velocities and rotor velocities modelled, drag force is dominated by terms dependent on the mean flow ($u_0{}^2$), thus $C_{\mathrm{D},1} = C_{\mathrm{T}}$. Neglecting the terms $u_0 u_{\mathrm{wave,p}}(x_1, t) - u_0 \dot{x}_1$ the force is:

$$\frac{1}{2}\rho A C_{\mathrm{D},1}(u_0{}^2 + u_0 u_{\mathrm{wave,p}} - u_0 \dot{x}_1) \approx F_0 \quad \text{Eq. 6.24}$$

The dynamic force of the rotor is hence reduced to the rotor thrust when supported on a stiff support in a mean flow superposed with a force due to the rotor motion within an incident mean flow with waves:

$$F_{\mathrm{D},11}(\dot{x}_1, u_0, u_{\mathrm{wave,p}}) = F_0 + \frac{1}{2}\rho A C_{\mathrm{D},2}(u_{\mathrm{wave,p}} - \dot{x}_1)|u_0 + u_{\mathrm{wave,p}} - \dot{x}_1| \quad \text{Eq. 6.25}$$

Herein, the second drag is analogous to the drag coefficient due to the oscillatory flow, thus $C_{\mathrm{D},2} \approx C_\mathrm{D}$ (see Section 4.6, Eq. 4.9). After substituting Eq. 6.21 and Eq. 6.25 into Eq. 6.16, the equation of motion for motion in surge only is:

$$\begin{aligned}(m_{11} + a_{11} + \mathrm{n}m_{\mathrm{rotor},11} + \mathrm{n}\rho V C'_{\mathrm{a}})\ddot{x}_1 + b_{11}\dot{x}_1 + k_{11}x_1 \\ = X_1 + 0.08F_0 \\ +\mathrm{n}\left(\tfrac{1}{2}\rho A C_\mathrm{D}(u_{\mathrm{wave,p}} - \dot{x}_1)\left|u_0 + u_{\mathrm{wave,p}} - \dot{x}_1\right| + F_0\right) \\ +\mathrm{n}\rho V \dot{u}_{\mathrm{wave,p}}\end{aligned} \qquad \text{Eq. 6.26}$$

It can be seen that to reduce the thrust fluctuations relative to a rigid support, the drag force resulting from the streamwise oscillation and waves should be out of phase with the wave forcing due to the support. This is to ensure that the right hand side terms of, $X_1 + \mathrm{n}F_{\mathrm{D},11}$, are minimised. The drag force $F_{\mathrm{D},11}$ is mainly due to wave induced horizontal velocity and is in phase with the surface elevation.

To obtain predictions of thrust and response amplitude, the equation of motion (Eq. 6.26) is initially transformed into a set of first-order differential equations (ODE). A solution is then provided in a forward time scheme by a numerical solver. Here, the Matlab solver ODE45 based on the Runge Kutta method is employed. The solution procedure begins by setting the differential equations as:

$$\frac{d}{dt}\begin{bmatrix} x \\ \dot{x} \end{bmatrix} = \frac{d}{dt}[X] = \mathrm{f}_{\mathrm{initial}} \qquad \text{Eq. 6.27}$$

where X is the matrix of the set of differential equations and $\mathrm{f}_{\mathrm{initial}}$, the initial conditions. The conditions are initially set to zero, until a steady periodic solution is reached. The acceleration is then isolated from Eq. 6.26 and substituted into Eq. 6.27 so that the set of differential equations becomes:

$$\begin{aligned}\frac{d}{dt}\begin{bmatrix} x_1 \\ \dot{x}_1 \end{bmatrix} \\ = \begin{bmatrix} \dot{x}_1 \\ \dfrac{X_{\mathrm{e},1} + X_1 + \mathrm{n}F_{\mathrm{D},11}(\dot{x}_1, u_0, u_{\mathrm{wave,p}}) + \mathrm{n}\rho V\dot{u}_{\mathrm{wave,p}} - k_{11}x_1 - b_{11}\dot{x}_1}{m_{11} + a_{11} + \mathrm{n}m_{\mathrm{rotor},11} + \mathrm{n}\rho V C'_{\mathrm{a}}} \end{bmatrix} \\ = \mathrm{f}_{\mathrm{initial}}\end{aligned} \qquad \text{Eq. 6.28}$$

The main advantage of a time domain compared to a frequency model is the allowance of synthetic incident velocities of the combined wave and channel flows. This approach would also allow, at a later date, implementation of non-linear effects such as more realistic mooring lines and wave drift forces.

Initially, the influence of dynamic response on the rotor loading is analysed in wave conditions representative of waves of 1 metre amplitude and periods of 5.5 and 8 s at full scale. These two wave periods are selected since they are representative of wave conditions at tidal stream deployment sites and because the phase corresponding to the wave force is at a maximum or negligible with the surface elevation (see Figure 6.8 and Figure 6.9). The force is predicted with damping ratios, (see Eq. 6.9, Section 6.8), varying from 0.4 to 1.2, a mass ratio (Eq. 6.11) of 1.5, a wave factor (K_1, Eq. 6.7) of 0.15, and a phase difference corresponding to δ= 0 and $\pm\pi$ radians between the surge force and the free surface elevation. These parameter ranges are representative for the wave conditions and typical platform considered (see Figure 6.8 and Figure 6.10).

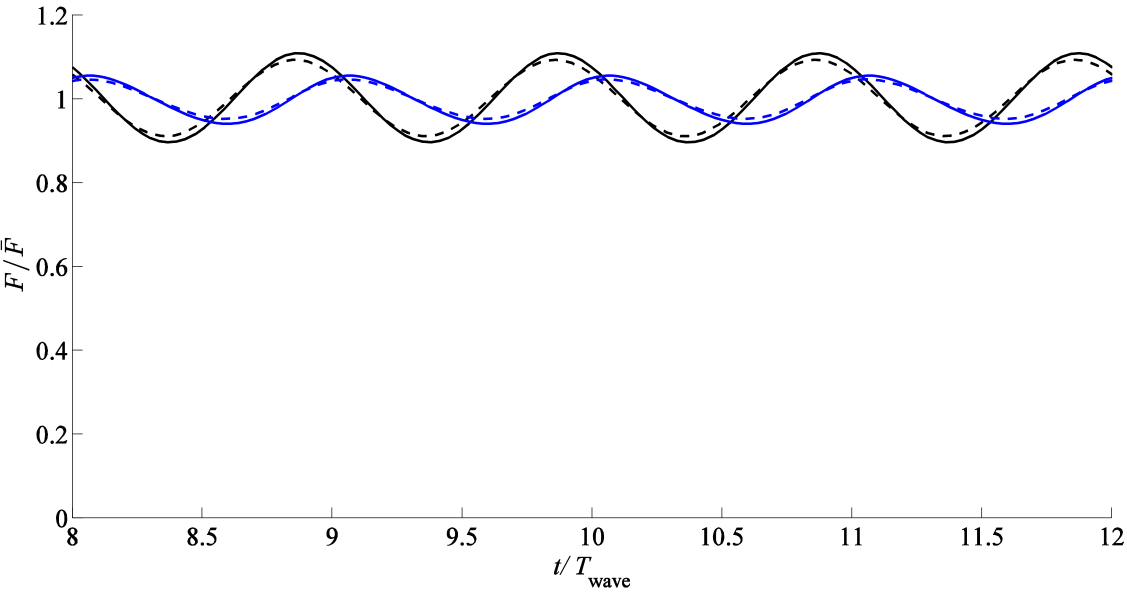

Figure 6.11 Dynamic force exerted on the mooring lines normalised to its mean using a mass ratio of 1.5, K_1=0.15 and support damping ratios. —, f =1.5 Hz, $\frac{b_{11}}{b_{\max}}$ =0.4, δ =0; --, f =1.5 Hz, $\frac{b_{11}}{b_{\max}}$ =1.2, δ =0;—, f =1.05 Hz, $\frac{b_{11}}{b_{\max}}$ =0.4, $\delta = \pm\pi$; --, f =1.05 Hz, $\frac{b_{11}}{b_{\max}}$ =1.2, $\delta = \pm\pi$.

It is observed from simulations of time-varying force (Figure 6.11) that increase of either radiation damping or the phase difference between the support force and the surface elevation, reduce both the rotor response (shown in Figure 6.12) and the magnitude of net thrust on the rotor. However, the change of phase difference between wave force and surface elevation was shown to have a greater effect than the increase of damping of the support platform. The least and most favourable phase of the force support was obtained at 0 and close to $\pm\pi$ radians. The support-structure response has negligible effect on the mean force for all cases.

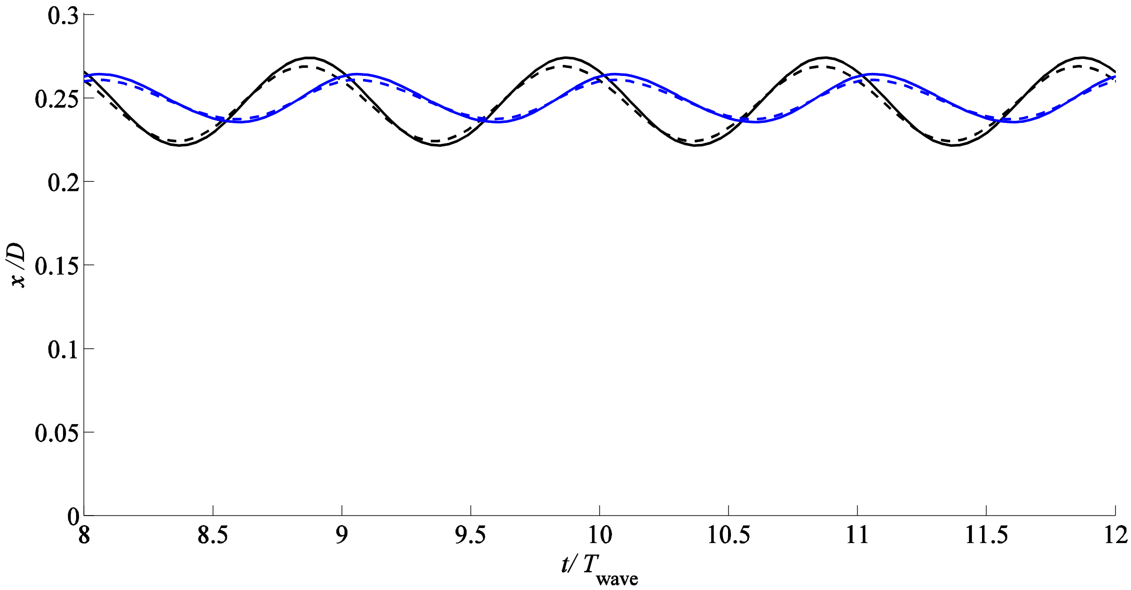

Figure 6.12 Linear displacement in a support unconstrained to surge using representative damping, mass and force ratios. Line styles as Figure 6.11.

To identify support-structure characteristics (excitation force, radiation damping, added mass and stiffness) that reduce the extreme loading, peak forces (1 in 100) were obtained for the studied flexible support (see Section 6.7). Three amplitudes of support platform forces were studied, both without and with a phase difference to surface elevatio. The 1 in 100 forces obtained with force in phase with surface elevation (f =1.5 Hz) for a platform supporting a single rotor are shown in Figure 6.13. Figure 6.14 shows the 1 in 100 forces for the same platform supporting two rotors for the same wave condition. For a single rotor, the dynamic response resulted in extreme loading almost equal or greater than that experienced by a rotor with a rigid support. Increasing the amplitude of the wave force was found to increase the extreme force. However, for multiple rotors on a single structure the additional damping leads to a reduction of the extreme forces by up to 4% in comparison to a single rotor on a rigid support (Figure 6.14a).

For the lower wave frequency (f =1.05 Hz) the ratio of extreme support forces were reduced by up to 12 % for both single- and two-turbine case (see Figure 6.15 and Figure 6.16). This greater reduction is due to the phase difference between the force and surface elevation. The influence of peak loading with increasing or reducing mass of the support was observed to be small.

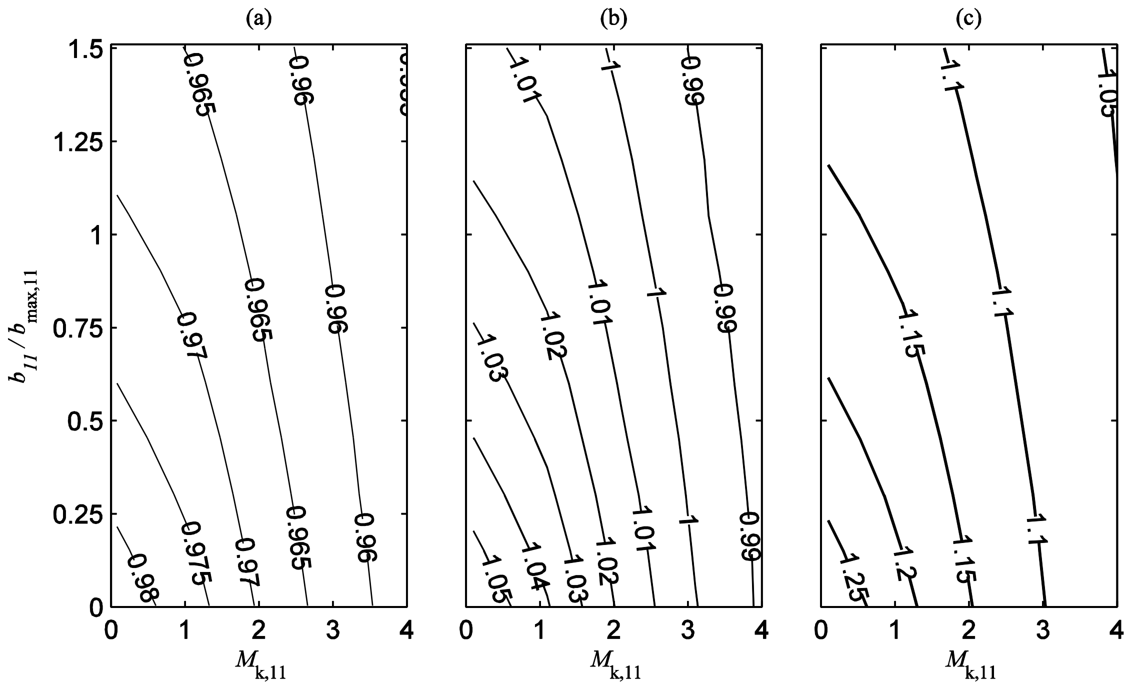

Figure 6.13 Extreme forces with 1% probability of exceedance on one rotor supported from a floating structure relative to same forces on a rigid structure. a) K_1 =0.1. b) K_1 =0.2. c) K_1 =0.3. f =1.5 Hz, δ =0 for all cases.

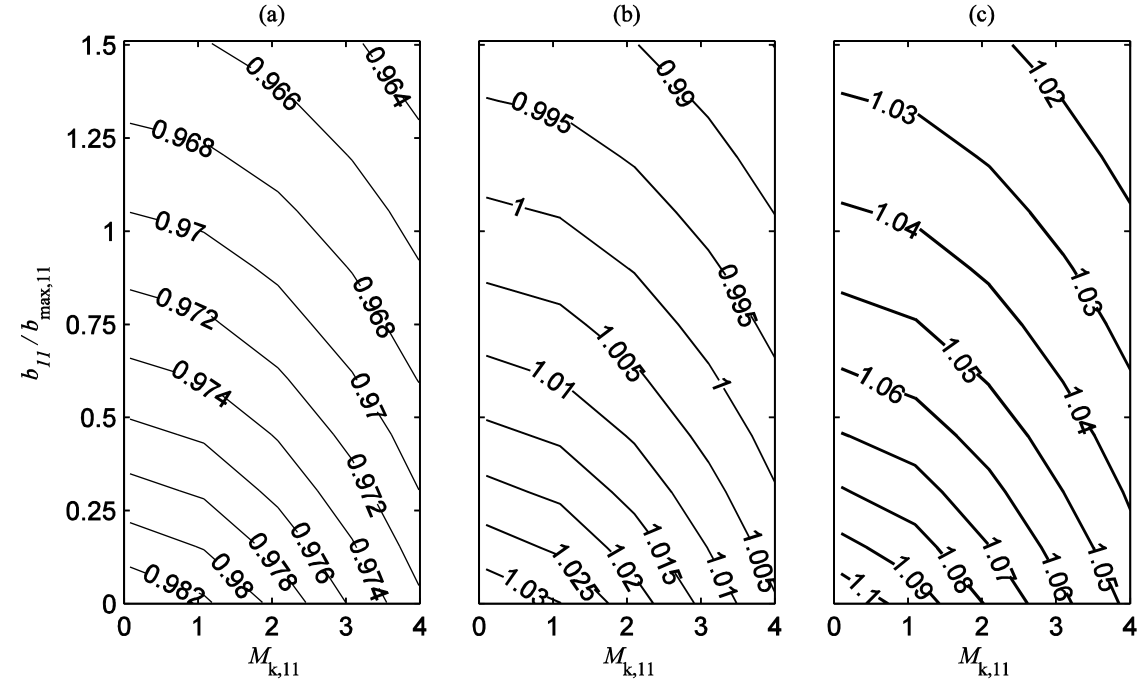

Figure 6.14 Extreme forces with 1% probability of exceedance on one of two rotors supported from a floating structure relative to same forces on a rigid structure. a) K_1 =0.1. b) K_1 =0.2. c) K_1 =0.3. f =1.5 Hz, δ =0 for all cases.

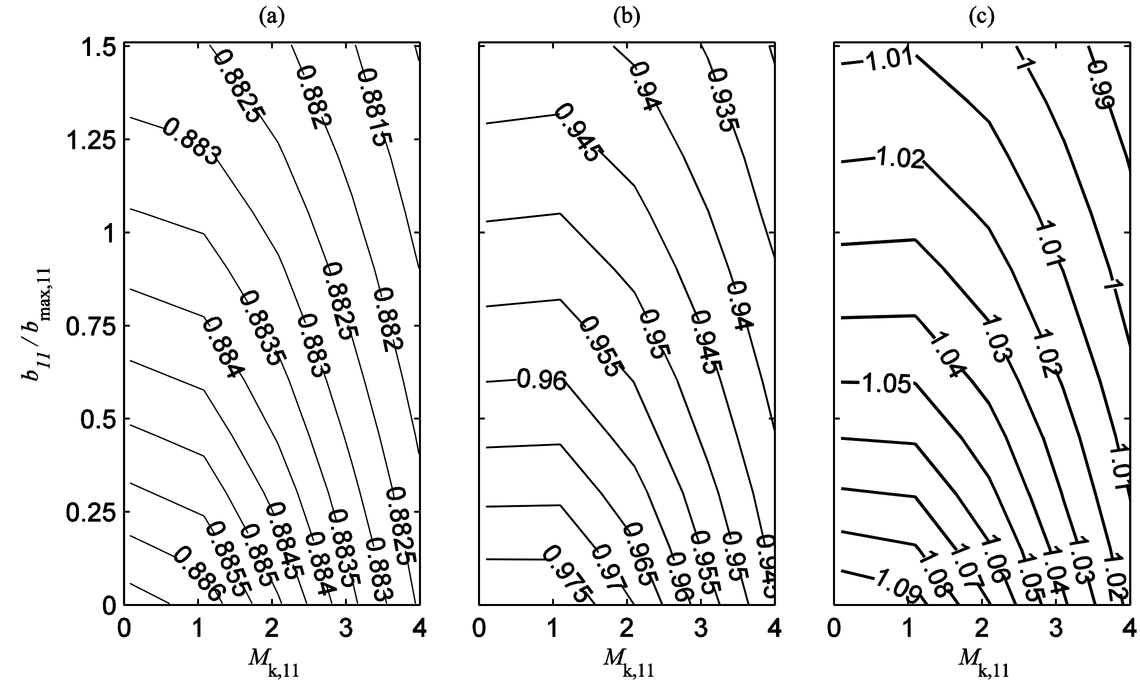

Figure 6.15 Extreme forces with 1% probability of exceedance on one rotor supported from a floating structure relative to same forces on a rigid structure. a) Wave factor K_1 =0.1. b) K_1 =0.2. c) K_1 =0.3. f = 1.05 Hz, δ = $\pm\pi$ for all cases.

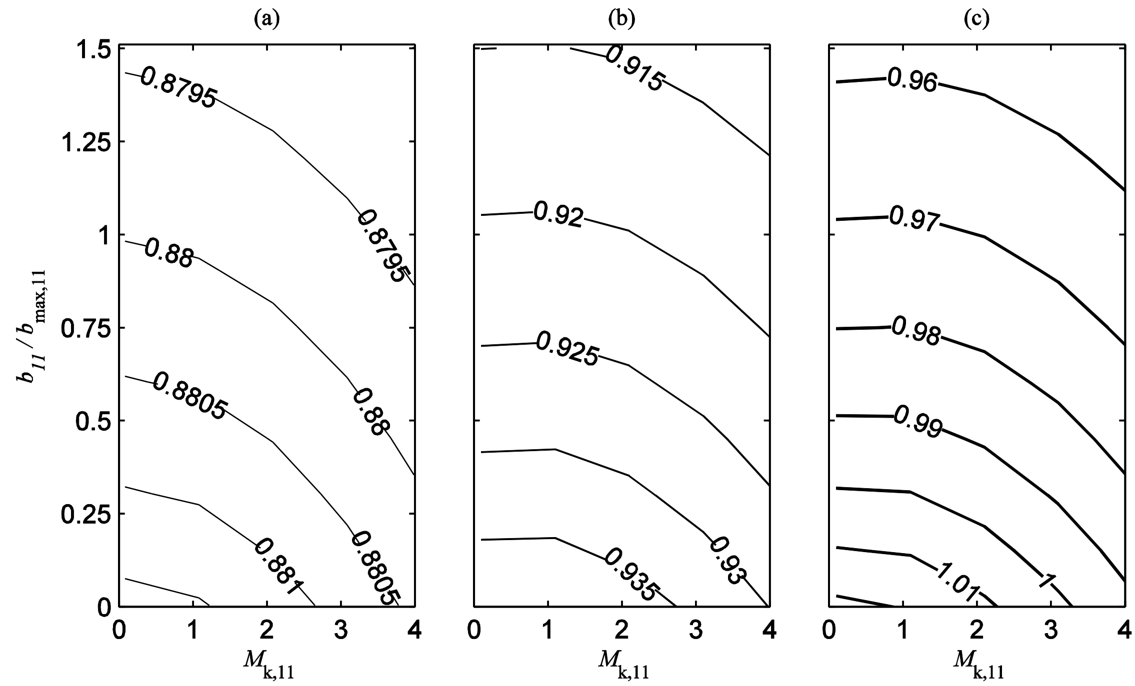

Figure 6.16 Extreme forces with 1% probability of exceedance on one of two rotors supported from a floating structure relative to same forces on a rigid structure. a) K_1 =0.1. b) K_1 =0.2. c) $K_1 = 0.3$.f =1.05 Hz, $\delta = \pm\pi$ for all cases.

The dynamic response of a floating support platform can thus reduce peak loads on a rotor under several conditions: if the amplitude of wave-induced forces is less than the rotor dynamic peak thrust, K_1<0.2, if the phase between the wave force and surface elevation is close to $\pm\pi$ radians, if more than one rotor is supported on the same platform, or if net damping associated with the supporting platform is greater than that of the averaged rotor. However, the greatest reduction of extreme force was obtained when the relative phase between the wave force and surface elevation is approaching to an anti-phase condition. The extreme forces obtained for the frequency condition with $\delta = \pm\pi$ using either one or two rotors were mostly reduced in comparison to a rigid platform. This applied for the range of damping and mass ratios considered. For a particular platform geometry, the phase of the force relative to elevation is related to the wavelength, hence a function of the wave frequency and therefore forcing in anti-phase to elevation would be limited to a narrow range of frequencies.

6.10 Coupled Pitch and Surge

A coupled model of the pitch and surge response of the supporting platform is employed to investigate the extreme load variation of the platform concept in the same representative turbulent and oscillatory flow condition. Pitch and surge of the platform define the motion of the rotor in surge only. Rearranging Eq. 6.2 for the surge and pitch coupled motion (j=1,5), the equation of motion of the support structure becomes:

$$\begin{aligned}\left(m_{11}+a_{11}+\mathrm{n}m_{\mathrm{rotor},11}\right)\ddot{x}_1+b_{11}\dot{x}_1+k_{11}x_1+a_{15}\ddot{x}_5+b_{15}\dot{x}_5 &\\ =\mathrm{n}0.08F_0+X_1 &\\ +\mathrm{n}F_{\mathrm{D},11}\left(\dot{x}_{\mathrm{rotor},1},u_{\mathrm{c}},u_{\mathrm{wave,p}}\right)+\mathrm{n}F_{\mathrm{I},11}\left(\ddot{x}_{\mathrm{rotor},1},\dot{u}_{\mathrm{c}},\dot{u}_{\mathrm{wave,p}}\right) &\\ +\mathrm{n}F_{\mathrm{D},15}\left(\dot{x}_{\mathrm{rotor},5},u_{\mathrm{c}},u_{\mathrm{wave,p}}\right)+\mathrm{n}F_{\mathrm{I},15}\left(\ddot{x}_{\mathrm{rotor},5},\dot{u}_{\mathrm{c}},\dot{u}_{\mathrm{wave,p}}\right) &\end{aligned} \quad \text{Eq. 6.29}$$

Defining surge of the rotor in terms of pitch and surge of the support:

$$\begin{aligned}\left(m_{11}+a_{11}+\mathrm{n}m_{\mathrm{rotor},11}\right)\ddot{x}_1+b_{11}\dot{x}_1+k_{11}x_1+a_{15}\ddot{x}_5+b_{15}\dot{x}_5 &\\ =\mathrm{n}0.08F_0+X_1 &\\ +\mathrm{n}F_{\mathrm{D},11}\left(\dot{x}_1,u_{\mathrm{c}},u_{\mathrm{wave,p}}\right)+\mathrm{n}F_{\mathrm{I},11}\left(\ddot{x}_1,\dot{u}_{\mathrm{c}},\dot{u}_{\mathrm{wave,p}}\right) &\\ +\mathrm{n}F_{\mathrm{D},11}\left(\dot{x}_5L,u_{\mathrm{c}},u_{\mathrm{wave,p}}\right)+\mathrm{n}F_{\mathrm{I},11}\left(\ddot{x}_5L,\dot{u}_{\mathrm{c}},\dot{u}_{\mathrm{wave,p}}\right) &\end{aligned} \quad \text{Eq. 6.30}$$

The contribution of drag and inertia of each rotor in surge motion is written as shown in Section 6.9. The time-dependent pitch equation of motion is obtained similarly to the surge by employing Eq. 6.3 with the parameters set to j=1,5 and approximating the rotor displacements with support motion as:

$$\begin{aligned}\left(m_{55}+a_{55}+\mathrm{n}m_{\mathrm{rotor},11}L^2\right)\ddot{x}_5+b_{55}\dot{x}_5+c_{55}x_5+a_{51}\ddot{x}_1+b_{51}\dot{x}_1 &\\ =\mathrm{n}0.08F_0L+X_5 &\\ +\mathrm{n}F_{\mathrm{D},11}\left(\dot{x}_5L,u_{\mathrm{c}},u_{\mathrm{wave,p}}\right)L+\mathrm{n}F_{\mathrm{I},11}\left(\ddot{x}_5L,\dot{u}_{\mathrm{c}},\dot{u}_{\mathrm{wave,p}}\right)L &\\ +\mathrm{n}F_{\mathrm{D},11}\left(\dot{x}_1,u_{\mathrm{c}},u_{\mathrm{wave,p}}\right)L+\mathrm{n}F_{\mathrm{I},11}\left(\ddot{x}_1,\dot{u}_{\mathrm{c}},\dot{u}_{\mathrm{wave,p}}\right)L &\end{aligned} \quad \text{Eq. 6.31}$$

The predictions of thrust and response amplitude of oscillation are obtained by the time-domain solution of the set of first-order differential equations of pitch and surge motion (Eq. 6.29 and Eq. 6.31) as shown in Section 6.9. The implementation and conversion of the force formulas into a set of ODE is shown in Appendix C.

The dynamic displacement and force on the rotor due to coupled surge and pitch of the support was contrasted to the force on a rigid structure as Eq. 6.18, Figure 6.16, Section 6.9. The time-varying force per rotor supported on a stiff tower due to mean current, waves and response (see Eq. 5.5 and Eq. 6.18) is:

$$F_{\text{rigid}} = \left(F_0 + \frac{1}{2}\rho A C_{\text{D}}\left|u_{\text{wave,p}}\right|\left(u_0 + \left|u_{\text{wave,p}}\right|\right) + 0.08F_0\right) \qquad \text{Eq. 6.32}$$

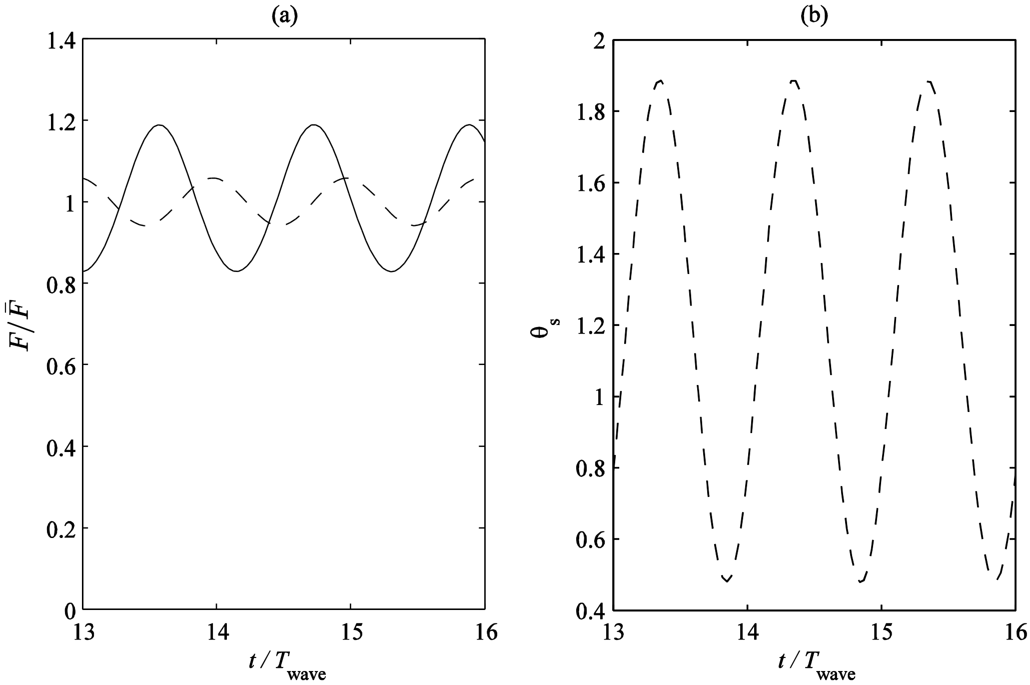

Figure 6.17 a) Force between a floating (--) and rigid-bed-connected support structure (-) without turbulence. b) Pitch oscillation in degrees for the floating support in waves opposing a mean flow (--).

For wave period of 8 s at full-scale (1.05 Hz as modelled), it was found that the range of forces, F'_{rms}, were reduced to 33% of the rms force obtained with a rotor supported on a rigid tower in the same conditions (Figure 6.17a). For this wave frequency, the pitch damping and moment exerted by the support resulted in an amplitude of angle of oscillation less than 0.8° and a 8% reduction of the 1 in a 100 forces (using Eq. 6.18) relative to a turbine on a rigid support. This suggests that the semi-submersible support structure geometry considered in Section 6.5 is a reasonable geometry due to its low wave forcing, high damping, and non-zero phase difference between force and surface elevation for the frequency range ($f = 0.7 - 1.2$ Hz). However, increasing further the frequency of operation would be detrimental to the support since damping of the support decreases for the pitch mode and the phase corresponding to the force, relative to the surface elevation, approaches to zero ($f \sim 1.5$ Hz). A design objective for support structures may thus be to select the geometry such that the phase difference between wave-excitation force and wave-induced velocity is maximum whilst wave amplitude large.

6.11 Summary

Floating support structures for wind and tidal stream turbines were reviewed. The influence of loading and response on rotor loading was identified as a design uncertainty. In this chapter the dynamic response of a rotor rigidly connected to a floating support is analysed based on the response in surge and pitch of a floating support rigidly connected to a turbine. A semi-submersible geometry studied by Van der Plas (2014) and Francis and Hamilton (2007) is simplified to a slender half-cylinder. Wave forcing, added mass and radiation damping are obtained from the diffraction code WAMIT^{TM}. The external constraint of a mooring line was modelled as a low stiffness spring. Forcing on the rotor was defined by the mean incident flow, waves and streamwise motion of the rotor as per the analysis of Chapter 4.

The effect of dynamic response on the mean, variance and peak values of rotor loading was investigated due to response in two modes: independent pitch and coupled surge and pitch and for a range of hydrodynamic coefficients, wave forces and moments. Two wave frequencies were considered with phase difference between the support platform wave force and surface elevation close to 0 and $\pm\pi$ radians. For these wave frequencies, peak thrust was reduced compared to a rigid support structure when the phase difference was $\pm\pi$ radians. Force was also reduced when the phase difference was zero if the following conditions were met: multiple rotors, net damping coefficients of at least equivalent to the rotor damping and amplitude of wave forces, K_1, below 0.2 of the dynamic rotor thrust. The extreme thrust per turbine was found to be lower for a structure supporting two rotors due to the additional damping of the rotor. For the wave condition with phase difference, the 1 in 100 exceedance force for motion in surge was found to reduce across the range of achievable hydrodynamic parameters (added mass and damping) of the support by up to 12% relative to a rotor supported on a rigid tower.

For the simplified support structure geometry modelled, the 1 in 100 exceedance force for motion in coupled surge and pitch was found to reduce by approximately 8%

due to structure dynamics when compared to the rotor response obtained from a stiff support structure.

CHAPTER 7: CONCLUSIONS

The overall aim of the thesis was to determine how the response of a floating support platform affects the loading of wind or tidal stream turbines. The particular interest was the influence of the dynamic response on the occurrence and magnitude of the maximum loads applied to the rotor of a tidal stream turbine during operation since these loads directly influence tidal system design.

It was found that the support-structure dynamics can either increase or reduce the extreme thrust of the turbine relative to the rotor response on a rigid structure, and this was dependent on the hydrodynamic damping, added mass and excitation force on the supporting platform at particular wave frequencies. A support-platform geometry that minimises peak forces on the rotor would be characterised by low wave forcing, a damping of at least equivalent to the rotor and an excitation force in anti-phase to the surface elevation. Due to the multiple wave frequencies encountered in sea states, the magnitude of the phase force from the support would then be optimised for the most representative frequency of flow operation.

To model loading coupled with response, the loading on a horizontal-axis rotor has been investigated as it responds to different types of onset flow representing the flows experienced by a rotor during operation. These included the mean and time-varying rotor loads due to an incident uniform flow, a turbulent channel flow, oscillatory incident flow due to waves opposing turbulent flow and due to sinusoidal oscillation of the rotor within quiescent flow and turbulent flow. The understanding of each effect on the turbine's performance was investigated using engineering tools such as BEMT and by experimental investigation of time variation of rotor thrust in turbulent channel flows, oscillatory flow and due to oscillation relative to a mean flow. The loading in turbulent channel flow was acquired from the variance of the rotor thrust measurements and related to the standard deviation of the operating-flow velocities. The thrust and power curves modelled with the BEMT model was obtained within 10% of the mean measured rotor performance in an operating flow with TI =12%.

Forces with probability of occurrence 1 in 100 (1%) in the mean flow with turbulence present (TI =12%) were around 140% of the mean thrust. The variation of extreme loads due to mean flow combined with turbulence and opposing waves was investigated and approximated with a Morison equation (Eq. 4.9) by ignoring inertia coefficient and accounting for the mean loading due to uniform flow, as well as the turbulent thrust fluctuations and the wave loading. The effect of waves on the rotor loading was found to increase the extreme loading as a function of relative velocity using a drag coefficient of 2 and the mean force was close to the value in turbulent channel flow.

For the wave conditions applicable to rotor operation at full scale (typically less than 3m wave height) the maximum 1% force encountered was approximately 190% of the mean thrust. The damping coefficient of a disc (using Eq. 4.5) of similar rotor thrust increased linearly with the amplitude of streamwise oscillation, KC, and the magnitude of the slope using a least-squares approach was approx. 0.15. The added mass coefficient was found to be small in comparison to the damping in all conditions studied, with magnitude approximately 0.12.

The dynamic force on a support structure was considered as a combination of the loading on the turbine due to turbulent flow and waves, loading of the turbine due to response and the direct loading on the immersed part of the supporting platform. Subsequently, the influence of the structure dynamics on the rotor thrust was analysed using wave forcing by linear analysis in an uncoupled surge-pitch structure model with the mechanical properties of the support defined as proportional to the rotor. Two wave conditions were studied with phase difference between the wave force support and the surface elevation of zero and $\pm\pi$ radians. It was found that extreme forces were reduced relative to a rigid support if the force phase difference was close to $\pm\pi$ radians. When this condition is not met, extreme forces can be reduced in the following conditions: multiple rotors, surge and pitch damping coefficients of at least the same of the rotor and with amplitudes of support forces being lower than 0.2 of the peak rotor thrust imposed in forced axial oscillations. The dynamic response applied to a typical support platform geometry due to mean flow and with wave forcing on the platform close to anti-phase with surface elevation exhibited a reduction of peak rotor force (1 in a 100) by about 8% in comparison to rotor response on a rigid bed-mounted support. The findings of rotor thrust and support structure influence are summarised below.

Mean and variance of thrust

A BEM numerical model based on wind rotor loading was shown to be suitable for the prediction of thrust and power output from a tidal stream turbine due to a steady flow. This method was evaluated against predictions for a 0.27 m rotor and a new set of experimental measurements in a mean flow with TI =12%. Evaluation was also conducted using published performance data for two tidal stream turbines of a 0.8 metre rotor diameter each (Batten et al., 2008; Galloway et al., 2011). The blockage effects on the experiments using the 0.27 m single rotor were corrected using a wind-tunnel method and found negligible for the steady-flow coefficients of thrust and power.

The thrust fluctuations normalised to the mean in the turbulent channel flows were found to increase proportionally to the turbulence intensity that is averaged across the rotor. A multiplier (admittance) factor, K_{I}, which relates the intensity of fluctuations (standard deviation over mean) between the thrust and hub-height velocity for flows corresponding to a TI =12% and TI =14% was obtained as 1.17 and 1.5. The measured thrust fluctuations in the turbulent channel flows were predicted using an aerodynamic admittance previously obtained for square plates in grid-generated turbulence. The comparison between the measurements and predictions were considered to be good due to the discrepancy of the object (rectangular plate rather than rotor) and the operating flows (grid against open channel turbulence) employed between the theoretical model and experiments.

For a single rotor, the time-average thrust obtained due to forced streamwise oscillations within a turbulent channel flow of TI =12% remained within 7% of the mean thrust that is imposed when the rotor is supported on a stiff tower and subjected to turbulent channel flows of TI =12% and TI =14% and in eighteen wave conditions opposing a turbulent channel flow of TI =12%.

Turbine Hydrodynamics

The damping of a porous disc (Eq. 4.5) oscillating in quiescent flow was a linear function Keulegan Carpenter number, KC. The drag coefficient of the disc (using Eq. 2.39) was found to decay exponentially with KC to a limiting value of 2 for KC > 1. A drag term was evaluated against measurements of force due to streamwise oscillation within turbulent flows by summing the mean thrust due to turbulent channel flow with a drag force due to streamwise oscillation about the mean velocity (Eq. 4.9, approach based on Eq. 2.49). The drag coefficient obtained for a disc and rotor oscillating in incident turbulent channel flows was found to be comparable. The drag coefficient on a disc in turbulent channel flow was within 6% of the drag obtained for a porous disc forced to oscillate in quiescent flow. The accuracy of the drag assumption was limited to $KC < 0.65$. The discrepancy was attributed to the approximation of the relative velocity between the water and disc and the neglected terms in the modified Morison force associated with turbulent fluctuations. The added mass for the disc and rotor in quiescent and turbulent channel flows was approximately constant with KC and the magnitude was approximately 12% of the virtual mass predicted for a non-perforated disc (defined by a spheroid) using potential flow theory. The effects of added mass were much lower than drag and these were found to be negligible when considering maximum rotor loading.

Extreme loading

The magnitude of the thrust on a rotor in turbulent channel flow exceeded by 1%, 0.1% and 0.01% samples was analysed using the peak-over-threshold technique with the Type 1 distribution and Pareto tail-fitting technique. The 0.01% force in turbulent channel flow only and in mean flow combined with turbulence and waves can be considered representative of the loading occurring on a full-scale turbine on average once every two days when operating in similar flow. Threshold magnitudes of 1.25 and 1.1 times the mean force were selected for the loading due to oscillatory and turbulent channel flows. A 10 minute sample measurement was found to obtain the extremes using Type 1 distribution within 3% from 30 min sample of the experimental measurement of force in turbulent channel flow and from 44 min sample of the experimental measurement of force due to turbulence channel flow with opposing waves. The 1% force was 1.38 and 1.59 times the mean thrust corresponding to the flow conditions with TI =12% and TI =14%. The prediction of loads was also analysed in terms of sample length and threshold forces by using Type 1, Normal and Weibull distributions and these provided similar extremes within 3%.

In waves opposing a turbulent channel flow, the maximum 0.01% force encountered was acquired with waves specified as 0.7 Hz and 20mm with a magnitude of

2.36 times the mean thrust. The extreme forces in the oscillatory flow conditions increased quadratically with the amplitude of wave velocity and as amplitude of velocity decreased, the initial thrust was comparable to the turbulent channel flow of $TI = 12\%$. The spectrum of the excitation force in the combined flow with small wave height was comparable to the force superposition of the ambient and wave frequency load.

A Morison equation was evaluated against the extreme force measurements in small waves by summing the load deviation in turbulent channel flow with a wave-induced force (Eq. 5.1, approach based on Eq. 2.48). Linear wave theory provided the measured velocity at hub height to within 7% for a range of wave conditions. Definition of the drag associated with wave induced velocity in terms of the square of wave velocity provides extreme force as (Eq. 5.2):

$$F_{\frac{1}{\mathrm{n}},\mathrm{wave}} = \frac{1}{2}\rho C_{\mathrm{D,wave}}\pi R^2 \|u_{\mathrm{wave}}\|^2$$

For this drag model, a thrust coefficient of 0.89 in the turbulent channel flow and drag coefficient of magnitude 11 for the wave conditions were attained. The simulated extreme force curves had initial values comparable to the exceedance load in turbulent channel flow and increased exponentially with the amplitude of the wave velocity. The extreme forces were predicted within 8% by employing linear wave prediction of velocity.

A force prediction method (approach based on Eq. 4.9) using relative velocity at hub height, defined by the product of wave velocity and wave velocity superposed with mean flow, and a drag coefficient of 2 was evaluated to obtain the extremes in forced streamwise motion tests in a turbulent channel flow. Definition of the drag force associated with the wave-induced velocity is (Eq. 5.5):

$$\frac{1}{2}\rho A C_{\mathrm{D,wave}} u_{\mathrm{wave,p}} \left|u_0 - u_{\mathrm{wave,p}}\right| = F_{\mathrm{osc,p}}$$

For this formulation the extreme forces were predicted to within 6% and asymptote to a limit as the wave velocity increases relative to the mean flow. This discrepancy is within the 7% difference between measured hub height velocity and velocity predicted by linear wave theory providing confidence in this approach for peak force prediction. This method also provides a reasonable prediction of the time-varying force due to waves with turbulence.

Effect of platform response on extreme loading

Dynamic response of a floating platform was considered in pitch and surge modes due to forcing on the turbine associated with uniform flow, turbulence, waves and streamwise oscillation of the rotor due to the response of the support structure the forcing of which is obtained by linear diffraction theory. The dynamic response in the time-dependent pitch and surge motion was studied for a typical floating platform geometry.

The simulations of dynamic response in uncoupled surge and pitch modes exhibited a reduction of the extreme loads in specific circumstances. This included when the phase magnitudes between the surface elevation and support force were close to $\pm\pi$ radians. In the condition without phase difference, greatest reduction of rotor force was achieved using multiple rotor devices in a support that produces low wave force amplitudes between support and rotor. Support platform force amplitudes of less than 20% of the mean rotor force and damping coefficients in surge and pitch of at least equal to the rotor damping reduced extreme force on the rotor. It was found that a phase difference between the wave force and the hub velocity caused cancellation of rotor drag with the wave support force and thus extremes forces with 1% probability of exceedance were reduced by up to 12% for motion in surge only.

This geometry was found beneficial by imparting low wave-support responses, damping coefficients of support over rotor plane between 0.2-1.25 and phase magnitudes close to $\pm\pi$ radians for the range of frequencies (0.7-1.2 Hz). These properties applied to a scaled floating moored platform in a wave condition with support forcing close to anti-phase with the surface elevation showed an 8% reduction of the peak load (probability of occurrence 1 in a 100) for motion in coupled pitch and surge, when compared to that acquired in a bed-mounted support.

Recommendations for future work

The last section concerns more research to be performed to further improve understanding of the dynamic performance of the rotor and the support in flow conditions representative of tidal stream sites. This includes the assessment, prediction and evaluation of the floating system response, the coupled mooring lines, the rotor performance and the solution of the time-dependent model of the floating system in 3 or more coupled degrees of freedom. These suggestions may be relevant for future investigation of cost-effective supports to be utilised in deep water.

Loading in Turbulent Channel flow Only

Extreme forces are expected to play a crucial role in capital costs of any support design and rotor force fluctuations were found to increase with the flow's turbulent intensity. However, the deployment of multiple devices is required for its feasible commercialisation and the array itself influence the local incident flow and hence turbine operation. Therefore, various aspects are encouraged such as the study of extreme forces due to array configurations at different lateral and downstream spacing, the change of thrust caused by channel blockage and evaluation of thrust coefficient against onset local flow standard deviations. Differences and advantages of rotor operation with constant torque and constant speed are also important to further address by using engineering methods such as the BEMT, Morison-based equations and experimental measurements.

Loading due to Waves and Turbulent Channel Flow

The work presented in the thesis was limited to flow conditions, which were propagated perpendicularly to the rotor swept area. Turbine design and the wide range of flow directions that occur at some tidal stream sites may require yawed operation for part of the cycle. In addition, waves are likely to be irregular with variation of dominant direction. To improve understanding of rotor loading in oblique waves and yawed onset flow, a set of experiments would be required to evaluate performance of the rotor in incident flows and irregular waves misaligned to rotor axis. Alternatively, this experimental study may be attained in another wave flume facility by generating wave conditions at different propagation angles relative to the mean flow. This finding as an input to coupled rotor response leading to multi-mode response in a floating moored platform is relevant for the design and innovation of dynamic support systems. Such information may be used to produce guidelines to cover aspects such as rotor device performance and detailed optimisation of rigid support structures in indicative tidal stream sites.

Loading due to Forced Streamwise Motion

The loading due to forced streamwise motion was investigated in perpendicular quiescent and turbulent channel flows to the rotor and the results were used as input to a model of structural dynamics. Coupled pitch and surge sinusoidal motion of the support platform were regarded as contributing to most of the rotor's variation of thrust. This result may be considered for ideal operating conditions, whereby the incoming waves are monochromatic and decay effects are small. This leads to some uncertainties of dynamic response in irregular motion and in oblique waves combined with current flows. Hence, proper tools must be first developed to understand uncoupled rotor behaviour in order to combine into a structure response model. This will require the design of stiffer oscillating support equipment to induce the total contribution of sinusoidal rotor displacement in mean flow with turbulence present and in same flow combined with waves of different directions, amplitude and wave peak frequencies. The new damping and drag parameters as a function of KC would provide a broader understanding of wave-current interactions and demonstrate key differences between rotor operation with and without forced streamwise motion.

Hydrodynamic Coefficients of the Rotor

Most of the floating supports that have been proposed are comprised of a pair of rotors so that their own thrust aligns to the incident flow and counteracts the yaw moment applied to the immersed support. Nevertheless, the yaw moment induced by the rotor in misaligned flow conditions may be large relative to the floating support. The decoupling effect of the rotor could be further explored by quantifying the rotor hydrodynamics in additional degrees of freedom such as yaw, and heave. The resulting coupled predicted motion between the turbine and platform would serve as a basis design of the mooring lines to keep system's oscillations within acceptable operation. Various aspects of mooring representations such as linear spring forces and dynamic analyses have been included for floating wind-turbine platforms (Qiao and Ou, 2014) to reduce the surge, heave and yaw induced moments (Nielsen et al., 2006; Skaare et al., 2007). Therefore, a similar approach for tidal floating supports should be appraised to limit the system's oscillations and protect against extreme conditions.

Alternative Support Structures

There is substantial work to be done to assess the cost-benefits of each support system, which are appropriate for the site characteristics, the rotor employed (wind or tidal) and the mooring system preferred. Hydrodynamic interactions and influence of rotor loading can be investigated using representative dimensions and linear wave forcing of support structure such as Tension Leg Platforms, spar systems and semi-submersible concepts. The influence of the dynamic structure can be expanded into an equation of motion to include time-dependant hydrodynamics and drift forces of the support, as well as non-linear interaction of the mooring lines and hydrodynamics of the rotor in surge, pitch and yaw motion.

Evaluation of Dynamic response

A set of experiments on simple buoy and scaled support devices in turbulent channel flow combined with waves will be needed to quantify the moments and the hydrodynamic coefficients as well as to evaluate the suitability of WAMIT™. Prediction methods of the moored dynamic support will be validated against measurements. This study will lead to the development of a fully coupled model for the design, and the assessment of life support and improvement of the current marine offshore platforms technology.

References

ABPmer, The Met Office & Proudman Oceanographic Laboratory (2004), "Atlas of UK Marine Renewable Energy Resources". Technical report R.1106, *September 2004*.

Afgan I., McNaughton, J., Rolfo, S., Apsley, D., Stallard, T., and Stansby, P. (2013), "Turbulent Flow and Loading on a Tidal Stream Turbine by LES and RANS", *International Journal of Heat and Fluid Flow*, 43, 96-108.

An, S., and Faltinsen, O. M. (2013), "An Experimental and Numerical Study of Heave Added Mass and Damping of Horizontally Submerged and Perforated Rectangular Plates", *Journal of Fluids and Structures*, 39, 87-101.

Atlantis Resources Ltd. URL http://atlantisresourcesltd.com/

Bahaj, A., Myers, L., Rawlinson-Smith, R., and Thomson, M. (2012), "The Effect of Boundary Proximity Upon the Wake Structure of Horizontal Axis Marine Current Turbines", *Journal of Offshore Mechanics and Arctic Engineering*, 134, 021104.

Bahaj, A. S., Batten, W. M. J., and McCann, G. (2007), "Experimental Verifications of Numerical Predictions for the Hydrodynamic Performance of Horizontal Axis Marine Current Turbines", *Renewable Energy*, 32, 2479-2490.

Bahaj, A. S., Molland, A. F., Chaplin, J. R., and Batten, W. M. J. (2007), "Power and Thrust Measurements of Marine Current Turbines under Various Hydrodynamic Flow Conditions in a Cavitation Tunnel and a Towing Tank", *Renewable Energy*, 32, 407-426.

Barltrop, N., Varyani, K. S., Grant, A., Clelland, D., and Pham, X. P. (2007), "Investigation into Wave-Current Interactions in Marine Current Turbines", *Proceedings of the Institution of Mechanical Engineers, Part A: Journal of Power and Energy*, 221, 233-242.

Batten, W. M., Harrison, M., and Bahaj, A. (2013), "Accuracy of the Actuator Disc-Rans Approach for Predicting the Performance and Wake of Tidal Turbines", *Philosophical Transactions of the Royal Society A: Mathematical, Physical and Engineering Sciences*, 371, 20120293.

Batten, W. M. J., Bahaj, A. S., Molland, A. F., and Chaplin, J. R. (2007), "Experimentally Validated Numerical Method for the Hydrodynamic Design of Horizontal Axis Tidal Turbines", *Ocean Engineering*, 34, 1013-1020.

Batten, W. M. J., Bahaj, A. S., Molland, A. F., and Chaplin, J. R. (2008), "The Prediction of the Hydrodynamic Performance of Marine Current Turbines", *Renewable Energy*, 33, 1085-1096.

Bearman, P. W. (1971), "An Investigation of the Forces on Flat Plates Normal to Turbulent Flow", *Journal of Fluid Mechanics*, 46, 177-198.

Ben Elghali, S., Benbouzid, M., and Charpentier, J. F. (2007), "Marine Tidal Current Electric Power Generation Technology: State of the Art and Current Status", *Electric Machines & Drives Conference, (IEMDC 07), IEEE International*, IEEE, 2. 1407-1412.

Berthelsen, P. A., and Fylling, I. (2011), "Optimization of Floating Support Structures for Deep Water Wind Turbines", *EWEA 2011, 14-17 March, Brussels, Belgium*.

Black & Veatch Ltd. (2005), "Tidal Stream Energy Resource and Technology Summary Report".Technical Report 107799/D/2200/04, Carbon Trust, London.

Black & Veatch Ltd. (2011), "UK Tidal Current Resource and Economics Study". Technical Report 121393, Carbon Trust, London.

Blackmore, T., Batten, W. J., Műller, G., and Bahaj, A. (2013), "Influence of Turbulence on the Drag of Solid Discs and Turbine Simulators in a Water Current", *Experiments in Fluids*, 55, 1-10.

Blackmore, T., Batten, W. M. J., and Bahaj, A. S. (2014), "Influence of Turbulence on the Wake of a Marine Current Turbine Simulator", *Proceedings of the Royal Society of London A: Mathematical, Physical and Engineering Sciences*, 470, 20140331.

Blanchfield, J., Garrett, C., Rowe, A., and Wild, P. (2008), "Tidal Stream Power Resource Assessment for Masset Sound, Haida Gwaii", *Proceedings of the Institution of Mechanical Engineers, Part A: Journal of Power and Energy*, 222, 485-492.

Blasques, J. P., and Natarajan, A. (2013), "Mean Load Effects on the Fatigue Life of Offshore Wind Turbine Monopile Foundations", *International Conference on Computational Methods in Marine Engineering*, *29-31 May* 2013, *Hamburg, Germany*.

Blunden, L. S., and Bahaj, A. S. (2007), "Tidal Energy Resource Assessment for Tidal Stream Generators", *Proceedings of the Institution of Mechanical Engineers, Part A: Journal of Power and Energy*, 221, 137-146.

Bossanyi, E. A. (2007), *GH Tidal Bladed Theory Manual*. GH & Partners Ltd.

Bowditch, N. (2002), *The American Practical Navigator: An Epitome of Navigation* (Bicentenial ed.), National Imagery and Mapping Agency.

Brabson, B., and Palutikof, J. (2000), "Tests of the Generalized Pareto Distribution for Predicting Extreme Wind Speeds", *Journal of Applied Meteorology*, 39, 1627-1640.

Brouwers, J. J. H., and Verbeek, P. H. J. (1983), "Expected Fatigue Damage and Expected Extreme Response for Morison-Type Wave Loading", *Applied Ocean Research*, 5, 129-133.

Bryden, I. G., and Couch, S. J. (2006), "ME1-Marine Energy Extraction: Tidal Resource Analysis", *Renewable Energy*, 31, 133-139.

Buckland, H. C., Masters, I., Chapman, J. C. and Orme, J.A.C. (2010), "Blade Element Momentum Theory in Modelling Tidal Stream Turbines", *18th UK Conference on Computational Mechanics (ACME-UK), 29-31 March, Southampton, UK*.

Buhl, M. L. (2005), "A New Empirical Relationship Between Thrust Coefficient and Induction Factor for the Turbulent Windmill State", Technical Report No. NREL/TP-500-36834. National Renewable Energy Laboratory

Burrows, R., Yates, N., Hedges, T., Li, M., Zhou, J., Chen, D., Walkington, I., Wolf, J., Holt, J., and Proctor, R. (2009), "Tidal Energy Potential in UK Waters", *Proceedings of the ICE-Maritime Engineering*, 162, 155-164.

Burton, T., Sharpe, D., Jenkins, N., and Bossanyi, E. (2001), *Wind Energy Handbook*, John Wiley & Sons.

Butterfield, C. P., Musial, W., Jonkman, J., Sclavounos, P., and Wayman, L. (2007), "Engineering Challenges for Floating Offshore Wind Turbines", National Renewable Energy Laboratory. *Copenhagen Offshore Wind Conference, 26-28 October, Copenhagen, Denmark*.

Carballo, R., Iglesias, G., and Castro, A. (2009), "Numerical Model Evaluation of Tidal Stream Energy Resources in the Ría De Muros (Nw Spain)", *Renewable Energy*, 34, 1517-1524.

Chapman, J. C., Masters, I., Togneri, M., and Orme, J. A. C. (2013), "The Buhl Correction Factor Applied to High Induction Conditions for Tidal Stream Turbines", *Renewable Energy*, 60, 472-480.

Chakrabarti, S. K. (1987), *Hydrodynamics of Offshore Structures*, WIT Press.

Cheng-Han, T., Young.-Zher, K., Dong-Jiing, D., Hsien-Wen, L., Nan-Jung, K., Shih-Jen, H., Yao-Tsai, L., Hung-Jen, L. and Sin-Jye L.. (2012), "Development and Testing of a Tidal Stream Device for the Sea near Keelung, Taiwan", *4th International Conference on Ocean Energy*, *October 17-19, Dublin, Ireland*.

Churchfield, M. J., Li, Y., and Moriarty, P. J. (2013), "A Large-Eddy Simulation Study of Wake Propagation and Power Production in an Array of Tidal-Current Turbines", *Philosophical Transactions of the Royal Society A: Mathematical, Physical and Engineering Sciences*, 371, 20120421.

Clarke, J., Connor, G., Grant, A., Johnstone, C., and Ordonez-Sanchez, S. (2009), "Contra-Rotating Marine Current Turbines: Single Point Tethered Floating System-Stabilty and Performance", *8th European Wave and Tidal Energy Conference, EWTEC 2009*, 7-10 *September, Uppsala, Sweden*.

Clarke, J., Connor, G., Grant, A., Johnstone, C., and Ordonez-Sanchez, S. (2010), "Analysis of a Single Point Tensioned Mooring System for Station Keeping of a Contra-Rotating Marine Current Turbine", *Renewable Power Generation, IET*, 4, 473-487.

Coles, S., Bawa, J., Trenner, L., and Dorazio, P. (2001), *An Introduction to Statistical Modeling of Extreme Values*, Vol 208. London: Springer.

Crasto, G., Gravdahl, A. R., Castellani, F., and Piccioni, E. (2012), "Wake Modeling with the Actuator Disc Concept", *Energy Procedia*, 24, 385-392.

De Vries, W., and Krolis, V. (2007), "Effects of Deep Water on Monopile Support Structures for Offshore Wind Turbines", *European Wind Energy Conference & Exhibition (EWEC), 7-10 May, Milan, Italy*.

DEA/CADDET (2000), "Electricity from Offshore Wind". Danish Energy Agency and Iea Caddet Renewable Energy Programme, ETSU, Harwell UK.

Dean, R. G., and Dalrymple, R. A. (1991), *Water Wave Mechanics for Engineers and Scientists* (2nd printing with corrections. ed.),Singapore. London: World Scientific.

Det Norske Veritas (DNV) (2007), "Design of Offshore Wind Turbine Structures", *Offshore Standard DNV-OS-J101*, 142.

De Silva, C. W. (2010), *Vibration and Shock Handbook*, CRC Press.

Downie, M. J., Graham, J. M. R., Hall, C., Incecik, A., and Nygaard, I. (2000), "An Experimental Investigation of Motion Control Devices for Truss Spars", *Marine Structures*, 13, 75-90.

Draper, S., Stallard, T., Stansby, P., Way, S., and Adcock, T. (2013), "Laboratory Scale Experiments and Preliminary Modelling to Investigate Basin Scale Tidal Stream Energy Extraction", *10th European Wave and Tidal Energy Conference (EWTEC), 2-5 September, Aalborg, Denmark*.

Edmunds, M., Malki, R., Williams, A., Masters, I., and Croft, T. (2014), "Aspects of Tidal Stream Turbine Modelling in the Natural Environment using a Coupled BEM-CFD Model", *International Journal of Marine Energy*, 7, 20-42.

Embrechts, P., Klüppelberg, C., and Mikosch, T. (1997), *Modelling Extremal Events* (Vol. 33). Springer Science & Business Media.

ETSU (1993), "Tidal Stream Energy Review", Technical Report ETSU-T-05/00155/Rep. Harwell Laboratory, Energy Technology Support Unit, DTI.

Fallon, D., Hartnett, M., Olbert, A., and Nash, S. (2014), "The Effects of Array Configuration on the Hydro-Environmental Impacts of Tidal Turbines", *Renewable Energy*, 64, 10-25.

Faltinsen, O. (1993), *Sea Loads on Ships and Offshore Structures* (Vol. 1), Cambridge University Press.

Faudot, C., and Dahlhaug, O. G. (2012), "Prediction of Wave Loads on Tidal Turbine Blades", *Energy Procedia*, 20, 116-133.

Feng, A., Chen, Z., You, Y., and Xing, J. T. (2012), "Hydrodynamic Evaluation for Spar Platform Subjected to Mooring Line Failure", *The Twenty-second International Offshore and Polar Engineering Conference*, *17-23 June, Rhodes, Greece*.

Fernandez-Rodriguez, E., Stallard, T., and Stansby, P. K. (2014), "Experimental Study of Extreme Thrust on a Tidal Stream Rotor Due to Turbulent Flow and with Opposing Waves", *Journal of Fluids and Structures*.51,354-36.

Fernandez-Rodriguez, E., Stallard, T. and Stansby, P.K. (2013), "Influence of Support Structure Response on Extreme Loading of a Tidal Turbine Due to Turbulent Flow and Waves", *Proceedings of the 2nd Oxford Tidal Energy Workshop (OTE), 18-19 March 2013, Oxford, UK*.

Fraenkel, P. (2010), "Practical Tidal Turbine Design Considerations: A Review of Technical Alternatives and Key Design Decisions Leading to the Development of the Seagen 1.2 MW Tidal Turbine", *Proceedings–Fluid Machinery Group–Ocean Power Fluid Machinery Seminar, 19 October, London, UK*.

Francis, M., and Hamilton, M. (2007), "SRTT Floating Tidal Turbine Production Design Study with Independent Verification", Submitted to *Department for Business: Enterprise and Regulatory Reform*.

Freebury, G., and Musial, W. D. (2000), "Determining Equivalent Damage Loading for Full-Scale Wind Turbine Blade Fatigue Tests", *National Renewable Energy Laborator*y.

Furness, R. W., Wade, H. M., Robbins, A. M., and Masden, E. A. (2012), "Assessing the Sensitivity of Seabird Populations to Adverse Effects from Tidal Stream Turbines and Wave Energy Devices", *ICES Journal of Marine Science: Journal du Conseil*, 69, 1466-1479.

Galloway, P. (2013), "*Performance Quantification of Tidal Turbines Subjected to Dynamic Loading*". Doctoral dissertation. University of Southampton.

Galloway, P., Myers, L., and Bahaj, A. (2010), "Studies of a Scale Tidal Turbine in Close Proximity to Waves", *3rd International Conference on Ocean Energy, 6 October, Bilbao, Spain*.

Galloway, P. W., Myers, L. E., and Bahaj, A. S. (2011), "Experimental and Numerical Results of Rotor Power and Thrust of a Tidal Turbine Operating at Yaw and in Waves", *Proceedings of the Renewable Energy Congress, Marine and Ocean Technology*. 2246-2253.

Gao, Z., and Moan, T. (2009), "Mooring System Analysis of Multiple Wave Energy Converters in a Farm Configuration", *Proc. of the 8th European Wave and Tidal Energy Conference (EWTEC), 7-10 September, Uppsala, Sweden*.

Garret, C., and Cummins, P. (2007), "The Efficiency of a Turbine in a Tidal Channel", *Journal of Fluid Mechanics*, 588, 243-251.

Gooch, S., Thomson, J., Polagye, B., and Meggitt, D., (2009), "Site Characterization for Tidal Power", *OCEANS 2009, MTS/IEEE Biloxi-Marine Technology for Our Future: Global and Local Challenges*, *26-29 October, Biloxi, MS*.

Grogan, D. M., Leen, S. B., Kennedy, C. R., and Ó Brádaigh, C. M. (2013), "Design of Composite Tidal Turbine Blades", *Renewable Energy*, 57, 151-162.

Gunn, K., and Stock-Williams, C. (2013), "On Validating Numerical Hydrodynamic Models of Complex Tidal Flow", *International Journal of Marine Energy*, 3–4, 82-97.

Hansen, M. O. L. (2012), *Aerodynamics of Wind Turbines*, Routledge Taylor & Francis.

Harding, S., Thomson, J., Polagye, B., Richmond, M., Durgesh, V., and Bryden, I. (2011), "Extreme Value Analysis of Tidal Stream Velocity Perturbations", *Proceedings of the 9th European Wave and Tidal Energy Conference*, *5-9 September, Southampton, UK*.

Hardisty, J. (2009), *The Analysis of Tidal Stream Power*, John Wiley and Sons.

Harrald, M., Aires, C., and Davies, I. A. N. (2010), "Further Scottish Leasing Round (Saltire Prize Projects): Regional Locational Guidance", Ed. Marine Scotland Science.

Harrison, M., Batten, W., and Bahaj, A. (2010), "A Blade Element Actuator Disc Approach Applied to Tidal Stream Turbines", *OCEANS 2010*, *20-23 September, Seattle, WA*.

Harrison, M., Batten, W., Myers, L., and Bahaj, A. (2010), "Comparison between CFD Simulations and Experiments for Predicting the Far Wake of Horizontal Axis Tidal Turbines", *IET Renewable Power Generation*, 4, 613-627.

Hassan, U. (1982), "A Wind Tunnel Investigation of the Wake Structure within Small Wind Turbine Farms". Produced by *ETSU WN 5113, DTI, contractor Garrad Hassan & partners*.

Hayman, J., Fiore, F., and Trarieux, F. (2013), "IFREMER Tank Testing November & December 2012", Marine Renewables Infrasctructure Network for emerging Technology Technologies (MARINET).

He, H., Troesch, A. W., and Perlin, M. (2008), "Hydrodynamics of Damping Plates at Small KC Numbers", *IUTAM Symposium on Fluid-Structure Interaction in Ocean Engineering*, *Springer*, *23-26 July, Hamburg, Germany*.

Henderson, A. R., Argyriadis, K., Nichols, J., and Langston, D. (2010), "Offshore Wind Turbines on TLPs–Assessment of Floating Support Structures for Offshore Wind Farms in German Waters", *10th German wind energy conference, 17-18, November, Bremen, Germany*.

Hsu, H. P. (1996), *Theory and Problems of Probability, Random Variables, and Random Processes*, McGraw-Hill.

IEC61400-3 (2009), "Wind turbines-Part3: Design Requirements for Offshore Wind Turbines", International Electrotechnical Commission (IEC), Genève, Switzerland.

Jancauskas, E. D., and Melbourne, W. H. (1983), "The Aerodynamic Admittance of a Slender Box Girder Bridge Section", *8th Australasian Fluid Mechanics Conference, 28 November-2 December, Newcastle, Australia*.

Jensen, J. J., Olsen, A. S., and Mansour, A. E. (2011), "Extreme Wave and Wind Response Predictions", *Ocean Engineering*, 38, 2244-2253.

Jonkman, J. M., and Buhl Jr, M. L. (2007), "Development and Verification of a Fully Coupled Simulator for Offshore Wind Turbines", *45th AIAA Aerospace Sciences Meeting and Exhibit. 8–11 January 2007, Reno, USA. AIAA Meeting Papers on Disc*.

Journée, J. M. J., and Massie, W. W. (2001), *Offshore Hydromechanics* (First ed.).TU Delft.

Karimirad, M., and Moan, T. (2010), "Effect of Aerodynamic and Hydrodynamic Damping on Dynamic Response of a Spar Type Floating Wind Turbine", *European Wind Energy Conference (EWEC), April 2010, Warsaw, Poland*.

Karsten, R., McMillan, J., Lickley, M., and Haynes, R. (2008), "Assessment of Tidal Current Energy in the Minas Passage, Bay of Fundy", *Proceedings of the Institution of Mechanical Engineers, Part A: Journal of Power and Energy*, 222, 493-507.

Kawase, M., Beba, P. and Fabien, B.C. (2011) "Finding an Optimal Placement Depth for a Tidal in-Stream Energy Conversion Device in an Energetic, Baroclinic Tidal Channel". Report number 7. Northwest National Marine Renewable Energy Center.

Kelly, S. G. (2011), *Mechanical Vibrations: Theory and Applications*, Cengage Learning.

Keysan, O., McDonald, A., Mueller, M., Doherty, R., and Hamilton, M. (2010), "C-GEN, a Lightweight Direct Drive Generator for Marine Energy Converters", *Power Electronics, Machines and Drives (PEMD 2010), 5th IET International Conference on System Safety, 18-20 October, Manchester, UK*. IET. 1-6.

Kollu, R., Rayapudi, S. R., Narasimham, S., and Pakkurthi, K. M. (2012), "Mixture Probability Distribution Functions to Model Wind Speed Distributions", *International Journal of Energy and Environmental Engineering*, 3, 27.

Kurian, V., Wong, B., and Montasir, O. (2008), "Frequency Domain Analysis of Truss Spar Platform", *International Conference on Construction and Building Technology,* 5, 11-13.

Lake, M., Troesh, A. W., Perlin, M., and Thiagarajan, K. P. (2000), "Scaling Effects in Hydrodynamic Coefficient Estimation of TLP and Spar Structures", *Journal Offshore Mech and Artic Eng*., 122, 118-124.

Laura, C.-S., and Vicente, D.-C. (2014), "Life-Cycle Cost Analysis of Floating Offshore Wind Farms", *Renewable Energy*, 66, 41-48.

Lee, Y.-L. (2005), *Fatigue Testing and Analysis: Theory and Practice* (Vol. 13), Butterworth-Heinemann.

Lee, C.-H., Newman, J., and Nielsen, F. (1996), "Wave Interactions with an Oscillating Water Column", *The Sixth International Offshore and Polar Engineering Conference, May 26-31, Los Angeles, USA*.

Lee, C., and Newman, J. (2006), "Wamit® User Manual, Versions 6.3, 6.3 Pc, 6.3 S, 6.3 S-Pc", *WAMIT, Inc., Chestnut Hill, MA, USA*.

Lee, J. H., Kim, D. H., Rhee, S. H., Do, I. R., Shin, B. C., and Kim, M. C. (2011), "Computational and Experimental Analysis for Horizontal Axis Marine Current Turbine Design", *Second International Symposium on Marine Propulsors, 15-17 June, Hamburg, Germany*.

Lehmann, L. (2007), *Wave Propagation in Infinite Domains: with Applications to Structure Interaction* (Vol. 31). Springer Science & Business Media.

Leishman, J. G. (2006), *Principles of Helicopter Aerodynamics with CD Extra*, Cambridge University Press.

Lewis, M., Neill, S., and Hashemi, R. (2014), "Realistic Wave Conditions and their Influence on Quantifying the Tidal Stream Energy Resource", *Applied Energy*, 136, 495-508.

Luznik, L., Flack, K. A., Lust, E. E., and Taylor, K. (2013), "The Effect of Surface Waves on the Performance Characteristics of a Model Tidal Turbine", *Renewable Energy*, 58, 108-114.

Maniaci, D. C., and Li, Y. (2011), "Investigating the Influence of the Added Mass Effect to Marine Hydrokinetic Horizontal-Axis Turbines Using a General Dynamic Wake Wind Turbine Code", *OCEANS. 19-22, September, Waikoloa, HI*. IEEE, 1-6.

Manwell, J. F., McGowan, J. G., and Rogers, A. L. (2002), *Wind Energy Explained: Theory, Design and Application*, John Wiley & Sons, Ltd. 577p.

Marine Current Turbines Ltd. (MCT) URL http://marineturbines.com/

Masters, I., Chapman, J., Orme, J., and Willis, M. (2011), "A Robust Blade Element Momentum Theory Model for Tidal Stream Turbines Including Tip and Hub Loss Corrections", *Journal of Marine Engineering and Technology*, 10, 25-35.

McAdam, R., Houlsby, G., Oldfield, M., and McCulloch, M. (2010), "Experimental Testing of the Transverse Horizontal Axis Water Turbine", *Renewable Power Generation, IET*, 4, 510-518.

McCann, G. N. (2007), "Tidal Current Turbine Fatigue Loading Sensitivity to Waves and Turbulence- a Parametric Study", *Proceedings of the 7th European Wave and Tidal Energy Conference, 11-14 September, Porto, Portugal*.

McCann, G., Hitchcock, S., and Lane, S. (2008), "Implications of Site-Specific Conditions on the Prediction of Loading and Power Performance of a Tidal Stream Device St Vincent ' S Works", *2nd International Conference on Ocean Energy, 15-17 October, Brest, France*.

McCann, G. N., Rawlinson-Smith, R. I., and Argyriadis, K. (2006), "Load Simulation for Tidal Turbines Using Wind Turbine Experience", *International Conference of Ocean Energy, 23-24 October, Bremenhaven, Germany*.

McNae, D. M., and Graham, J. M. R. (2014), "Effects of Dynamic Inflow and Distortion of Incident Turbulence on Tidal Turbine Rotors", *3rd Oxford Tidal Energy Workshop, 7-8 April, Oxford, UK*.

McNaughton, J., Rolfo, S., Apsley, D., Afgan, I., Stallard, T., and Stansby, P. (2012), "CFD Prediction of Turbulent Flow on an Experimental Tidal Stream Turbine Using RANS Modelling", *Power*, 1, 0-3.

Milne, I. A., Day, A. H., Sharma, R. N., Flay, R. G. J., and Bickerton, S. (2011), "Tidal Turbine Blade Load Experiments for Oscillatory Motion", *Proceedings of the 9th European Wave and Tidal Energy Conference, 5-9 September, Southampton, U.K*.

Milne, I., Sharma, R., Flay, R., and Bickerton, S. (2013), "Characteristics of the Turbulence in the Flow at a Tidal Stream Power Site", *Philosophical Transactions of the Royal Society A: Mathematical, Physical and Engineering Sciences*, 371, 20120196.

Molin, B. (2001), "On the Added Mass and Damping of Periodic Arrays of Fully or Partially Porous Disks", *Journal of Fluids and Structures*, 15, 275-290.

Molin, B., and Nielsen, F. (2004), "Heave Added Mass and Damping of a Perforated Disk Below the Free Surface", *Workshop on Water Waves and floating Bodies, 28-31 March, Cortona, Italy*.

Montasir, O. A., and Kurian, V. J. (2011), "Effect of Slowly Varying Drift Forces on the Motion Characteristics of Truss Spar Platforms", *Ocean Engineering*, 38, 1417-1429.

Morgan, E. C., Lackner, M., Vogel, R. M., and Baise, L. G. (2011), "Probability Distributions for Offshore Wind Speeds", *Energy Conversion and Management*, 52, 15-26.

Moriarty, P. J., and Hansen, A. C. (2005), *Aerodyn Theory Manual*, National Renewable Energy Laboratory. *Golden, Colorado, USA*.

Moriarty, P. J., Holley, W., and Butterfield, C. P. (2004), "Extrapolation of Extreme and Fatigue Loads Using Probabilistic Methods", Technical Report No. NREL/TP-500-34421. National Renewable Energy Laboratory (NREL).

Morison, J., Johnson, J., and Schaaf, S. (1950), "The Force Exerted by Surface Waves on Piles", *Journal of Petroleum Technology*, 2, 149-154.

Musial, W., Butterfield, S., and Boone, A. (2004), "Feasibility of Floating Platform Systems for Wind Turbines", *23rd ASME Wind Energy Symposium, 5-8 January, Reno, NV*.

Musial, W., and Ram, B. (2010), "Large-Scale Offshore Wind Power in the United States: Assessment of Opportunities and Barriers". Technical Report No. NREL/TP-500-40745, National Renewable Energy Laboratory (NREL).

Mycek, P., Gaurier, B., Germain, G., Pinon, G., and Rivoalen, E. (2014), "Experimental Study of the Turbulence Intensity Effects on Marine Current Turbines Behaviour. Part I: One Single Turbine", *Renewable Energy*, 66, 729-746.

Myers, L., and Bahaj, A. S. (2006), "Wake Studies of a 1/30th Scale Horizontal Axis Marine Current Turbine", *Ocean Engineering*, 34, 758-762.

Myers, L., Bahaj, A., Germain, G., and Giles, J. (2008), "Flow Boundary Interaction Effects for Marine Current Energy Conversion Devices", *World Renewable Energy Congress X, 19-25 July, Glasgow,UK*.

Myers, L., Shah, K., and Galloway, P. (2013), "Design, Commissioning and Performance of a Device to Vary the Turbulence in a Recirculating Flume", *10th European Wave and Tidal Energy Conference, 2-5 September, Aalborg, Denmark*.

Naess, A. (1983), "Prediction of Extremes of Morison-Type Loading—an Example of a General Method", *Ocean Engineering*, 10, 313-324.

Nakamura, T., Kaneko, S., Inada, F., Kato, M., Ishihara, K., Nishihara, T., and Mureithi, N. W. (2013), *Flow-Induced Vibrations: Classifications and Lessons from Practical Experiences*, Elsevier Science.

Neill, S. P., Litt, E. J., Couch, S. J., and Davies, A. G. (2009), "The Impact of Tidal Stream Turbines on Large-Scale Sediment Dynamics", *Renewable Energy*, 34, 2803-2812.

Nelson, V. (2009), *Wind Energy: Renewable Energy and the Environment*, Taylor & Francis.

Nielsen, F. G., Hanson, T. D., and Skaare, B. (2006), "Integrated Dynamic Analysis of Floating Offshore Wind Turbines", *25th International Conference on Offshore Mechanics and Arctic Engineering*, 671-679. *4-9 June, Hamburg,Germany*. American Society of Mechanical Engineers.

Nishino, T., and Willden, R. H. (2012), "The Efficiency of an Array of Tidal Turbines Partially Blocking a Wide Channel", *Journal of Fluid Mechanics*, 708, 596-606.

NOAA, National Oceanic and Atmospheric Administration:United States Department of Commerce. URL http://www.noaa.gov/.

Norris, J. V., and Droniou, E. (2007), "Update on EMEC Activities, Resource Description and Characterisation of Wave-Induced Velocities in a Tidal Flow", *Proceedings of the 7th European Wave and Tidal Energy Conference*, *11-14 September, Porto, Portugal*.

Norton, M. P., and Karczub, D. G. (2003), *Fundamentals of Noise and Vibration Analysis for Engineers*. Cambridge University Press.

Olczak A., Stallard T., Stansby P. K. (2013), "The Influence of Waves on Tidal Stream Turbine Wake Recovery", *10th European Wave and Tidal Energy Conference, 2-5 September, Aalborg, Denmark*.

Ormel, J. A. C., and Masters, I. (2006), "Analysis and Comparison of Support Structure Concepts for Tidal Stream Turbines", *Proceedings World Maritime Technology Conference*, *6-10 March, London, UK*.

Papoulis, A., and Pillai, S. U. (2002), *Probability, Random Variables, and Stochastic Processes*. Tata McGraw-Hill Education.

Perrin, O., Rootzén, H., and Taesler, R. (2006), "A Discussion of Statistical Methods Used to Estimate Extreme Wind Speeds", *Theoretical and Applied Climatology*, 85, 203-215.

Phillips, O. M. (1977), *The Dynamics of the Upper Ocean*, Cambridge University Press, London.

Pitt, D. M., and Peters, D. A. (1981), "Theoretical Prediction of Dynamic-Inflow Derivatives", *Vertica*, 5, 21-34.

Polagye, B., and Thomson, J., (2013), "Tidal Energy Resource Characterization: Methodology and Field Study in Admiralty Inlet, Puget Sound, US", *Proceedings of the Institution of Mechanical Engineers, Part A: Journal of Power and Energy*.

Qiao, D., and Ou, J. (2014), "Mooring Line Damping Estimation for a Floating Wind Turbine", *The Scientific World Journal*, 2014, 10.

Rho, J. B., Choi, H. S., Lee, W., Shin, H., and Park, I. (2002), "Heave and Pitch Motions of a Spar Platform with Damping Plate", *Proceedings of the 12th International Offshore and Polar Engineering Conference,* 198-201, *26-31 May 2002, Kitakyushu, Japan*.

Roddier, D., and Cermelli, C. (2014), "Floating Wind Turbine Platform with Ballast Control and Mooring System". U.S. Patent Application 14/218,805, filed March 18, 2014.

Sadeghi, K., Incecik, A., and Downie, M. J. (2004), "Response Analysis of a Truss Spar in the Frequency Domain", *Journal of Marine Science and Technology*, 8, 126-137.

Salzmann, D., and Van der Tempel, J. (2005), "Aerodynamic Damping in the Design of Support Structures for Offshore Wind Turbines", *Paper of the Copenhagen Offshore Conference, 26-28 October, Copenhagen, Denmark*.

Sarpkaya, T., and Isaacson, M. (1981), *Mechanics of Wave Forces on Offshore Structures*, Van Nostrand Reinhold Co.

Schabenberger, O., and Pierce, F. J. (2001), *Contemporary Statistical Models for the Plant and Soil Sciences,* CRC Press.

Scotrenewable Tidal Power Ltd., URL http://www.scotrenewables.com/

Sedaghat, A., and Mirhosseini, M. (2012), "Aerodynamic Design of a 300 kW Horizontal Axis Wind Turbine for Province of Semnan", *Energy Conversion and Management*, 63, 87-94.

Simiu, E., Heckert, N. A., Filliben, J. J., and Johnson, S. K. (2001), "Extreme Wind Load Estimates Based on the Gumbel Distribution of Dynamic Pressures: An Assessment", *Structural Safety*, 23, 221-229.

Sirnivas, S., Musial, W., Bailey, B., and Filippelli, M. (2014), "Assessment of Offshore Wind System Design, Safety, and Operation Standards", Technical Report No NREL/TP-500-60573, National Renewable Energy Laboratory (NREL), Golden, CO.

Skaare, B., Hanson, T. D., Nielsen, F. G., Yttervik, R., Hansen, A. M., Thomsen, K., and Larsen, T. J. (2007), "Integrated Dynamic Analysis of Floating Offshore Wind Turbines", *2007 European Wind Energy Conference and Exhibition (EWEC), 7-10 May, Milan, Italy*.

Stansby, P. K., Devaney, L. C., and Stallard, T. J. (2013), "Breaking Wave Loads on Monopiles for Offshore Wind Turbines and Estimation of Extreme Overturning Moment", *Renewable Power Generation,* IET, 7 No 5.

Sumer, B. M., and Fredsøe, J. (2006), *Hydrodynamics around Cylindrical Strucures*, World Scientific Publishing.

Sun, X., Bryden, I. G., Jeffrey, H., and Forehand, D. (2008), "An Experimental Survey in the Wake of a Simulated Tidal Current Turbine", *Proceedings of IMarEST-Part A-Journal of Marine Engineering and Technology*, 2008, 13-22.

Sun, X., Huang, D., and Wu, G. (2012), "The Current State of Offshore Wind Energy Technology Development", *Energy*, 41, 298-312.

Sutherland, D. R. J., Sellar, B. G., and Bryden, I. G. (2012), "The Use of Doppler Sensor Arrays to Characterise Turbulence at Tidal Energy Sites", *4th International Conference on Ocean Energy, October 17-19, Dublin, Ireland*.

Tao, L., and Cai, S. (2004), "Heave Motion Suppression of a Spar with a Heave Plate", *Ocean Engineering*, 31, 669-692.

Tao, L., and Dray, D. (2008), "Hydrodynamic Performance of Solid and Porous Heave Plates", *Ocean Engineering*, 35, 1006-1014.

Tao, L., Molin, B., Scolan, Y. M., and Thiagarajan, K. (2007), "Spacing Effects on Hydrodynamics of Heave Plates on Offshore Structures", *Journal of Fluids and Structures*, 23, 1119-1136.

Taylor, P. H., Santo, H., and Choo, Y. S. (2013), "Current Blockage: Reduced Morison Forces on Space Frame Structures with High Hydrodynamic Area, and in Regular Waves and Current", *Ocean Engineering*, 57, 11-24.

Tedds, S. C., Owen, I., and Poole, R. J. (2014), "Near-Wake Characteristics of a Model Horizontal Axis Tidal Stream Turbine", *Renewable Energy*, 63, 222-235.

Thomson, J., Polagye, B., Durgesh, V., and Richmond, M. C. (2012), "Measurements of Turbulence at Two Tidal Energy Sites in Puget Sound, WA", *Oceanic Engineering, IEEE Journal of* 37, 363-374.

Togneri, M., and Masters, I. (2011), "Parametrising Turbulent Marine Flows for a Blade Element Momentum Model of Tidal Stream Turbines", *Proc. of the 9th (2011) European Wave and Tidal Energy Conference (EWTEC)*, *5-9 September, Southampton, UK.*

Togneri, M., Masters, I., and Orme, J. (2011), "Incorporating Turbulent Inflow Conditions in a Blade Element Momentum Model of Tidal Stream Turbines", *Proceedings of the International Offshore and Polar Engineering Conference*, 19-24 *June, Hawaii, USA.*

Troen, I., and Petersen, E.L. (1989), "European Wind Atlas". Risø National Laboratory.

Val, D. V., Chernin, L., and Yurchenko, D. V. (2014), "Reliability Analysis of Rotor Blades of Tidal Stream Turbines", *Reliability Engineering & System Safety*, 121, 26-33.

Van der Plas, P. (2014), "The Effect of Platform Motions on Turbine Performance: A Study on the Hydrodynamics of Marine Current Turbines on the Floating Tidal Energy Converter Bluetec". Doctoral dissertation. TU Delft, Delft University of Technology.

Van Riet Bergen, E., Palm, M., Ganzinga, W., Jorritsma, R., and de Ruiter, R. (2013), "Data Processing and Analysis of Bluetec Model Tests at IFREMER (Phase I)". 28 March.

Velázquez, M. T., Del Carmen, M. V., Francis, J. A., Pacheco, L. A. M., and Eslava, G. T. (2014), "Design and Experimentation of a 1 MW Horizontal Axis Wind Turbine", *Journal of Power and Energy Engineering*, 2014. 2, 9-16.

Verley, R., and Moe, G. (1979), "The Effect of Cylinder Vibration on the Drag Force and the Resultant Hydrodynamic Damping", *Bull. River Harbour Lab. Norw. Inst. Technol.*

Vickery, B. J. (1965), "On the Flow Behind a Coarse Grid and Its Use as a Model of Atmospheric Turbulence in Studies Related to Wind Loads on Buildings", Aerodynamic Report No 1143. National Physics Laboratory, Teddlington, England.

Viterna, L. A., and Corrigan, R. D. (1982), "Fixed Pitch Rotor Performance of Large Horizontal Axis Wind Turbines", *Large Horizontal-Axis Wind Turbines*, 1, 69-85.

Vu, K. H., Chenu, B., and Thiagarajan, K. P. (2004), "Hydrodynamic Damping Due to Porous Plates", *Proc. World Scientific and Engineering Academy and Society, 17-19 August, Corfu, Greece.*

Walker, J. M., Flack, K. A., Lust, E. E., Schultz, M. P., and Luznik, L. (2014), "Experimental and Numerical Studies of Blade Roughness and Fouling on Marine Current Turbine Performance", *Renewable Energy*, 66, 257-267.

Walker, S. R., Howell, R., Hodgson, P., and Griffin, A. (2013), "Tidal Energy Machines: A Comparative Life Cycle Assessment Study", *Proceedings of the Institution of Mechanical Engineers, Part M: Journal of Engineering for the Maritime Environment*, 1475090213506184.

Way, S., Thomson, M., and Goldsmith, J. (2013), "Modeling a Floating, Multiple-Rotor Tidal Energy Converter Using Tidal Bladed", *Proceedings of the 1st Marine Energy Technology Symposium METS13. 10-11 April, Washington, USA.*

Weinstein, A., Roddier, D., Banister, A. (2012), "WindWaveFloat Final Report", Technical Report DOE/EE0002651-2. Principle Power Inc.

Whelan, J. I., Graham, J. M. R., and Peiró, J. (2009a), "A Free-Surface and Blockage Correction for Tidal Turbines", *Journal of Fluid Mechanics*, 624, 281-291.

Whelan, J. I., Graham, J. M. R., and Peiró, J. (2009b), "Inertia Effects on Horizontal Axis Tidal-Stream Turbines", *8th European Wave and Tidal Energy Conference*, *7-10 September, Uppsala, Sweden.*

Whelan, J. I., and Stallard, T. (2011), "Arguments for Modifying the Geometry of a Scale Model Rotor", *9th European Wave and Tidal Energy Conference, 5-9, September, Southampton, UK.*

Winter, A. (2011), "Differences in Fundamental Design Drivers for Wind and Tidal Turbines", *OCEANS, 2011 IEEE-Spain*, IEEE, 1-10.

Xia, J., Falconer, R., and Lin, B. (2010), "Numerical Model Assessment of Tidal Stream Energy Resources in the Severn Estuary, UK", *Proceedings of the Institution of Mechanical Engineers, Part A: Journal of Power and Energy*, 224, 969-983.

Xiao, H., Duan, L., Sui, R., and Rosgen, T. (2013), "Experimental Investigations of Turbulent Wake Behind Porous Disks", *Proceedings of the 1st Marine Energy Technology Symposium METS13*, *10-11 April, Washington, USA*.

Appendix A

High Blockage Corrections

The Actuator Disc method is a simple approach that relates the change of pressure imposed on a steady flow by a disc with the net horizontal force exerted on the same object. As shown in Chapter 2, this change in pressure causes the fluid to slow down from the upstream to downstream region. In the context of a constricted flow, the free water surface and bed channel induce extra pressures to the bypass sections of the stream tube. Depending on the sectional area between the channel and rotor, the rotor thrust is greatly increased and the Betz limit may be exceeded.

A common approach to quantify blockage is to restate the flow energy relationships of incompressible fluids across the stream tube sections assuming the mean surface elevation is unaffected. The aim of this correctional method is to find the incident velocity ($u_{0\mathrm{c}}$) for an unbounded flow, which produces the same performance characteristics in the bounded experiments. The unbounded velocity is stated as a function of the measured force, the bypass velocity and the blockage ratio. Then, the equivalent incident velocity is used to correct the experimental TSR, thrust and power coefficients to compare BEM simulations in unbounded flows. The corrected parameters become:

$$C_{\mathrm{T}} = \frac{2T}{A_{\mathrm{D}}\rho {u_{0c}}^2} \qquad C_{\mathrm{P}} = \frac{2Q\omega}{A_{\mathrm{D}}\rho {u_{0\mathrm{c}}}^3} \qquad TSR = \frac{\omega R}{u_{0\mathrm{c}}} \qquad \text{Eq. A. 1}$$

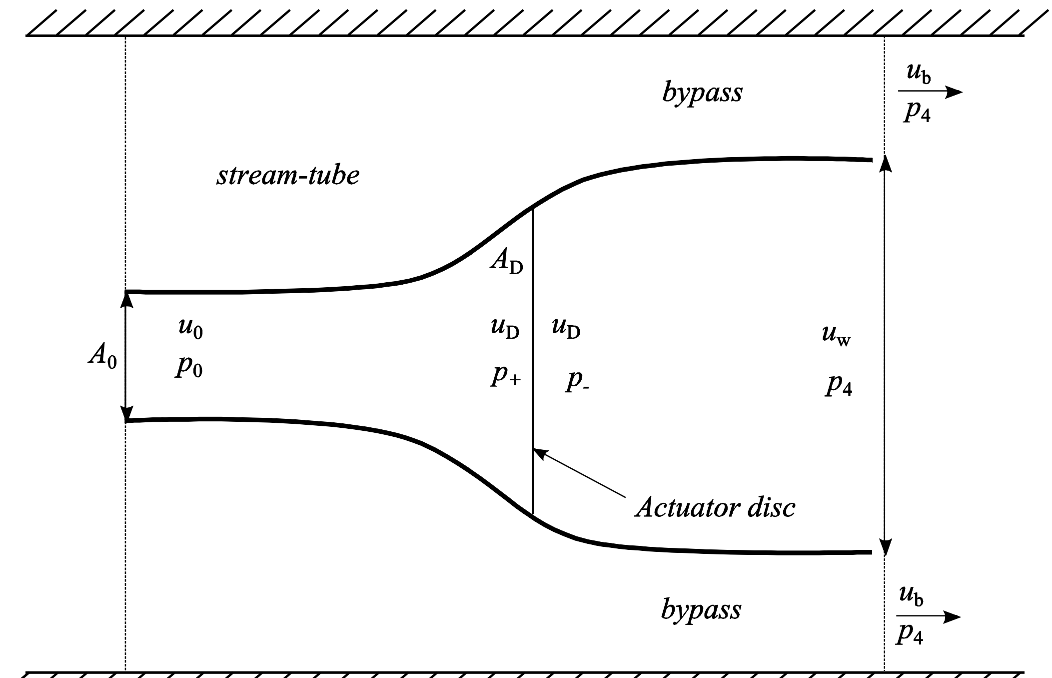

Figure A.1 Diagram of the Actuator Disc in a bounded flow. Linear Momentum is used to calculate the total axial force on the disc. Diagram adapted from Garret and Cummins (2007).

Looking at Figure A.1, the conservation of mass implies at:

stream tube $$A_0 u_0 = A_D u_D = A_w u_w \quad \text{Eq. A.2}$$

and bypass flow $$A_0 u_0 = (A_0 - A_w) u_b + A_w u_w \quad \text{Eq. A.3}$$

From Eq. A.3, the area of the wake before mixing is found as

$$A_w = \frac{A_D u_D}{u_w} \quad \text{Eq. A.4}$$

Substituting Eq. A.3 in Eq. A.4, it follows that:

$$u_w(u_b - u_0) = \varepsilon u_D (u_b - u_w) \quad \text{Eq. A.5}$$

where

$$\varepsilon = \frac{A_D}{A_0} \quad \text{Eq. A.6}$$

represents the blockage ratio given in terms of the wake, bypass and incident velocity.

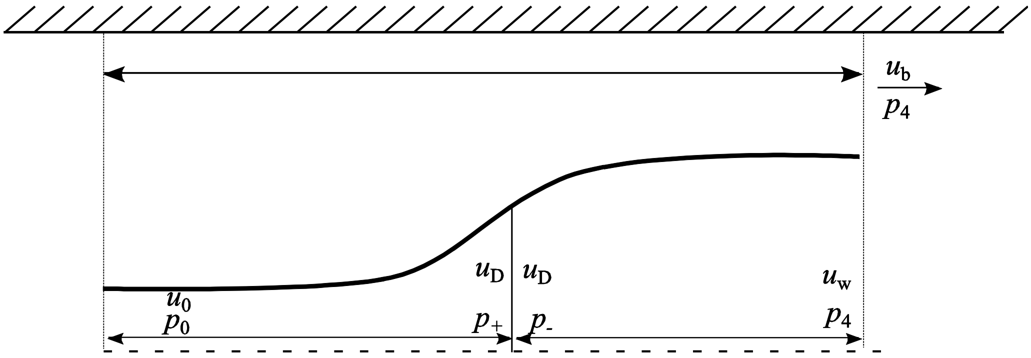

Figure A.2 Half top of the stream tube obtained in a bounded flow, indicating the sections of the energy relationships employed. Diagram adapted from Garret and Cummins (2007).

For an incompressible flow and assuming energy is conserved across the stream tube sections, the change of pressure and velocity across the disc can be estimated with the energy flow relationships or Bernoulli equations within the bypass sections. The horizontal load is then equal to this pressure difference multiplied by the disc area.

The Bernoulli principle applied between far right and left part of the bypass flow (see Figure A.2) gives a relationship of:

$$0.5\rho {u_0}^2 + p_0 = 0.5\rho {u_b}^2 + p_4 \quad \text{Eq. A.7}$$

Rearranging the pressure drop of the disc is:

$$p_0 - p_4 = 0.5\rho({u_b}^2 - {u_0}^2) \quad \text{Eq. A.8}$$

Likewise, in the region just before and after the fluid hits the disc become:

$$0.5\rho {u_0}^2 + p_0 = 0.5\rho {u_D}^2 + p_+ \quad \text{Eq. A.9}$$

$$0.5\rho {u_D}^2 + p_- = 0.5\rho {u_w}^2 + p_4 \quad \text{Eq. A.10}$$

Therefore, the pressure drop between the left and right side on the disc $(p_+ - p_-)$ is found by combining Eq. A.9 with Eq. A.10. After some algebraic work, the force becomes:

$$T = A_{\mathrm{D}} dp = A_{\mathrm{D}}\left(0.5\rho({u_0}^2 - {u_{\mathrm{w}}}^2) + 0.5\rho({u_{\mathrm{b}}}^2 - {u_0}^2)\right) \qquad \text{Eq. A.11}$$
$$= 0.5\rho A_{\mathrm{D}}({u_{\mathrm{b}}}^2 - {u_{\mathrm{w}}}^2)$$

Similarly, the force applied to the fluid is equivalent to the total rate of change of momentum between the incident and the wake-bypass section ($F = dmu$). Expanding the individual forces in the stream tube, the total force is calculated as:

$$F_{\mathrm{T}} = u_0(u_0 A_0) - u_{\mathrm{w}}(u_{\mathrm{w}} A_{\mathrm{w}}) - u_{\mathrm{b}}(u_{\mathrm{b}} A_{\mathrm{b}}) + dp_{+0,\mathrm{xp}} + dp_{+0,\mathrm{b}} \qquad \text{Eq. A.12}$$

Since the wake pressure is recovered to atmospheric value, $dp_{+0,\mathrm{nc}}$ =0. The pressure drop between bypass and incident flow, $dp_{+0,\mathrm{b}}$, is as stated in Eq. A.8. Substituting terms, the equivalent total force is:

$$F_{\mathrm{T}} = u_0(u_0 A_0) - {u_{\mathrm{w}}}^2 A_{\mathrm{w}} - {u_{\mathrm{b}}}^2(A_0 - A_{\mathrm{w}}) + (p_0 - p_4)A_0 \qquad \text{Eq. A.13}$$

Expanding Eq. A.8 into Eq. A.13, the force is:

$$F_{\mathrm{T}} = u_0(u_0 A_0) - {u_{\mathrm{w}}}^2 A_{\mathrm{w}} - {u_{\mathrm{b}}}^2(A_0 - A_{\mathrm{w}}) + 0.5({u_{\mathrm{b}}}^2 - {u_0}^2) \qquad \text{Eq. A.14}$$

After some algebraic manipulation, the total force is finally expressed as:

$$F_{\mathrm{T}} = 0.5A_{\mathrm{w}}(u_{\mathrm{b}} - u_{\mathrm{w}})(u_{\mathrm{b}} + 2u_{\mathrm{w}} - u_0) \qquad \text{Eq. A.15}$$

The velocity at the disc is obtained by equalising the momentum force (Eq. A.11) with the total force on the fluid (Eq. A.15). After arranging terms, the disc velocity is:

$$u_{\mathrm{D}} = \frac{u_{\mathrm{w}}(u_{\mathrm{b}} + u_{\mathrm{w}})}{u_{\mathrm{b}} + 2u_{\mathrm{w}} - u_0} \qquad \text{Eq. A.16}$$

For unbounded flows, the magnitude of the bypass and incident velocity recovers to the same expression, $u_{\mathrm{b}} = u_0$. This force (Eq. A.11) and velocity in the disc (Eq. A.16) correspond equally to the classical Momentum Theory. They are:

$$T = A_{\mathrm{D}} dp = A_{\mathrm{D}} 0.5\rho({u_0}^2 - {u_{\mathrm{w}}}^2) \qquad \text{Eq. A.17}$$

$$u_{\mathrm{D}} = 0.5(u_0 + u_{\mathrm{w}}) = u_0(1 - \mathrm{a}_{\mathrm{axial}}) \qquad \text{Eq. A.18}$$

The power in the disc is equal to the axial force multiplied by the disc velocity. Using Eq. A.11 into Eq. A.16, the power becomes:

$$P_{\mathrm{p}} = Q\omega = Tu_{\mathrm{D}} = 0.5\rho A_{\mathrm{D}} u_{\mathrm{w}} \frac{(u_{\mathrm{b}} + u_{\mathrm{w}})({u_{\mathrm{b}}}^2 - {u_{\mathrm{w}}}^2)}{u_{\mathrm{b}} + 2u_{\mathrm{w}} - u_0} \qquad \text{Eq. A.19}$$

Finally, substituting Eq. A.16 into Eq. A.5. The bypass velocity is given in terms of the blockage ratio, incident and wake velocity as:

$$u_{\mathrm{b}} = \frac{u_0 - u_{\mathrm{w}} + \sqrt{\varepsilon u_0{}^2 - 2\varepsilon u_0 u_{\mathrm{w}} + (1 - \varepsilon + \varepsilon^2) u_{\mathrm{w}}{}^2}}{1 - \varepsilon} \quad \text{Eq. A.20}$$

To obtain the equivalent incident velocity, the definitions of thrust and disc velocity are related and arranged for both bounded and unbounded flow by assuming that the outputs of power, thrust and disc velocities are identical in both flow conditions.

The wake velocity is found by arranging Eq. A.11 using iteration programming with the bypass velocity (Eq. A.20) and force measurements in bounded flow as:

$$u_{\mathrm{w}} = \sqrt{\frac{-T}{0.5\rho A_{\mathrm{D}}} + u_{\mathrm{b}}{}^2} \quad \text{Eq. A.21}$$

Once the convergence of bounded velocities is met, the disc velocity for both the bounded and unbounded flow is from Eq. A.18:

$$u_{\mathrm{D}} = u_{\mathrm{Dc}} = 0.5(u_{0\mathrm{c}} + u_{\mathrm{wc}}) \quad \text{Eq. A.22}$$

Isolating the unbounded wake velocity term:

$$u_{\mathrm{wc}} = 2u_{\mathrm{D}} - u_{0\mathrm{c}} \quad \text{Eq. A.23}$$

Then, equating the thrust in both flows using Eq. A.11 and Eq. A.17, the thrust becomes:

$$T = 0.5\rho A(u_{\mathrm{b}}{}^2 - u_{\mathrm{w}}{}^2) = 0.5\rho A(u_{0\mathrm{c}}{}^2 - u_{\mathrm{w0c}}{}^2) \quad \text{Eq. A.24}$$

Finally, substituting Eq. A.23 into Eq. A.24, the equivalent incident velocity is estimated as:

$$u_{0\mathrm{c}} = u_{\mathrm{D}} + \frac{(u_{\mathrm{b}}{}^2 - u_{\mathrm{w}}{}^2)}{4u_{\mathrm{D}}} \quad \text{Eq. A.25}$$

Subsequently, the measurements are corrected and compared to the BEM model in unbounded flows. Likewise, the water relationship can also be written as (Bahaj, Molland, et al., 2007):

$$\frac{u_0}{u_{0\mathrm{c}}} = \frac{\frac{u_{\mathrm{D}}}{u_0}}{\left(\frac{u_{\mathrm{D}}}{u_0}\right)^2 + \frac{C_{\mathrm{T}}}{4}} \quad \text{Eq. A.26}$$

where the thrust coefficient from Eq. A.11 is:

$$C_{\mathrm{T}} = \frac{2T}{\rho A(u_0{}^2)} = \frac{0.5\rho A(u_{\mathrm{b}}{}^2 - u_{\mathrm{w}}{}^2)}{0.5\rho A(u_0{}^2)} = \frac{(u_{\mathrm{b}}{}^2 - u_{\mathrm{w}}{}^2)}{(u_0{}^2)} \quad \text{Eq. A.27}$$

Appendix B

Statistical analysis for oscillatory flows developed with mean flow opposing regular waves of specified frequencies 0.5-1 Hz and amplitudes of 10, 15 and 20 mm.

Waves opposing flow A_{wave}=10 mm	$f\ (Hz)$						Steady
	0.5	0.6	0.7	0.8	0.9	1	0
H_s (mm)	31.20	6.61	62.56	67.63	7.93	9.79	9.1
H_0 (mm)	29.74	3.34	49.76	51.93	14.903	8.97	8.3
η_{rms}	11.34	15.97	19.51	20.87	6.47	4.25	4.4
F_{Th}	1.25	1.25	1.25	1.25	1.1	1.1	1.1
F_0 (N)	5.48	5.49	5.49	5.47	5.55	5.41	5.47

Waves opposing flow A_{wave}=15 mm	$f\ (Hz)$						Steady
	0.5	0.6	0.7	0.8	0.9	1	0
H_s (mm)	47.25	71.36	92.83	85.51	24.53	10.36	9.1
H_0 (mm)	5.21	65.99	71.69	65.48	19.95	9.45	8.3
η_{rms}	6.48	23.78	28.05	25.62	8.4	4.52	4.4
F_{Th}	1.25	1.25	1.25	1.25	1.1	1.1	1.1
F_0 (N)	5.52	5.52	5.64	5.59	5.50	5.44	5.47

Waves opposing flow A_{wave}=20 mm	$f\ (Hz)$						Steady
	0.5	0.6	0.7	0.8	0.9	1	0
H_s (mm)	64.66	97.55	114.94	95.40	26.76	10.74	9.1
H_0 (mm)	61.01	89.47	92.51	76.27	21.50	9.67	8.3
η_{rms}	21.89	32.06	34.84	28.92	8.99	4.54	4.4
F_{Th}	1.25	1.25	1.25	1.25	1.1	1.1	1.1
F_0 (N)	5.59	5.73	5.60	5.75	5.51	5.52	5.47

Appendix C

The solver ode45 is employed to predict the time-varying force with defined structural and rotor properties and incident velocity inputs. The procedure of solution for the coupled pitch and surge equation of motion begins by setting the differential equations as:

$$\frac{d}{dt}\begin{bmatrix} x_1 \\ \dot{x}_1 \\ x_5 \\ \dot{x}_5 \end{bmatrix} = \frac{d}{dt}[X] = \mathrm{f}_{\mathrm{initial}}$$

Subsequently, the acceleration is isolated from Eq. 6.30 and substituted in the differential format as:

$$\frac{d}{dt}\dot{x}_1 = -\frac{[k_{11} \quad b_{11} \quad 0 \quad b_{15} \quad a_{15} + \mathrm{n}\rho V {C'}_{\mathrm{a}} L]}{m_{11} + a_{11} + \mathrm{n}m_{\mathrm{rotor},11} + \mathrm{n}\rho V {C'}_{\mathrm{a}}}\begin{bmatrix} x_1 \\ \dot{x}_1 \\ x_5 \\ \dot{x}_5 \\ \frac{d}{dt}\dot{x}_5 \end{bmatrix}$$

$$+\frac{\mathrm{n}0.08F_0 + X_1 + \mathrm{n}F_{\mathrm{D},11}(\dot{x}_1, u_0, u_{\mathrm{wave,p}}) + n\rho\dot{u}_{\mathrm{wave,p}}}{m_{11} + a_{11} + \mathrm{n}m_{\mathrm{rotor},11} + \mathrm{n}\rho V {C'}_{\mathrm{a}}}$$

$$+\frac{\mathrm{n}F_{\mathrm{D},11}(\dot{x}_5 L, u_0, u_{\mathrm{wave,p}}) + \mathrm{n}\rho\dot{u}_{\mathrm{wave,p}}}{m_{11} + a_{11} + \mathrm{n}m_{\mathrm{rotor},11} + \mathrm{n}\rho V {C'}_{\mathrm{a}}}$$

In a similar way, the angular acceleration from pitch motion is isolated from Eq. 6.31 and becomes:

$$\frac{d}{dt}\dot{x}_5 = -\frac{\left[0 \quad b_{51} \quad a_{51} + \mathrm{n}L\frac{1}{3}\rho D^3 {C'}_{\mathrm{a}} \quad c_{55} \quad b_{55}\right]}{m_{55} + a_{55} + \mathrm{n}m_{\mathrm{rotor},11}L^2 + \mathrm{n}\rho V {C'}_{\mathrm{a}} L^2}\begin{bmatrix} x_1 \\ \dot{x}_1 \\ \frac{d}{dt}\dot{x}_1 \\ x_5 \\ \dot{x}_5 \end{bmatrix}$$

$$+\frac{\mathrm{n}0.08F_0 L + X_5 + \mathrm{n}F_{\mathrm{D},11}(\dot{x}_1, u_0, u_{\mathrm{wave,p}})L + \mathrm{n}\rho\dot{u}_{\mathrm{wave,p}}L}{m_{55} + a_{55} + \mathrm{n}m_{\mathrm{rotor},11}L^2 + \mathrm{n}\rho V {C'}_{\mathrm{a}} L^2}$$

$$\frac{+\mathrm{n}F_{\mathrm{D},11}(\dot{x}_5 L, u_0, u_{\mathrm{wave,p}})L + \mathrm{n}\rho\dot{u}_{\mathrm{wave,p}}L}{m_{55} + a_{55} + \mathrm{n}m_{\mathrm{rotor},11}L^2 + \mathrm{n}\rho V {C'}_{\mathrm{a}} L^2}$$

Finally, a time solution of amplitude and velocity of oscillation is produced with these sets of ODE using the Runge Kutta method with the initial conditions set to zero. A steady periodic solution is reached within a few seconds and this is used in the analysis.